Effect of Strain on the Optical Properties of GaN Films, and GaN/AlGaN Heterostructure and Laser Lift-Off for GaN/AlGaN Multilayer

By

AMAL MOSTAFA ELGAWADI

MASTER OF SCIENCE IN PHYSICS
Polytechnic University
Brooklyn, New York
2001

MASTER OF SCIENCE IN
ELELCTRICAL ENGINEERING
Polytechnic University
Brooklyn, New York
2001

Submitted to the Faculty of
The Graduate College of the
Oklahoma State University
in partial fulfillment of
the requirements for
the Degree of
Doctor of Philosophy
July 2005

Effect of Strain on the Optical Properties of GaN Films, and GaN/AlGaN Heterostructure and Laser Lift-Off for GaN/AlGaN Multilayer

Dissertation Approved:

Dr. Jerzy Krasinski

Dissertation Adviser

Dr. Paul Westhaus

Dr. Weili Zhang

Dr. Yamin Zhang

Dr. A. Gordon Emslie

Dean of the Graduate College

DEDICATION

To the Spirit of My Father,

To My Dear Mother,

To my wife and my Son,

To My Sister and My Brothers,

To My Family and Instructors

ACKNOWLEDGEMENTS

I express gratitude to my advisor, Dr. Jerzy Krasinski, for his support, and guidance. His expertise and guidance has prepared me well for preparing this dissertation and for my professional future. I would like to thank him for taking the advisory assignment after Dr. Jin-Joo Song. This allowed me to continue my research and projects on III- Nitride group.

I would like to thank my ex-advisor, Dr. Jin-Joo Song, for her terrific and outstanding supervising during my first years in Oklahoma State University. She provided me with the working environment to perform state-of-the-art using top-of-the-line equipment. Her expertise has prepared me well for my professional future. I truthfully appreciate the support she provided to me until the last day in her work at Oklahoma State University.

My sincere appreciations and gratitude to Dr. Paul Westhaus, for his support, advising, and for his comprehensive review for the stylistic issues in this thesis. I would like to thank him for enhancing my knowledge of the vital and indispensable rules in physics that prepared me to have deeper understanding and capability to analyze my research data.

I would also like to thank other members of my advisory committee for the time and effort they have provided me: Dr. Weili Zhang, and Dr. Yamin Zhang.

I would like to express my thanks to all of Dr. Song's students and post-doctors who have helped me in many diverse ways. Dr. Gordon Gainer, and Dr. Brian Little, their unparalleled skills in the lab provided me with a solid foundation for my research in optical characterizations of semiconductors. I would like to acknowledge the vital role Dr. Serge Bidnyk has played in my research. In addition, I would like to express my thanks to Dr. Yong Hwan Kwon, Dr. Sang Kee Shee, Drs. Yong-Hwan Kwon, and Jack Lam.

I would like to express gratitude to Dr. Jerzy Krasinski ex-student, Mr. Erdal Yilmaz for his assistance with the laser lift-off setup.

I would also like to thank Mr. Lee Clark the supervisor of the machine shop in the Oklahoma State University, school of electrical and computer engineering for training me on the basic proficiency and operation of the equipment.

My great appreciation goes to the secretaries in the Physics Department, the school of electrical and computer engineering and the center for laser and photonics research. Especial apperception for Doris Al-Haraki, the ex-financial assistance of the school of electrical and computer engineering.

I express gratitude to the Physics Department at Suez Canal University for the excellent preparation I received during my undergraduate years and for providing the highly knowledgeable Faculty in Egypt from Cairo, Ain Shams, and Asute Universities.

I would like to express my gratitude to physics and electrical departments at Polytechnic University, Brooklyn, New York and the physics department at Al-azhar University for the education and experience they provided me through the three masters I obtained during my graduate studies there.

I would like to express my thanks to Technologies and Devices International, Inc. for providing some of the samples used in the experiments work and N. Kuznetsov at Ioffe Physical-Technical Institute for the electrical characterizations measurements.

Finally, I would like to express my gratitude to all those in my country, Egypt, faculties and employees who supported and facilitated my mission for graduate studies in the United States.

MATERIALS PREPARED FOR PUBLICATION AND PUBLICATION

The materials contained in this thesis were generated from the following refereed article and projects prepared for publications

MATERIALS PREPARED FOR PUBLICATION

1. Influence of compressive strain induced by sapphire substrate on GaN energy gap investigated by laser lift-off.
2. Investigation of strain-induced-effects on the optical properties of GaN/$Al_xGa_{1-x}N$ heterostructure by means of laser lift-off.
3. Investigation of the strain and piezoelectric effects on the optical properties of $Al_{0.2}Ga_{0.8}N$/GaN heterostructure

PUBLICATION

"Comparative Study of HVPE- and MOCVD-Grown Nitride Structures for UV Lasing Applications", J. B. Lam, G. H. Gainer, S. Bidnyk, Amal Elgawadi, G. H. Park, J. Krasinski, J. J. Song, D. V. Tsvetkov2, and V. A. Dmitriev, Mat. Res. Soc. Symp. 639, G6.4.1, (2001).

TA BLE OF CONTENTS

Chapter Page

PART I: BACKGROUND

LIST OF TABLES

Table Page

LIST OF FIGURES

Figure Page

PART I

BACKGROUND

CHAPTER I

INTRODUCTION

Although the elemental semiconductors, and in particular Si, have been useful for the development of microelectronics, they have some important drawbacks [1]. The fundamental band gap of these semiconductors is indirect. This implies that they emit light very poorly and their absorption coefficients are low. As a solar energy converter, Si is technologically good, but because of its small energy gap the conversion efficient is low, so it cannot perform many important functions. For optoelectronic applications, in particular, it was then necessary to turn to other materials. It turned out that compound semiconductor material offered many of the desired properties and could be synthesized without much difficulty, namely III-V, II-VI, IV-VI, and IV-IV compounds. Historically, for optoelectronic device applications, the III-V compounds have been the first and most widely used.

Indium antimonide (InSb) was the first III-V compound semiconductor to be discovered in 1950. The particular features of this compound that attracted interest were the ease with which it could be synthesized, the electron mobility, and the ionic component in the crystal binding. These properties are still of immense interest, and as advanced epitaxial techniques are being developed, the purity of the crystals continues to

improve. Furthermore, because of its low bandgap, E_g= 0.17 eV (~7298 nm), InSb has become important for the development of far infrared detector technology. The invention of the semiconductor laser turned the interest to other III-V compounds such as GaAs, E_g= 1.43 eV (~867 nm), and InP, E_g=1.35 eV (~918 nm).

The next in order is GaP, which has its bandgap, E_g=2.1 eV (~590 nm) in the visible part of the spectrum and therefore became important for the development of the light-emitting diode (LED). Though the bandgap of GaP in indirect, by certain doping technique, it is possible to improve the radiative efficiency.

An attractive feature of the binary compounds is that they can be combined or alloyed to form ternary or quaternary compounds, or mixed crystals. These compounds are made up of three or four group III and V atoms and are indicated by the tie lines between the binary compounds in Figure 1.

By choosing different binary compounds, it is possible to select different band gaps, and therefore varying emission energies for light sources. However, by alloying, it is possible to vary the bandgap continuously and monotonically, and therefore the band structure, electronics and optical properties. The formation of ternary and quaternary compounds of varying band gaps also enables the formation of heterojunctions, which have become essential for the design of high-performance electric and optoelectronics devices. Among the common GaAs and InP-based ternary and quaternary compounds, the properties of $Al_xGa_{1-x}As$ $(0 \leq x \leq 1)$ have been most thoroughly investigated. The

bandgap of $Al_xGa_{1-x}As$ depends on the mole fraction of x of AlAs in the solid solution and changes continuously from 1.43 eV (GaAs, x=0) to 2.1eV (AlAs, x=1). Other important ternary and quaternary compounds are $GaAs_{1-x}P_x$, $In_{1-x}Ga_xP$, $In_xGa_yAl_{1-x-y}As$ and $In_{1-x}Ga_xAs_yP_{1-y}$. These quaternary have emerged as being extremely important for optical communications; since their band gaps correspond to the spectral window in which silica fiber have their lowest loss and dispersion.

However, there are many areas where conventional III–V semiconductors cannot be used. Wide bandgap (short wavelength) light emitters are required for full color display, laser printers, high-density information storage, and under water communication. High temperature and high power transistors are needed for automobile engines, future advanced power distribution systems, and electric vehicles. Si and conventional III–V semiconductors are not suitable for designing and fabricating optoelectronic devices in the violet and blue region of the spectrum. There band gaps are not sufficiently large. GaAs based electronic devices cannot be used at high temperatures.

Group III–nitrides are particularly suitable for applications in these areas. The band gaps of the III–nitrides are large and direct. The band gap values are 1.9 eV for InN, 3.4 eV for GaN, and 6.2 eV for AlN as seen in Figure 1. Because of their wide band gaps and strong bond strength, they can be used for violet, blue, and green light emitting devices and for high temperature transistors. InN and AlN can be alloyed with GaN. This allows tuning of the band gaps and emission wavelengths. ZnSe based semiconductors also have band gaps suitable for short-wavelength optoelectronic devices but the bond strength in

the II–VI wide band gap semiconductors is low. Landwehr et. al.[2] have compared the bond energy of several different semiconductors. The values of the bond energy are 2.3 eV/ bond in GaN and 1.2 eV/bond in ZnSe.

However, in the seventies and eighties, the development of ZnSe based LEDs and LDs put that compound much ahead of GaN. In the seventies, the development of nitride physics and GaN devices was almost stopped because of two main barriers:

(1) The suitable substrates that would allow the growth of low dislocation-density-quantum heterostructure devices were lacking.; and

(2) The p-type doping method was unknown

These barriers were overcome in the early nineties, when Amano et. al.[3] and Nakamura et. al.[4] developed the low temperature buffer layer that lowered the dislocation density in nitride epitaxial layers from 10^{12} to 10^{8} cm^{-2} and discovered the p-type GaN doping by Mg.

The low-temperature buffers could be GaN, AlN or AlGaN layers. AlN buffer layers[5] and later low-temperature GaN buffer layers[6] of thickness ranging between 50-100 nm, were recognized as a way to relieve the stress and associated defects in GaN thin films grown on large lattice-mismatched substrates. The buffer layer acted as a template to supply nucleation sites for growth of the GaN epilayer.

The buffer relieves some of the large lattice mismatch that is harmful to achieving high-quality films. The layer also effectively absorbs the stress created by the lattice and thermal expansion coefficient mismatch through the generation of extended defects such as dislocations and stacking faults. The approaches have resulted in reducing the density of dislocation-induced defects in the GaN film from 10^{12} cm^{-2} to 10^{8} cm^{-2}, which is adequate for GaN-based optoelectronic device operation.

The density of threading dislocations has been reduced even further using an epitaxial-lateral-overgrowth (ELOG) process [7, 8]. The technique was successful in reducing the threading dislocation density down to the order of 10^{7} cm^{-2} by implementing SiO_2 mask windows to selectively limit the propagation of the threading dislocations. However, dislocation density of 10^{4} cm^{-2}, is essential for laser diodes (LDs) that are particularly important for high power LDs[31] and to create long lasting semiconductor laser.

The growth of GaN epitaxial layers and quantum structures by both MOVPE[9] and MBE[9] made it possible to determine many basic physical properties of GaN[10]. These achievements and the fact that, in contrast to short-lived ZnSe based devices, the nitride-based structures remain stable during long laser operation, resolved the ZnSe versus GaN competition. Successful commercialization of blue diodes by Nichia Ltd. and construction of the first blue laser diode by Nakamura[11] in 1996 made GaN based technology the unique solution for blue and UV semiconductor laser diodes of the future.

Monte Carlo simulations predict high mobility of electrons[12,13]. A group at Bell Laboratories, Lucent Technologies[14], reported a mobility of 75000 cm^2/Vs at temperature T=4.2 K for $Al_{0.5}Ga_{0.95}N/GaN$ grown by molecular beam epitaxy (MBE) on undoped low dislocation (~$2x10^8$ cm^{-2}) GaN template which was prepared previously by hydride vapor phase epitaxy (HVPE). The Monte Carlo simulated peak velocity in GaN is close to 3×10^7 cm/s and the saturation velocity is 1.5×10^7 cm/s.[13] Both values are considerably higher than the values for Si and GaAs. The nitrides have good thermal conductivity[15]. As discussed by Dietrich[16] and Khan[17], group III–nitride devices can work not only at much higher temperatures but also in hostile environments.

Gallium nitride (GaN) as a solid-state blue light emitter is the ideal material for blue laser diodes. The first major commercial blue laser diodes are high-density optical storage, such as DVDs; other potential applications include high-resolution laser printers and full-color video displays. Blue lasers can potentially make biomedical laser surgery safer and "invisible," and could ultimately lead to solid-state lighting that could make incandescent and fluorescent light bulb obsolete.

For high-performance electronics, GaN offers the potential to handle much higher powers and frequencies than conventional materials, potentially doubling the effective range for radar and satellites while increasing bandwidth. GaN-based devices should ultimately lead to increased system efficiency, reduced system costs, and new market applications.

Different substrate materials have been examined for GaN growth. Substrates such as sapphire[18], GaAs[19], Si[20,21], MgO[22], SiC[23], and ZnO[24] have all been tried with varying degrees of success.

The most commonly used growth substrate is sapphire, because of the following:

1. its compatibility with GaN crystal orientation,
2. its ability to withstand the high-temperature growth conditions,
3. its availability of large-area crystal of good quality,
4. its transparent nature,
5. its fairly mature growth technology, and
6. its relatively low price.

However due to the lattice and thermal-expansion coefficient mismatch between the sapphire and GaN[25] , as seen in Table 2, a high density of extended defects, such as dislocations and stacks faults, at the GaN thin film/substrate take place[24,26].

Dislocations can cause deterioration in the operation of quantum-well based optoelectronic devices, and high power semiconductor lasers mainly by the following mechanisms:

1. Serving as nonradiative recombination centers for electrons and holes leading to heat generation instead of optical emission.
2. Disturbing the epitaxial growth, thereby making perfect flat structures difficult to be obtained.

However, GaN based devices are much more tolerant of the presence of dislocations than classical devices based on GaAs. In GaN devices, efficient photo- and electro-luminescence was observed even in materials having dislocation densities as high as 10^8 - 10^9 cm^{-2}.

Several articles indicated that edge dislocation in GaN is negatively charged for example, Hansen et. al.[27] using scanning capacitance microscopy, Cherns et. al.[28] using electron holography, and Oila et. al.[29] using positron spectroscopy. Weimann et. al.[30] attributed the charged dislocation lines to the existence of traps along the dislocation lines. Empty traps are electrically neutrals, while filled trap are negatively charged. The negatively charged lines act as scattering centers.

Porowski et. al.[31] concluded that nonradiative recombination due to the presence of dislocations is destructive and detrimental to the efficiency of devices based on GaN/AlGaN quantum wells and heterostructure, such as UV light emitted diode and UV laser diode. They reported that the high-density dislocations in high power laser diodes (LDs) should be avoided. Dislocation density below 10^4 cm^{-2} is mandatory for manufacturing such devices. Bulk GaN substrates offer great potential for high-performance devices but they are manufactured at high prices prohibitive to volume production[32].

The development of the high nitrogen pressure solution growth (HNPSG) method[33] was the important step, which allowed growth of the first dislocation-free. Porowski et.

al.[31] have reported that high quality high-pressure grown GaN single crystals have a dislocation density not higher than 10^2 cm^{-2} is grew by high nitrogen pressure solution growth (HNPSG) method while the best quality GaN layers on sapphire have dislocation density above 10^7 cm^{-2} [Ref. 34]. This creates possibilities to growth epitaxial structures for high power laser diode devices [Porowski et. al.[31]]. However, typical duration of the growth processes is 120 - 200 hours, which gives a crystal with a small linear size up to 20 mm.

Today, GaN substrates are produced by vapor-phase transport or epitaxial-type growth. Wafer sizes are small and prices are high, and it is likely that volume products such as LEDs will continue to be fabricated on sapphire for the near future. Alternative hybrid options with higher dislocation densities are also available. For example, GaN-on-sapphire templates using HVPE, which reduces production times and equipment downtime. The main concern for the technology based on freestanding HVPE grown GaN substrates is the reduction of the density of dislocations. The size of the substrates is already sufficient for many industrial applications; however, the dislocation densities remain two orders of magnitude above the magic value 10^4 cm^{-2}, necessary for high power laser diodes (LDs). The prospects for this method depend on whether the technology will be able to break this barrier in the near future.

Until bulk GaN substrate prices fall substantially, sapphire will remain the first choice for volume production. In fact, for GaN-based LEDs, which are today successfully produced on foreign substrates, manufacturers may never transfer to bulk GaN substrate.

However, for laser diodes, GaN substrates are a much more attractive proposition, and here a market for GaN substrates may develop. Using HVPE deposition of 2-5 μm of Si-doped GaN on sapphire substrates with a deposition rate 100 times faster than that of MOCVD growth is obtained[35]. It believes that the material quality associated with the HVPE process, which has a yield of over 90%, is actually higher than that of MOCVD. Dislocation densities are 10^8 cm^{-2}, and are expected to decrease as the growth process is improved.

In summary shorter wavelength (UV range) requires further progress in strain engineering to prevent the generation of misfit dislocations, nonradiative recombination and the cracking of AlGaN layers with higher aluminum content.

New possibilities were opened in the late nineties by the lift-off technology[36,37,38] to reduce the dislocation density below 10^7 cm^{-2}. The GaN layer is separated from the sapphire substrate and then is used as a freestanding GaN substrate. Though this technology is sophisticated and expensive, it gives GaN substrates with dislocation density of about 10^6 cm^{-2} and reduces thermal stresses in devices. Such two-inch substrates are already available and they serve for construction of blue lasers of a power of hundreds of mW.

Kelly et. al.[36] reported that that the transparency of sapphire and the thermal decomposition of GaN could be combined to separate GaN thin films from sapphire substrates. Kelly et. al.[39] reported the first successful lift-off of thin (5 μm) GaN films from sapphire using pulsed laser-assisted third harmonic of a Q-switched Nd:YAG laser.

The photon energy of the pulsed laser 3.49 eV (355 nm) is just above the absorption edge of GaN and absorption yields metallic Ga and N_2 gas as decomposition products.

Wong et. al.[38] have also reported pulsed UV laser processing of GaN thin films using a KrF Excimer laser at photon energy 5 eV (~248 nm), well above the absorption edge of GaN. They utilized the transparency of the sapphire substrate and AlN capping layers to allow processing at higher fluencies without visible decomposition. Wong et. al.[38] estimated the interfacial decomposed layer to be in the range of the absorption length depth for 248 nm incident beam that is less than 75 nm.

The GaN lift-off technique take advantage of the thermal properties of GaN which allowed the decomposition[40] of GaN to metallic Ga and N_2 (gas) as a different sublimation process. The bonding energies of the III-V nitrides are relatively high compared to other III-V compounds. The bonding energy for AlN, GaN and InN are 11.52, 8.92, and 7.72 eV/molecule, respectively[41]. These high bond energies result in the higher melting temperatures and good thermal stability of the AlN and GaN compounds compared to other compound semiconductors. Table 5 shows the melting point for AlN, GaN, and InN. Groh et. al.[42] observed the presence of Ga droplets during decomposition in vacuum suggesting the GaN undergoes a dissimilar sublimation process. Later reports suggest the GaN decomposition process is strongly affected by the choice of substrate material and ambient conditions. In a report by Sun et. al.[43] the thermal decomposition of MOCVD grown GaN on R-plane sapphire was found to occur at a temperature of 1000°C in hydrogen ambient. They reported that the surface of the GaN thin film was totally decomposed leaving only a residual Ga droplet surface on the sapphire.

Figure 40 shows the calculated P-T curve for GaN. The plot indicates decomposition of the GaN to Ga and N_2 will occur at a critical temperature of ~1000°C at atmospheric pressure. The rectangular region to the lift shows the predicted decomposition area of GaN at the critical temperature, which correlates to the experimental data obtained by various groups[42,43,44].

Despite the big commercial success of blue and green LEDs based on GaN, AlGaN and InGaN compounds and an introduction blue and violet LDs to the market, the physical properties of GaN and InGaN and AlGaN systems are still not well understood. Correspondingly, the technology of GaN devices is still far from maturity.

The challenge facing GaN researchers is the production of efficient LEDs and LDs in the range of wavelength $\leq$ 260 nm. The wide band gap of AlN (6.2 eV) make its alloy with GaN the only option for such wide band gap semiconductor devices. However, as the band gap increases, nonradiative mechanisms increases, energy dissipate as heat leading to lower power and contributing to heat-management problems. The Nonradiative mechanisms also increase the fraction of light emitted at long wavelengths, which can interfere with fluorescence-based sensors.

In this study, we utilized the lift-off technique to study the effect of strain and dislocation induced by the lattice and thermal expansion coefficients mismatch between GaN and sapphire on the optical properties of GaN epilayers and AlGaN/GaN heterostructure. We performed lift-off for 4-AlGaN/GaN heterostructure for the first time to the best of our knowledge. We found that defects created by the strain and dislocation lines acted as trapping centers that increased the nonradiative recombination

and undermined the efficiency of the GaN based devices.

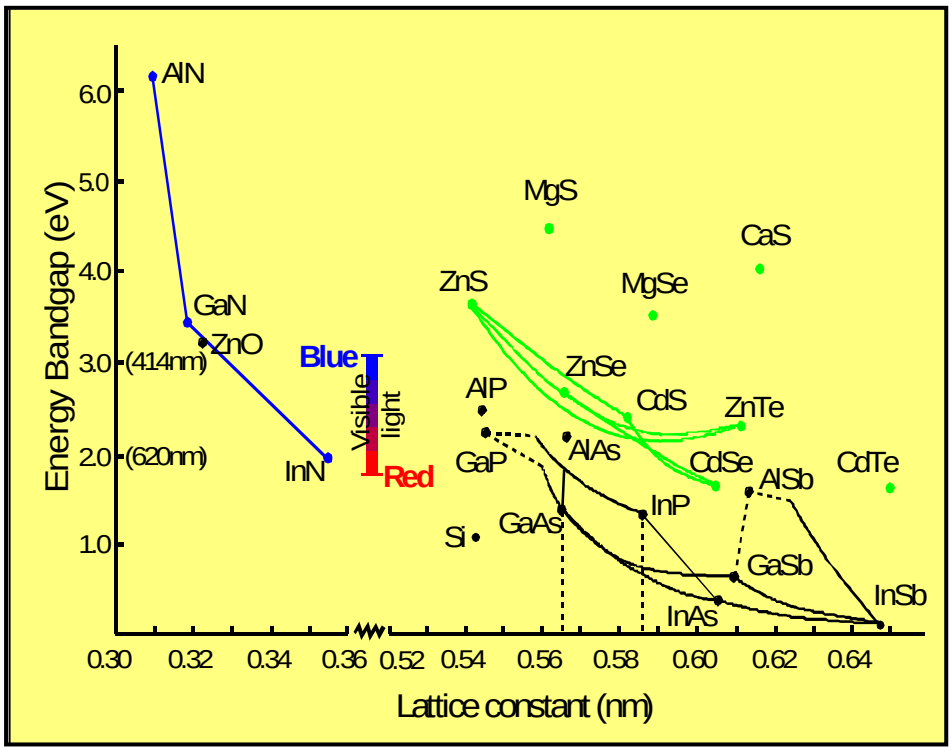

Figure 1: Energy bandgap versus lattice constant for common elemental and compound semiconductors. The tie lines joining the binaries represent ternary compositions. The dashed lines represent indirect bandgap materials. The band gap values of III-nitride are 1.9 eV for InN, 3.4 eV for GaN, and 6.2 eV for AlN. [Adopted from ref. 45].

CHAPTER II

OPTICAL PROCECSSES IN SEMICONDUCTORS

II.A. ELECTRON-HOLE GENERATION AND RECOMBINATION

The operation of almost all optoelectronic devices is based on the creation or annihilation of electron-hole pairs. Pair formation essentially involves raising an electron in energy from the valence band to the conduction band, thereby leaving a hole behind in the valance band. In principal, any energetic particle incident on a semiconductor, which can impart energy at least equal to the band gap energy to an electron in a valance band, will create pairs.

The simplest way to create electron-hole pairs is to irradiate the semiconductor. Photons with sufficient energy are absorbed, and these impart their energy to the valance band electrons and raise them to the conduction band. This process is, therefore called absorption. The reverse process, electron and hole recombination is associated with the pair giving up its excess energy. Recombination may be radiative or nonradiative. In a nonradiative transition, the excess energy due to recombination usually imparted to phonons, and dissipated as heat.

In a radiative transition, the excess energy is dissipated as photons, usually having energy equal the band gap (i.e. $\hbar\omega = E_g$). This is the luminescent process, which is

classified according the method by which the electron-hole pairs are created. Photoluminescence involves the radiative recombination of electron-hole pairs created by injection of photons. Cathodoluminescent is the process of radiative recombination of electron-hole pairs created by electron bombardment. Electroluminescence is the process of radiative recombination following injection with a p-n junction or similar device.

Under steady-state condition, the generation rate G for creating electron-hole pairs must equal the recombination rate R:

$$G = R$$

Generation and recombination process involve transition of carriers across the energy bandgap and are therefore different for direct and indirect bandgap semiconductors, as illustrated in the energy-momentum diagrams of direct and indirect bandgap semiconductor, Figure 2. In order to characterize the optical properties of a semiconductor materials one should considers the following basic mechanisms[46]:

1. Photon absorption (electron-hole formation, stimulated generation, or electron-hole pair generation) - outlines photon absorption, which stimulates the generation of an electron in the conduction band while leaving a hole in the valence band.
2. Radiative recombination:

    A. Spontaneous recombination or photon emission- represents the case of an electron in the conduction band recombining spontaneously with a hole (missing electron) in the valence band to generate a photon. If a large number of such events should occur, relatively incoherent emission would result, since the emission time, direction would be random, and the

photons would not tend to contribute to a coherent radiation field. This is the primary mechanism within a light emitting diode (LED), in which photon feedback is not provided.

B. Stimulated emission (stimulated recombination or coherent photon emission) - is the reverse of absorption. Here an incident photon perturbs the system, stimulating the recombination of an electron and a hole and simultaneously generating a new photon i.e. the stimulated emission adds a photon at the same frequency, at the same phase, in the same polarization state, and propagate in the same direction as the stimulating wave. This all-important positive gain mechanism is necessary for lasers to operate.

C. Nonradiative recombination: Non-radiative recombination - represents the several non-radiative ways in which a conduction band electron can recombine with a valence band hole without generating any useful photons. Instead, the energy is dissipated as heat in the semiconductor crystal lattice. These effects are to be avoided if possible. In practice, there are two general non-radiative mechanisms for carriers: (1) Non-radiative recombination centers, such as point defects, surfaces and interfaces in the active region of the laser. (2) Auger recombination, in which the electron-hole recombination energy is given to another electron or hole in the form of kinetic energy.

II.B. EXCITON ABSORPTION IN DIRECT BAND GAP SEMICONDUCTORS

II.B.1. Free Excitons:

When a photon with energy $(\hbar\omega)$ above the fundamental band gap E_g is incident on a crystal, the photon energy absorb in the crystal. An electron from the valence band can be promoted to the conduction band, a process create a free electron and a free hole. The threshold of this process is

$$\hbar\omega > E_g \qquad (1)$$

However, this is not the lowest excited state of a crystal. The lowest excited state of the crystal occurs when an electron and a hole are bound to each other by their attractive Coulomb interaction

$$E(r) = -e^2 / 4\pi\varepsilon r \qquad (2)$$

where r is the distance between the particles and ε the appropriate dielectric constants, and e is the electron charge. This interaction, however, leads to considerable changes in the optical properties of the material, particularly around the absorption edge as seen in Figure 6. The bound electron-hole pair is called an "exciton" or a "free exciton" and usually dentate as (FE). In excitons, the electron is bound to the hole and the quasi-particle is electrically neutral. However, an exciton is free to move as a "unit" throughout the crystal, similar to a real atom in free space. All excitons are unstable with respect to the ultimate recombination process or the exciton inhalation in which the electron drops into the hole. The operation of almost all optoelectronic devices is based on the creation

or annihilation of electron-hole pairs. There are two models for the free excitons (FE), the so-called Wannier excitons and Frenckel exciton as illustrated in Figure 3:

- Wannier free excitons (Weakly bound exciton):

In Wannier exciton, the Bohr radius (i.e. the mean distance between the electron and the hole) is large in comparison to the length of the lattice unit cell as illustrated in Figure 3 (a). This condition is met in most II-VI, III-V and column IV semiconductors. The mathematical treatment of Wannier exciton problem (electron-hole pair) is equivalent to the hydrogen problem (electron-proton pair). Refer to quantum mechanics textbooks (see Ref., [47,48]).

The excitonic energy eigenvalues are obtained as

$$\varepsilon_r \equiv \varepsilon_{nlm} = -\frac{m_r e^4}{2\hbar^2 \varepsilon^2}\left[\frac{1}{n^2}\right] = -E_B\left[\frac{1}{n^2}\right] \qquad (3)$$

where the integers n = 1, 2, …….; ℓ = 0, 1 … (n-1); and m= -ℓ, …..ℓ are the main, orbital and magnetic quantum numbers respectively. In analogy with atomic spectroscopic notations it is customary to refer to s-like excitons when ℓ= 0 and to p-like excitons when ℓ=1, etc. E_B is the exciton Rydberg energy or simply the exciton energy, which is often

$$E_B = \frac{m_r e^4}{2\hbar^2 \varepsilon^2} = \frac{e^2}{2a_B \varepsilon} = \frac{\hbar^2}{2m_r a_B^2} \qquad (4)$$

where $$a_B = \frac{\varepsilon \hbar^2}{m_r e^2} \qquad (5)$$

is the exciton Bohr radius. ε_r specifies the binding energy of the electron-hole pair (exciton).The total exciton energy is

$$\varepsilon_n = E_g + \varepsilon_r + \varepsilon_R = E_g - E_B \left[\frac{1}{n^2}\right] + \frac{\hbar^2 K_c^2}{2M} \qquad (6)$$

where E_g is the band gap, $\varepsilon_R = \frac{\hbar^2 K_c^2}{2M}$ describe the center-of-mass motion, K_c is the center to-mass wave number and $M = m_e + m_h$ is the total mass of the electron-hole pair.

At $K_c = 0$ the total exciton energy is

$$\varepsilon_n = E_g - E_B\left[\frac{1}{n^2}\right] \qquad (7)$$

Equation (7) shows clearly that the exciton level energies or the exciton resonances occur within the forbidden gap as seen in Figure 4.

The exciton dispersion relationship (that is the exciton energy versus the wave vector), Figure 4, shows the transition leading to the formation of free excitons below the energy gap i.e. to the energetic positions of the lowest three excitonic stated at $K_c = 0$. Figure 5 shows a low temperature absorption spectrum of high quality GaAs near the band edge. Figure 6 shows the intense absorption lines below the bandgap energy are n=1, 2 and 3 free exciton transition.

- Frenkel free excitons (Tightly bound exciton):

Frenkel exciton is realized when the exciton Bohr radius is on the order of, or smaller than, an atomic unit cell. It is a bound exciton as seen in Figure 3 (b). The exciton

is localized on or near a single atom: the hole is usually on the same atom as the electron although the pair may be anywhere in the crystal. Frenkel exciton exists in wide–gap semiconductor/insulators and in some organic materials[48].

For GaN, excitons are well described by the Wannier formalism and for the rest of this thesis the term exciton will refer to a Wannier-Mott exciton.

II.B.2. Bound Excitons Absorption:

A real crystal is never perfect. Intentionally or unintentionally, both donors and acceptors are simultaneously present in a semiconductor, and any semiconductor is usually compensated to some degree. Imperfections can attract free excitons that become localized at the defect size, becoming bound excitons (BX). The binding energy of the exciton to the defect is often quit small, typically few meV. Therefore, bound excitons are best observed at very low temperature. Exciton may be bound to a donor (DX) or to an acceptor (AX). Bound excitons play important rule particularly in luminescence, as we will discuss in more detail later.

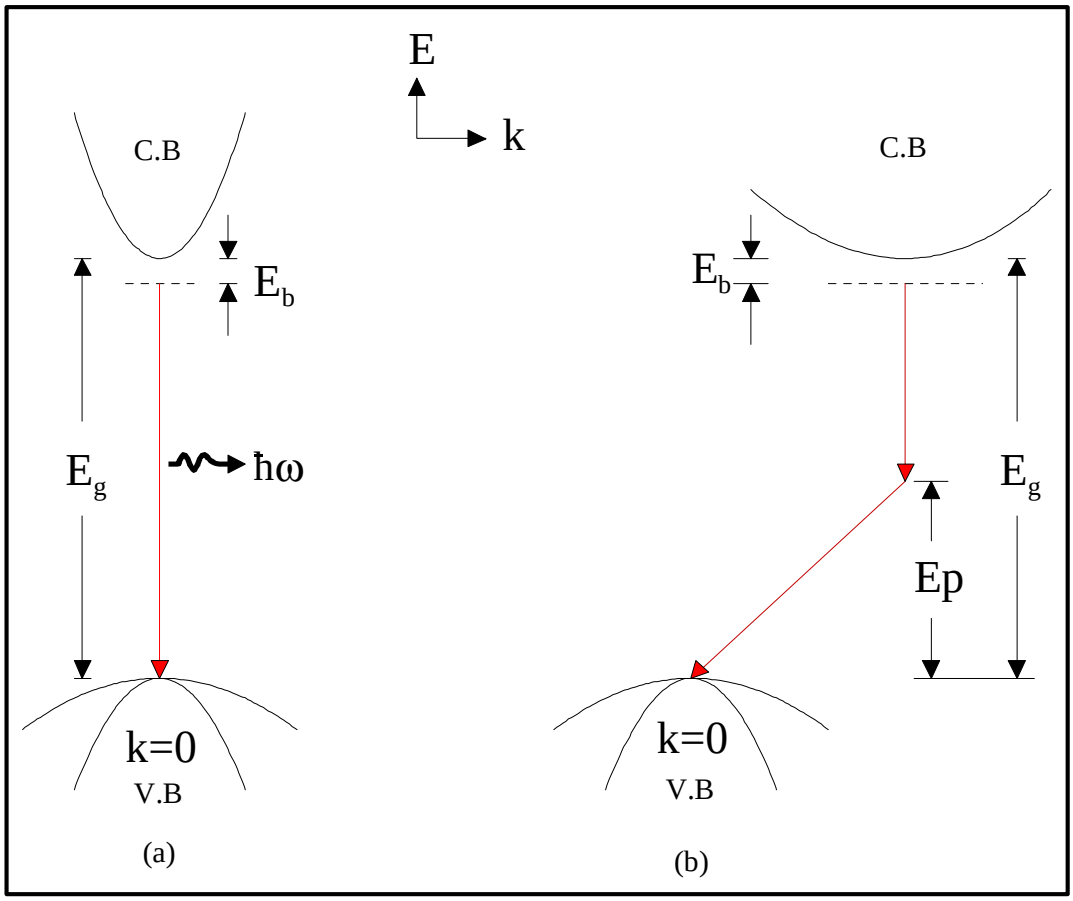

Figure 2. Exciton recombination in direct and indirect bandgap semiconductors

(a) Exciton recombination in direct bandgap semiconductors. The valence band maximum and the conduction band minimum at the Brillion zone center (k=0). Therefore, no change in momentum and radiation recombination is possible.

(b) In indirect band gap, the valence band maximum and the conduction band minimum not at (k=0). Phonon needs to be involved, in the transition for momentum conservation. Therefore, the probability of radiative recombination is very low in indirect band gap semiconductors.

[Adopted from ref. 1]

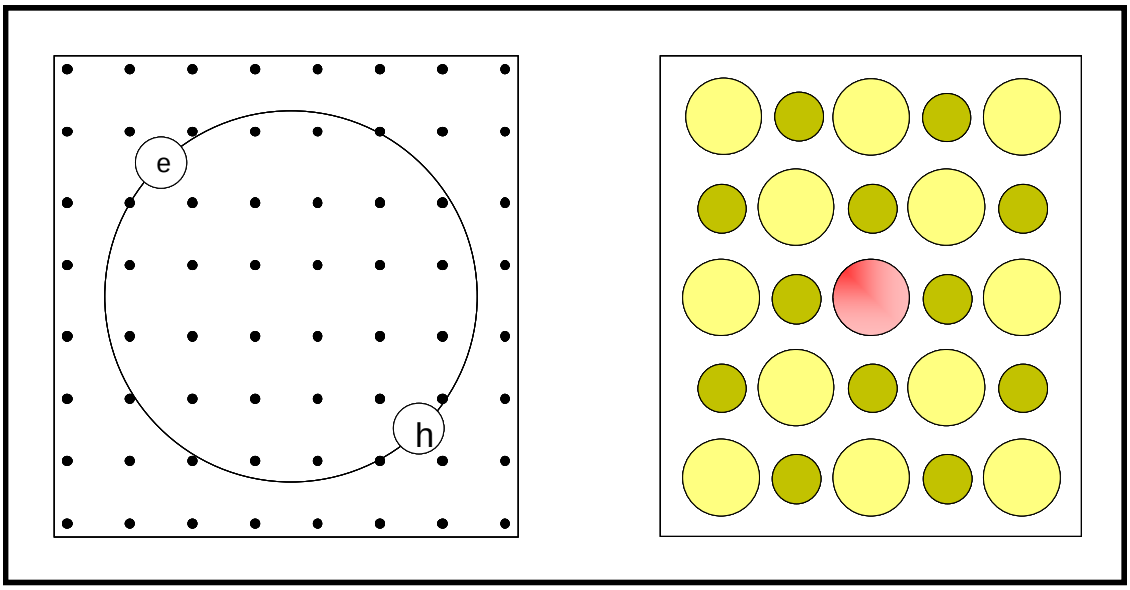

Figure 3: Illustration of Wannier and Frenckel free excitons

a) An exciton is a bound electron-hole pair, usually free to move together through the crystal. The exciton shown is a Mott-Wannier exciton; it is weakly bound, with an average electron-hole distance large in comparison with a lattice constant. [Adopted from Ref. 49.]

b) A tightly bound or Frenkel exciton shown localized on one atom in an alkali halide crystal. An ideal Frenkel exciton will travel as a wave throughout the crystal, but the electron is always close to the hole.

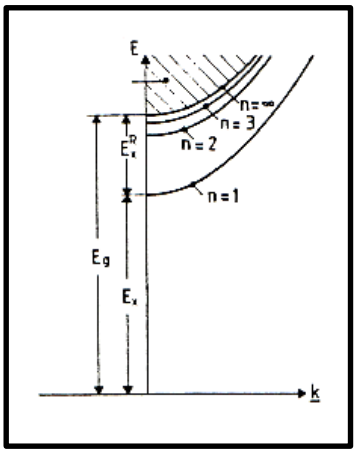

Figure 4. Energy levels of excitons. The exciton dispersion curves of Mott-Wannier excitons in direct gap semiconductors of the entire crystal. The crystal ground state (zero energy, zero momentum) is the point at the origin, K=o. The bound states form the discrete bands with main quantum numbers n=1, 2,…., ∞, within the forbidden gap. E_g , E_x and E_x^R represent the band gap energy, the exciton energy, and exciton Rydberg energy, respectively. [Adopted from Ref. 48].

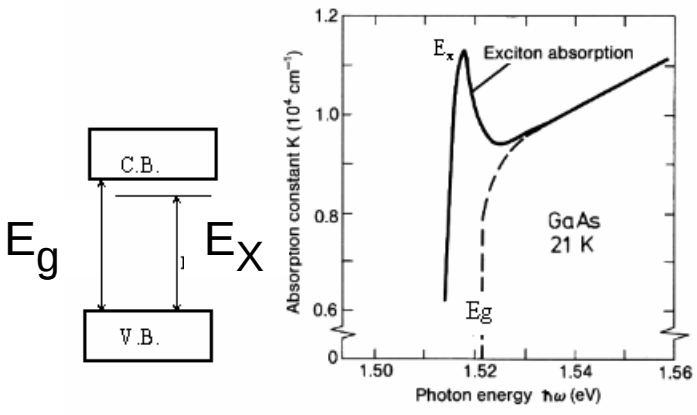

Figure 5. Absorption coefficient of GaAs measured at 21 K near the band gap edge. The dashed curve would be the results in the absence of exciton after M.D. the binding energy of the exciton is the difference between the band gap energy (E_g) and the exciton energy (E_x), after Struge [Ref. 50,51]

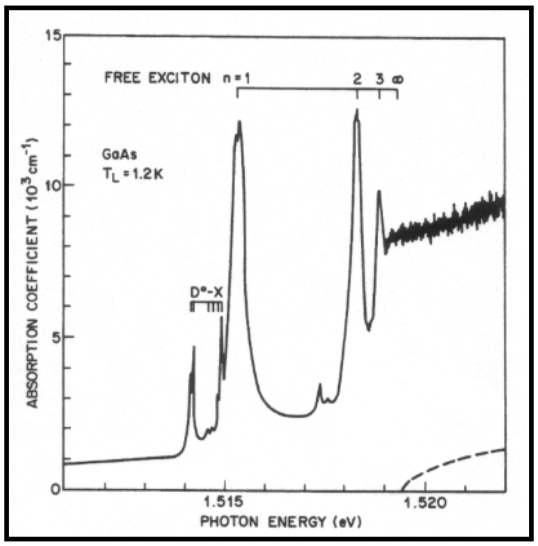

Figure 6. Absorption spectrum of high quality GaAs near the band edge at 1.2 K. The free excitons n=1, 2 and 3 transitions are clearly seen. Excitons bound to donors (D° - X) are also indicated. The dashed line indicates the spectrum in case of the absent of excitons i.e. free-carrier (band-to-band) absorption. [Adopted from ref. 52]

CHAPTER III

GENERAL PROPERTIES OF GROUP III-NITRIDE

III.A. STRUCTUREL PROPERTIES OF THE GROUP III-NITRIDES

All optical processes in semiconductors are related to their band structure. GaN crystallizes in cubic (zincblende), hexagonal (wurtzite), or rock salt structure. Generally, GaN grows with a wurtzite (Hexagonal) structure and will be the subject of our discussion and the whole thesis. The *s* levels of Ga constitute the conduction, which called Γ_7 - conduction band, while the three *p* levels of nitrogen form the valence band as seen in Figure 7.

For GaN, excitons are well described by the Wannier formalism and for the rest of this thesis the term exciton will refer to a Wannier-Mott exciton as it was mentioned before. Excitons associated with the Γ_9^V valence band (A-band), the upper Γ_7^V valence band (B-band), and the lower Γ_7^V valence band (C-band) are often referred to as A-, B-, and C-excitons. Under the influence of (1) spin-orbit and (2) the crystal field, the valance band split into Γ_9^V, Γ_7^V, and Γ_7^V sub bands which called usually A, B and C. The crystal field is depending on the ratio between the lattice parameters. A magnetic field

and/or a strain may alter these ratios and Γ_7^V, and Γ_9^V transform to Γ_5^V, and Γ_6^V [Reynolds[53], Chen[54] and Kitaev[55]].

III.B. OPTICAL PROPERTIES

III.B.1. Excitonic Absorption for GaN

In high quality GaN epilayers, low temperature absorption spectra are usually dominated by sharp excitonic resonances, as seen in Figure 8 [Song and Fisher[56]]. Since the concentration of impurities in these samples is relatively small, bound excitons are not expected to contribute significantly to band-edge absorption. At 10 K, we can clearly observe three different absorption features associated with A-, B-, and C-excitons.

Figure 8 also shows changes in absorption over the temperature range of 10 K to 450 K. An excitonic resonance is clearly observed in the 300 K absorption data. In fact, excitonic resonances were observed at least a hundred degrees above room temperature. The energy position of the A-exciton was found to be well approximated by the Varshni equation[95]:

$$E(T) = E(0) - \frac{AT^2}{B + T}, \qquad (8)$$

with $A = 11.8 \times 10^{-4}$ eV/K and $B = 1414$ K as seen in Figure 9.

Similar experiments were performed on InGaN and AlGaN epilayers. The InGaN epilayers usually exhibit a very wide absorption edge (several hundred meV) and have no excitonic features in absorption. Excitons have been observed in AlGaN epilayers at low temperatures[57], as shown in

Figure 10. The excitonic feature disappears for temperatures above 150 K. We further note that the abnormal temperature behavior of the band-gap in these alloys cannot be adequately fit by the Varshni equation. The difficulties in observing excitons in InGaN and AlGaN epilayers could be related to material quality. Once the quality of these ternary compounds is improved, we expect to see excitonic features in these materials over a wide temperature range. In this thesis, we mostly concentrate on the optical properties of GaN and AlGaN.

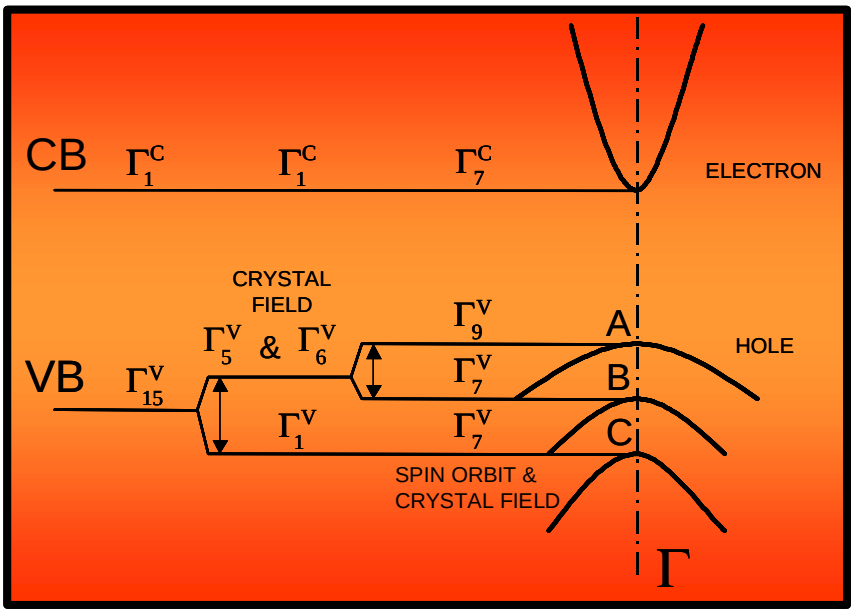

Figure 7. Structure and symmetries of the lowest conduction band and the uppermost valence bands in wurtzite GaN at the Γ-point ($k \approx 0$). [Adapted from ref. 59]

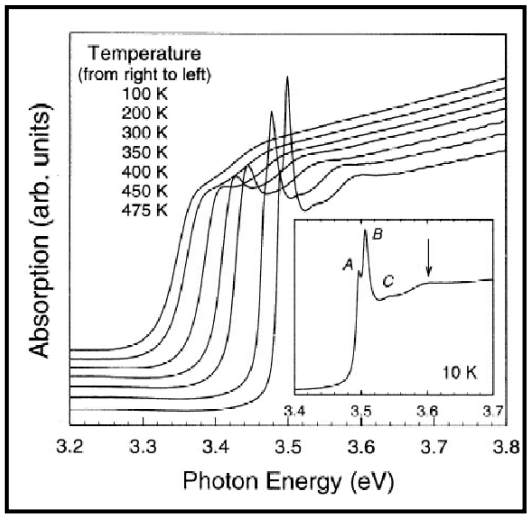

Figure 8. Absorption spectrum for GaN as a function of photon energy at different temperature. At 10 K, the A, B, and C excitons are clearly resolved showing the excitonic absorption due to the three valence bands. At room temperature, the A and B excitons overlap due to phonon broadening to form one peak while the C exciton appears as a change in slope. The inset is an expanded view of the excitonic structure at 10 K. The spectral feature indicated by the arrow in the inset is due to the contribution of the indirect exciton formation which creates an exciton and a LO phonon simultaneously.

[Adopted from ref. 56.]

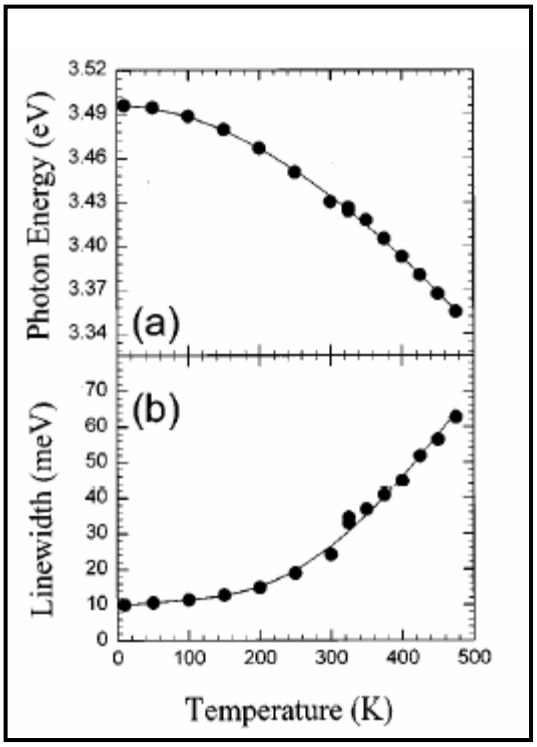

Figure 9. (a)Exciton energy position vs. temperature. The solid line is a fit to the Varshni equation, Eq. (8). (b)Exciton linewidth (FWHM) plotted as a function of temperature. [Adopted from ref. 56.]

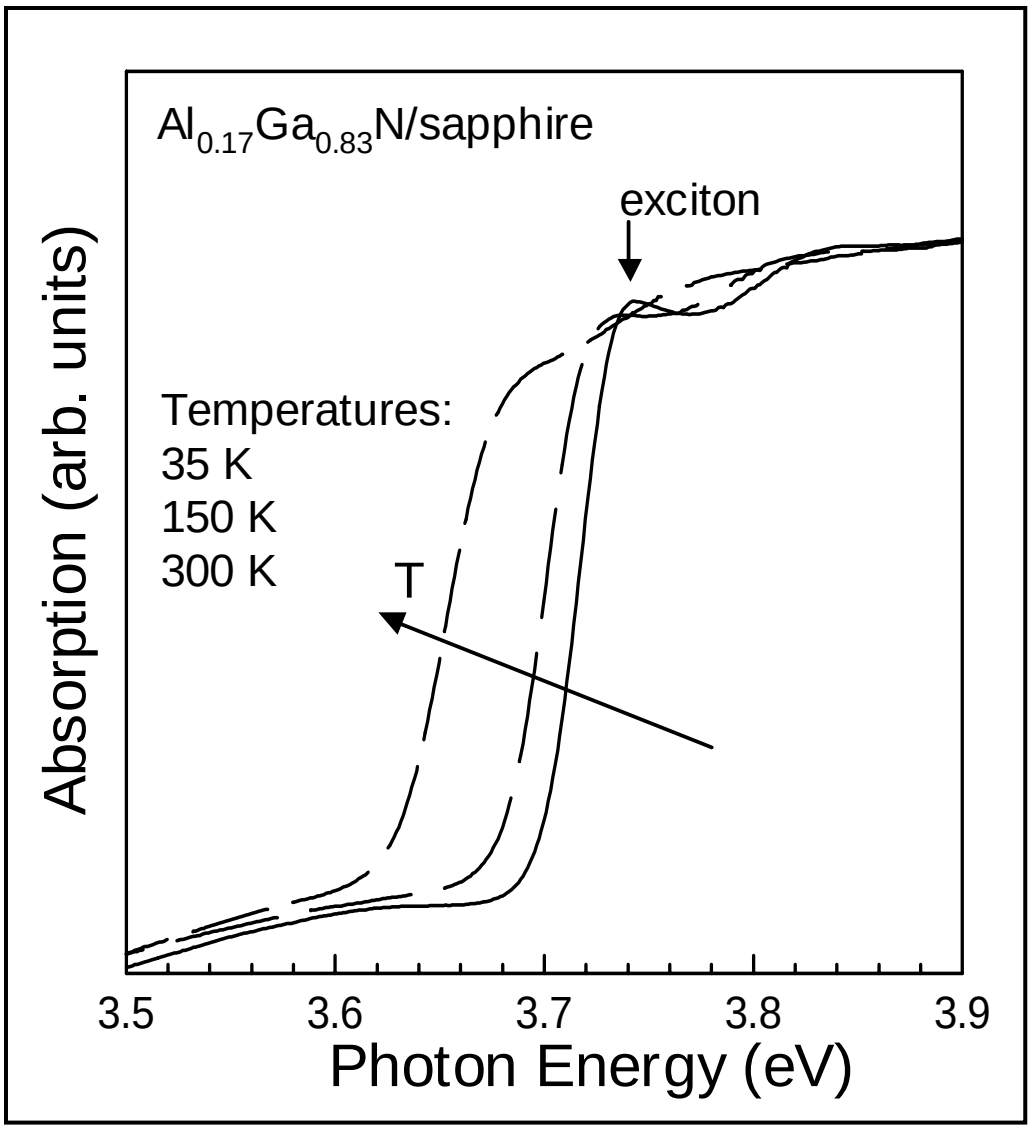

Figure 10. Absorption spectra of a 0.44 μm-thick $Al_{0.17}Ga_{0.83}N$ epilayer near the fundamental band-gap. At low temperatures, a weak excitonic feature is observed. [Adopted from ref. 58].

III.B.2. Near Bandgap Photoluminance (Excitonic Recombination in GaN)

Extensive work on the luminescence of III–nitrides (mostly GaN) has been done and several reviews have been published. Typical near band-edge PL spectra of GaN at different temperature is shown in Figure 11 after Song and Shan[59,60]. At low temperatures, the spectra are dominated by the BX peak due to recombination of excitons bound to impurities. BX has a full width at half maximum (FWHM) of less than 1.0 meV at 10 K while $FX_{n=1}^{A}$ shows a FWHM of less than 1.5 meV. As the temperature rises, the BX peak decays faster than the free exciton peaks marked $FX_{n=1}^{A}$ and $FX_{n=1}^{B}$ and all the peaks move to lower energies. The two peaks are due to the A and the B excitons i.e., due to transitions involving holes in the A (Γ_9^V) and B (Γ_7^V) valence bands.

At 75 K the A exciton peak becomes the strongest. It became hardly resolvable when the temperature was raised to above 100 K (not shown). Such effects of temperature on the luminescence intensity indicate the emission line resulting from radiative recombination of excitons bound to neutral donors[61]. Since the as grown GaN is generally, n type the BX peak is most likely due to the excitons bound to neutral donors so we may donate the bound exciton for GaN as DX. The rapid thermal quenching below 100 K implies that the exciton is bound very weakly; hence, it must be bound to a shallow neutral donor, not a deep donor, or an acceptor.

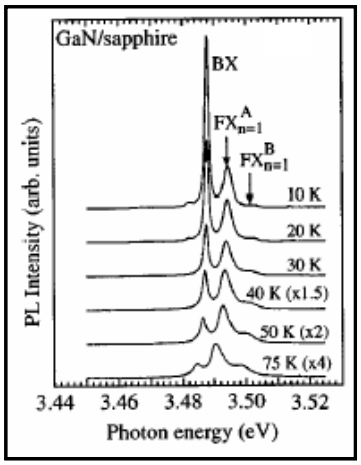

Figure 11. Near-band-edge exciton luminescence spectra taken from a 7.2 μm GaN epifilm grown on sapphire by MOVPE. (After Song and Shan, ref. 59,60).

III.C. Excitons and Strain in GaN Epilayers

Due to the lattice mismatch and difference in thermal expansion coefficients between GaN epilayers and substrates, one has to take into account the effects of residual strain when considering the excitonic energy transitions. Some degree of strain relaxation occurs through the formation of a large density of dislocations. However, the residual strain has a relatively strong influence on the optical properties of the sample.

Shown in Figure 12 is a comparison of reflection spectra taken from two GaN epilayers grown on sapphire and a GaN epilayer on SiC at 10 K. As clearly shown by the figure, the energy positions of the exciton resonances associated with A-, B-, and C-exciton transitions are substrate-dependent[59].

It is difficult to separate the effects of strain caused by lattice parameter mismatch from ones involving thermal-expansion mismatch to exactly determine their influence on the optical properties of GaN epilayers. However the overall effect of residual strain generated in GaN on sapphire is compressive, which results in an increased band-gap, while the stress induced in GaN on SiC is tensile, which leads to a decrease in the measured exciton transition energies. Figure 13 shows the photoluminescence spectra of GaN epilayer grown on sapphire and same epilayer freestanding GaN i.e. sapphire substrate has been removed by laser lift-off technique [Perlin et. al.[62]]. One can see that the luminescence from the sample on sapphire has a larger energy, indicating the presence of a compressive-biaxial strain. This strain is related to the difference between the thermal expansion coefficient of GaN ($5.59X10^{-6}$ K^{-1}) and that of sapphire ($7.5X10^{-6}$ K^{-1})[63] which causes a biaxial strain to develop during the sample cool down process from the growth temperature.

For vertical devices e.g. LED the emission from the surface. The growth of the epilayer is in the c-axis direction so the optical properties are dependent on the a-axis. In case of sapphire substrate, the a-axis is compressed and this led to blue shift. In case of SiC, the a-axis is stretched (tensile) and this led to red shift.

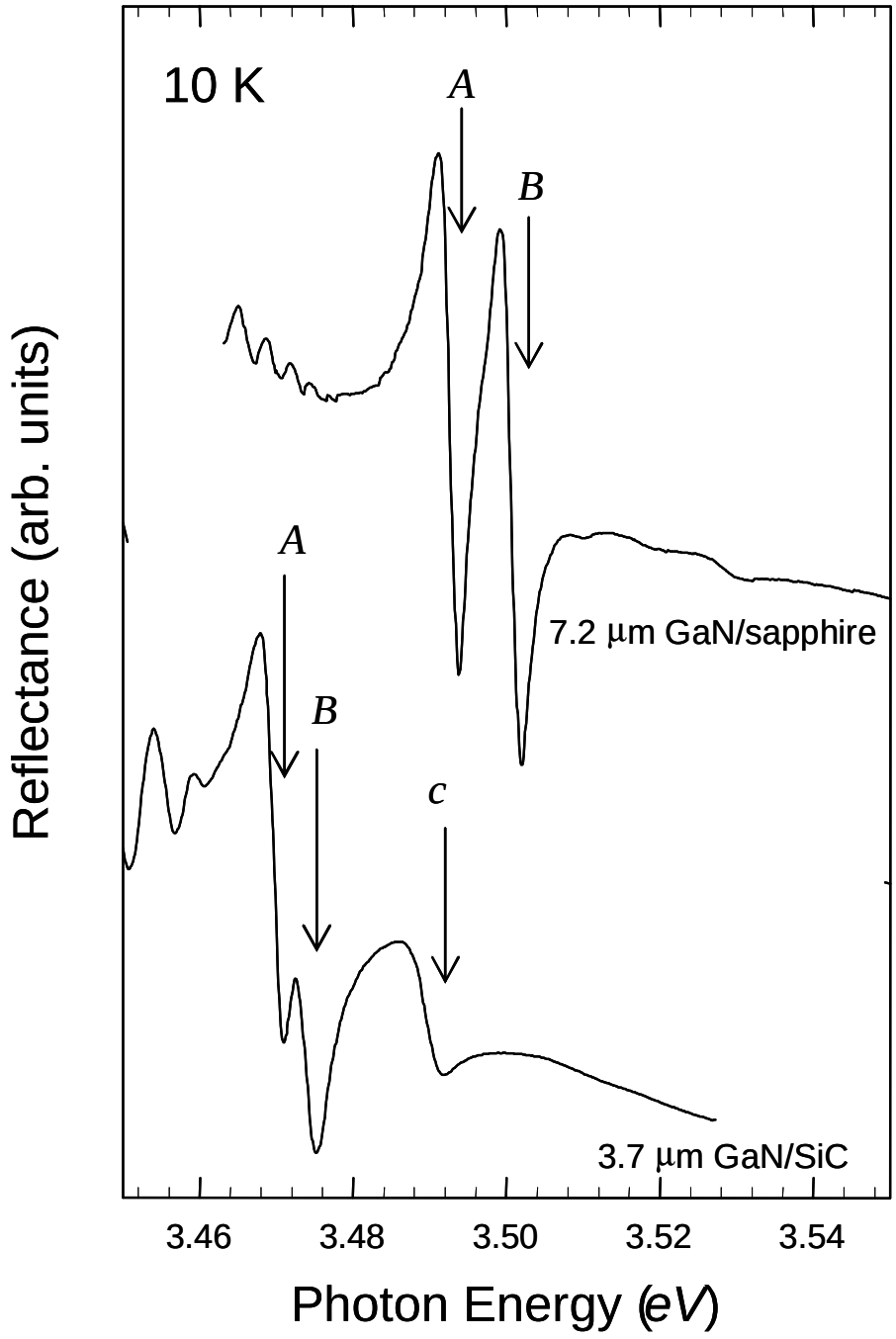

Figure 12. 10 K reflection spectra taken near the band edge of a 7.2 μm GaN/sapphire sample (top curve), and a 3.7 μm GaN/SiC sample (bottom curve). Various excitonic transitions are labeled. The curves are displaced vertically for clarity. [Adopted from ref. 59, page 192]

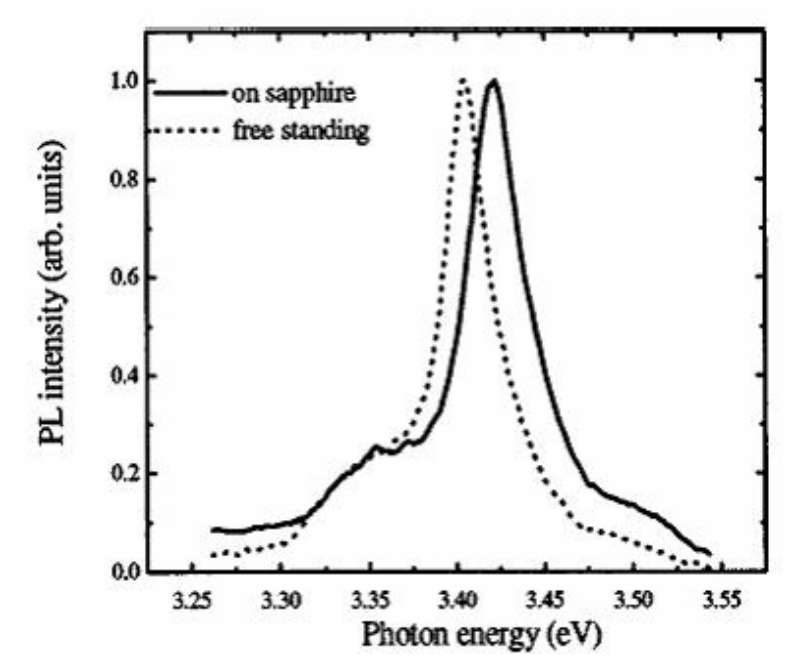

Figure 13. Comparison between Photoluminance spectra of 3 μm thick GaN epilayers grown on sapphire before and after the removal of the sapphire substrate. [Adopted from ref. 62].

CHAPTER IV

GROWTH TECHNIQUES AND SEMICONDUCTOR EPITAXIAL STRUCTURES

Bulk growth methods

The techniques used to grow III-Nitride can be split into two categories[64]: bulk and epitaxial. Bulk growth methods, such as vapor phase transport (VPT), seeded VPT (SVPT) and the hydrothermal method; traditionally use a seed crystal to grow a pure sample of the desired material. This procedure is roughly similar to the elementary experiment of creating sugar crystals from a saturated solution of sugar in water using a single sugar crystal as the seed. Semiconductor samples grown by this method are usually of extremely high crystalline quality, but often suffer from small lateral dimensions. It is common for bulk samples to have thicknesses of several mm (extremely thick compared to the typical epitaxially grown sample thickness of from nm - μm), but their lateral dimensions are usually limited to the mm regime as well.

Bulk GaN crystals up to 100 mm^2 have been grown by Unipress (High Pressure Research Center of the Polish Academy of Sciences, Warsaw) and exhibit extremely high crystalline quality, as determined by X-ray diffraction, photoluminescence, and

transmission electron microscope (TEM) measurements. Homoepitaxial layers of GaN grown on top of these bulk samples by molecular beam epitaxy (MBE) or metal organic chemical vapor deposition (MOCVD) are of unmatched quality[65,66]. The same group grew ultra low dislocation density (below 10^2 cm^{-2}) using high-nitrogen-pressure-solution-growth (HNPSG) technique. however the growing time still too long, from 120 to 200 hours for growing in the direction parallel to the c-axis [Porowski et. al.[31]].

Epitaxial growth techniques

1. Metal organic chemical vapor deposition (MOCVD) technique

MOCVD involves heating a suitable substrate material to high temperatures and flow of a combination of gases, which contain the constituent atoms of the material being grown, across the substrate. Some of the atoms stick to the substrate and arrange themselves in a well-defined crystallographic lattice. The detailed growth kinetics of semiconductors is beyond the scope of this thesis. For a more in-depth discussion of this topic, see Ref. [67]. There are many different variations of the MOCVD growth technique, including horizontal and vertical reactor designs, the two-flow method, and atmospheric and low-pressure growth. In addition, there are many variables related to growth that can be changed to produce different quality samples, such as growth temperature and source precursors. To make matters even more complex, the conditions for optimum growth usually vary from one material to another. For example, the substrate temperature can change substantially for different materials (1050-1100 C° for

GaN and AlGaN), (550 C° for InGaN), and can make the growth of alloys and/or heterostructure challenging.

2. Molecular beam epitaxy (MBE)

High quality epilayers have also been grown using MBE. MBE is similar to the MOCVD growth technique, but instead of gases flowing across the substrate, it involves sputtering source materials from heated crucibles in an ultrahigh vacuum environment. Both MOCVD and MBE are capable of producing extremely thin epitaxial layers, allowing the controlled growth of complex device structures (see next section).

3. Hydride vapor phase epitaxy (HVPE)

HVPE is important because it allows the growth of samples that are very thick compared to the typical 1-2 μm samples grown by MOCVD or MBE and at faster rate. The well-recognized benefits of GaN HVPE growth technology have included low production cost, high material quality, and high growth rate. HVPE has become an important growth technique for GaN, since it is a cost-effective way of growing thick, high quality GaN with growth rates of up to 100 μm/h [Ref. 68]. In the last few years, HVPE provided bulk GaN template, and low dislocation densities, which used as a substrate for GaN epilayer grown with other methods.

4. Pulsed laser deposition (PLD)

PLD is another technique that has been used to produce III-Nitride materials, but usually the quality is low compared to other techniques.

Semiconductor Epitaxial Structures

There are many complex structures that can be grown by the above mentioned growth techniques[64]. The crystal grower can directly control the alloy composition, dopants, layer thicknesses, and growth temperatures to grow samples for a wide range of potential applications. Some of the most common structures with an emphasis on those that are used in the research presented in later chapters will be introduced here.

Heterostructure

Using modern epitaxial method, such as molecular beam epitaxy (MBE), metal organic chemical vapor deposition (MOCVD) or HVPE, it is possible to deposit two different semiconductors on one another in a crystalline form[64]. These semiconductors will generally have different electronic properties, and in particular different band gaps. Such layer structures play a particularly important role in devices made from III-V semiconductors such as GaAs, InP and recently group III nitride.

The structure consisting of two different semiconductors layers grown epitaxially on one anther is called a semiconductors heterostructure. The width of the transition regions between the two semiconductors can be as little as one atomic layer if a suitable

epitaxial method is used. In such a heterostructure the band gap changes over distances of atomic dimensions.

Figure 14 shows the band scheme for a heterostructure formed from semiconductor I and II. When the two semiconductors are in contact, but not at thermal equilibrium because the Fermi levels E_F on the two sides have not equalized[72]. ΔE_C and ΔE_V are the band gap discontinuities in the conduction and valance bands, respectively.

In thermal equilibrium Figure 15, the Fermi energies E_F in I and II must be identical. Since the band discontinuities ΔE_C and ΔE_V are predetermined, band bending must occur in the two semiconductors. The band bending allows carriers to be confined in a quasi-triangular quantum well region, a fact that becomes extremely useful to create a two-dimensional electron gas (2DEG).

2DEG and High Electron Mobility Transistor (HEMT)

According to semiconductor theory, the semiconductor layer needs to be doped with n-type impurities to generate electrons in the layer. However, this procedure causes the electrons to slow down because they end up colliding with the impurities residing in the same region that were used to generate them in the first place.

HEMT is a smart device that was designed to resolve this contradiction. HEMT stands for High Electron Mobility Transistor. A HEMT is a Field effect transistor

(FETs) [69] with a junction between two materials with different band gaps i.e. heterojunction as a channel instead of an n-doped region. The effect of this junction is to create a very thin layer where the Fermi level energy is above the conduction band, giving the channel very low resistance i.e. “high electron mobility". This layer is sometimes called a two-dimensional electron gas (2DEG). In other words, the hetero-junction created by different band-gap material forms a steep canyon in the narrower band gap side where the electrons can move quickly. As with all the other types of FETs, a voltage applied to the gate alters the conductivity of this layer. A commonly used HEMT combination is GaAs with AlGaAs.

HEMT played an important role for better understanding of the quantum machines theory. In February 1980, Dr.Klitzing of West Germany measured the two-dimensional electron gas of metal oxide semiconductor field effect transistor (MOSFET) in an environment exposed to ultra low temperatures and high magnetic fields at Grenoble Research Center France. As a result of taking these measurements, Dr. Klitzing discovered "the quantum Hall effect". He published his findings in the Physical Review Letter[70]. Dr. Klitzing was awarded the 1985 Nobel Prize in Physics for this achievement.

Also, in March 1982, researchers led by Dr. Tsui of Bell Laboratories measured the properties of electron gas on a two-dimensional plane in GaAs/AlGaAs heterojunction using extremely powerful magnetic fields and extremely low temperatures. Then, they discovered "the fractional quantum Hall effect". In 1982, Dr. Laughlin, Stomer, and Tsui were awarded the 1998 Nobel Prize in Physics for this achievement. The discoveries of

the quantized and fractional Quantum Hall Effect phenomena are among the most important quantum physics findings.

AlGaN/GaN High Electron Mobility Transistors (HEMT)

The Group III-nitrides (AlN, GaN, InN, and their alloys) were initially researched for their promise to fill the void for a blue solid state light emitter[71]. GaN, in particular, received considerable attention because of its direct energy gap of 3.39 eV (365 nm). Electronic devices from III-nitrides have been a more recent phenomenon. One of the most noteworthy advantages of the III-nitrides over other wide band gap semiconductors, such as SiC, is the availability of AlGaN/GaN heterostructure and the large conduction band offset between GaN (Eg = 3.39 eV) and AlN (Eg = 6.2 eV) at 300 K. The band alignment between AlGaN and GaN has been shown to form a quasi-triangular potential well and a 2-dimensional electron gas (2DEG) at the heterointerface with extremely high sheet density ~10^{13} cm^{-2} in contrast with AlGaAs/GaAs sheet density ~10^{12} cm^{-2}. When these materials are brought into contact, thermal equilibrium requires alignment of their respective Fermi levels (E_F). This induces conduction (E_c) and valence (E_v) band bending in both the AlGaN and GaN layers and can cause the GaN conduction band at the interface to drop below E_F, as illustrated in Figure 16.

Since (for n-type material) the Fermi level can be viewed as an electrochemical potential for electrons, majority electrons will accumulate in the narrow gap material just below the heterointerface to fill the quasi-triangular potential well between E_c and E_F.

These electrons are confined by a distance shorter than their deBroglie wavelength, causing quantization of the allowed energy levels in the potential well. Depending on the structure, there may be more than one allowed energy level below the Fermi level. Usually the lowest allowed level will be substantially populated at room temperature. With the heterointerface on one side and a potential barrier on the other, electrons in the 2DEG are only free to move in along the plane of the interface, therefore a thin 'sheet' of negative charge (electrons) results.

The group III-nitride materials can exhibit 2DEG mobility approaching 2000 cm^2 / V·s at 300K. Combined with the sheet charge density of ~10^{13} cm^{-2} and large peak and saturation velocities, AlGaN/GaN heterojunction field-effect transistors (HFETs) are capable of handling large DC and RF currents. HFETs have been by far the most heavily investigated III-N electronic device, largely due to their promise in the radio frequency semiconductor market. The thermal conductivity of GaN is three times that of GaAs, as listed in Table 1. For high power or high temperature applications, good thermal conductivity is imperative for heat removal or sustained operation at elevated temperatures. The development of III-N and other wide band gap technologies for high temperature applications will likely take place at the expense of competing technologies, such as silicon-on-insulator (SOI) at moderate temperatures. At higher temperatures (>300°C), novel devices and components will become possible. The automotive industry will likely be one of the largest markets for such high temperature electronics. Automotive control components fabricated with wide bandgap materials could be mounted directly to an engine block, reducing signal delay. Well logging equipment, military combat systems, and aerospace components are just a few of the additional

sectors in the global market for these devices. Figure 17 illustrate the basic operation of the HEMT.

To summarize many of the attractive features of the group III-nitrides, selected material properties of AlN, GaN, and InN relevant to electronic device applications are listed in Table 1 along with those of Si, GaAs, SiC, and diamond at room temperature.

In chapter VIII, we will investigate strain and piezoelectric electric effects on the optical and electrical characterizations of $GaN/Al_{0.2}Ga_{0.8}N$ heterostructure grown by HVPE for HEMT applications.

Double heterostructure

Another common semiconductor structure is the double heterostructure (DH)[64], pictured in Figure 18. A DH consists of an active region in the center and two surrounding cladding layers. The basic principle design of a DH is to combine the confinement of photons with the confinement of carriers. The carrier confinement effect results from the desire of carriers to seek out the lowest energy level available. Once they drift or diffuse into the active region and get rid of their excess kinetic energy, they cannot escape. They are confined to this narrow volume.

Optical confinement arises from the difference in refractive index between the active region and the cladding regions. If the materials are chosen correctly, the difference in refractive index between these two layers will cause total internal reflection for light emitted in certain directions. This light will propagate through the sample with

minimal loss until it escapes at the end of the cavity. The confinement of light is crucial for laser diodes (LDs), specifically for the efficient extraction of gain from the laser cavity and for keeping the far-field emission pattern relatively small.

The quantum well (QW).

One of the most commonly grown structures is the quantum well (QW)[64]. A QW consists of a thin layer of semiconductor material typically on the order of several nm, sandwiched between the so-called barrier layers which have a larger band gap value. A QW well structure is similar to double heterostructure but the active layer is much thinner which yields more photons and carriers confinements. This effect can be very advantageous for certain devices such as laser diodes (LDs). This is shown schematically in Figure 19 (a), with the well width denoted by L_w. The most common way to create these wells is by epitaxially growing alloy systems, *e.g.* GaAs/$Al_xGa_{1-x}As$ or $In_xGa_{1-x}N$/GaN for the well/barrier.

One QW all by itself is referred to as a single quantum well (SQW). When the barrier regions are also relatively thin and there is more than one well, as seen in Figure 19 (b), the structure is known as a multiple quantum well (MQW). The barrier width is given by L_b. The difference in well and barrier bandgap energies, $\Delta E_g = \Delta E_g(\text{barrier}) - \Delta E_g(\text{well})$, is known as the band offset, and allows carriers to be confined in the well region, a fact that becomes extremely useful when one wishes, say, to create a two-dimensional electron gas (2DEG), generate a population inversion, or simply create a region in which a large number of carriers will reside.

Because of the extremely narrow dimensions in the growth direction of SQWs or MQWs and the wave-particle duality nature of electrons, quantized states form according to the laws of quantum mechanics (similar to the infamous "particle in a box" problem). These states have an energy larger than the band gap energy of the well material due to the quantum confinement effect (see the quantum states n = 1, 2, … in Figure 19 (a). As can also be seen in Figure, the total band offset ΔE_g can be split into two parts: the valence band offset (ΔE_v) and the conduction band offset (ΔE_c). The ratio of these two offsets is dependent on the materials used in the structure, and is an extremely important parameter in the design of efficient optoelectronic devices.

For the GaAs/AlGaAs system shown in the figure here, $\Delta E_v = 0.15\ \Delta E_g$, and $\Delta E_c = 0.85\ \Delta E_g$, thus $\Delta E_c/\Delta E_v = 5.7$. MQWs are very useful structures and are commonly employed as active regions in LEDs and LDs.

Separate confinement heterostructure (SCHs)

Separate confinement heterostructure (SCHs) play an extremely useful role in device physics[64]. A typical SCH structure is shown in Figure 20. As its name suggests, an SCH provides two separate confinement regions – a narrow one in the center of the structure to confine carriers, and a wider one symmetric about the center to confine the output light from the device. The center region, called the active region, consists of a narrow (~ 100 Å) layer of semiconducting material. Both sides of the active region are bordered by thicker layers of material with a larger bandgap energy called waveguide regions. Symmetrically located around the waveguide regions are thick layers of material

with an even higher bandgap energy called cladding regions. By using a widely spaced layer of material with lower index of refraction around the active region to confine the light output of the device, the junction region can be made extremely thin without refracting the emitted light out of the cavity. Thus, SCHs combine the quantum effects of QWs and the optical confinement properties of DHs, both of which can be very advantageous for creating efficient devices.

There are many other important semiconductor device structures but they are out of the scope of this thesis.

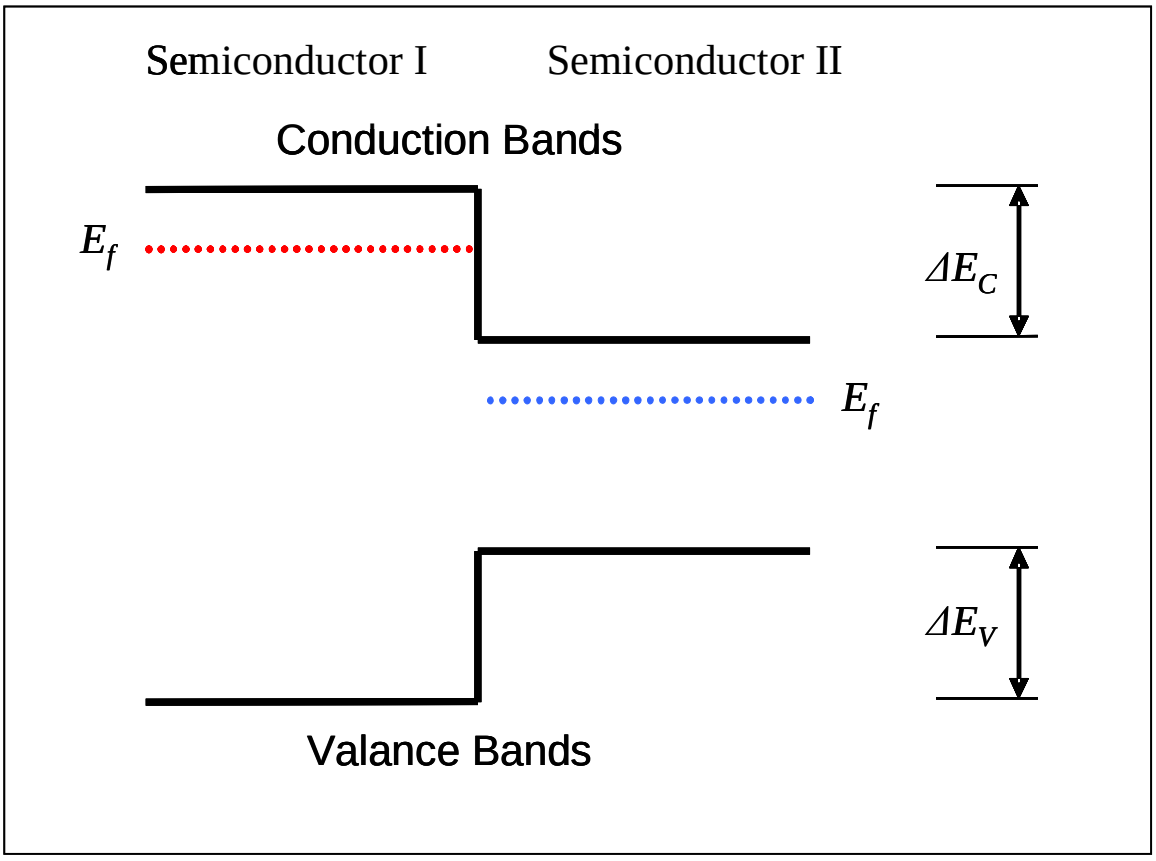

Figure 14. The band scheme for a heterostructure formed from semiconductor I and II. When the two semiconductors are in contact, but not at thermal equilibrium because the Fermi levels E_F on the two sides have not equalized, ΔE_C and ΔE_V are the band gap discontinuities in the conduction and valance bands, respectively. [Adapted from ref. [72]]

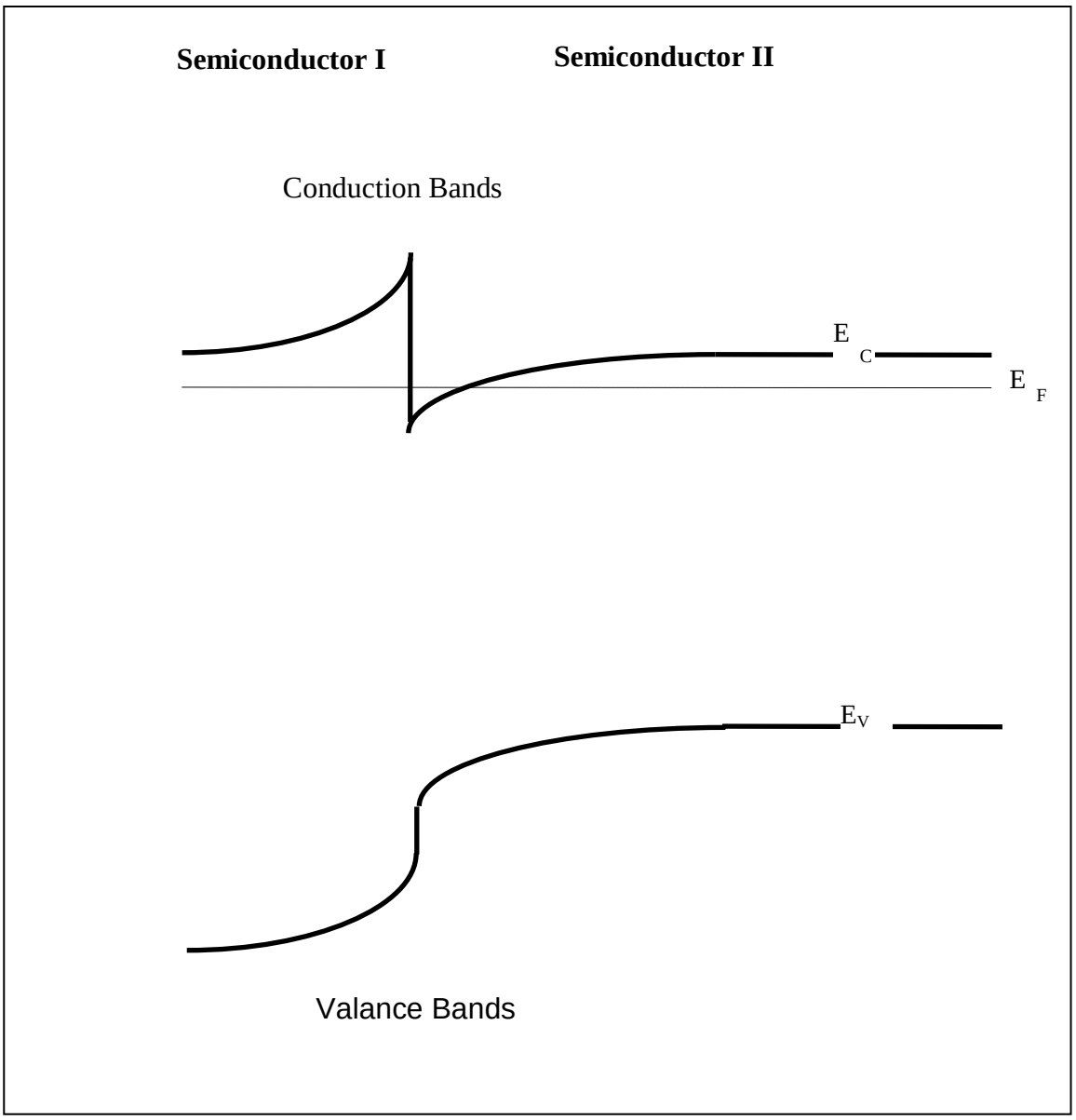

Figure 15. In thermal equilibrium, the Fermi energies E_F in semiconductors I and II must be identical. Since the band discontinuities ΔE_C and ΔE_V are predetermined, band bending must occur in the two semiconductors. A quasi-quantum well is formed at the interface of the conduction bands of the two semiconductors.

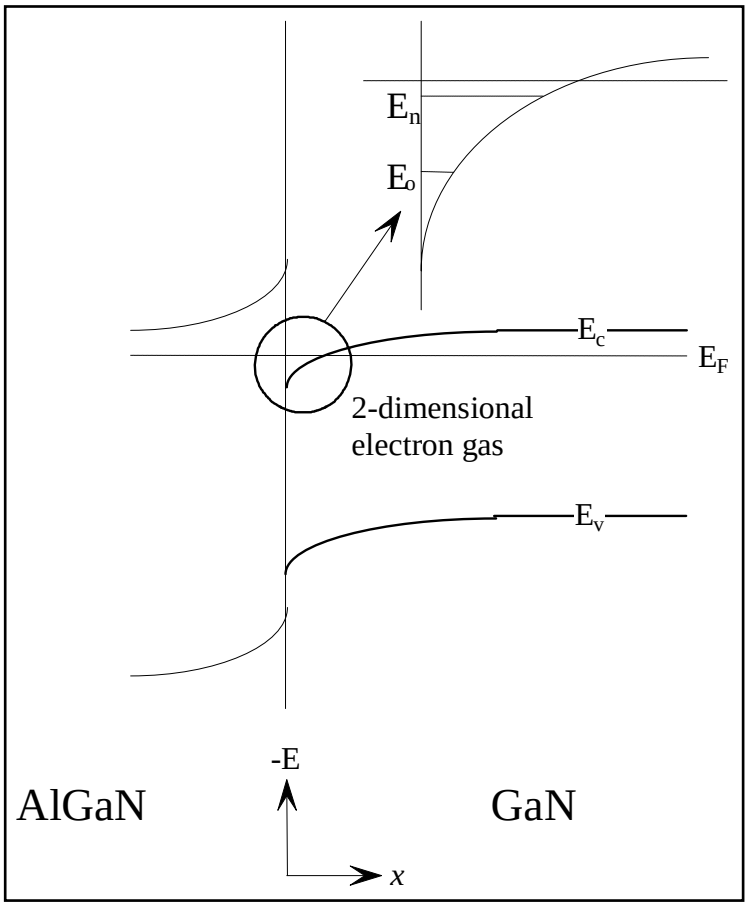

Figure 16. Formation of two dimensional electron gas (2DEG) at GaN/AlGaN heterostructure interface. [Adopted from ref. [73]]

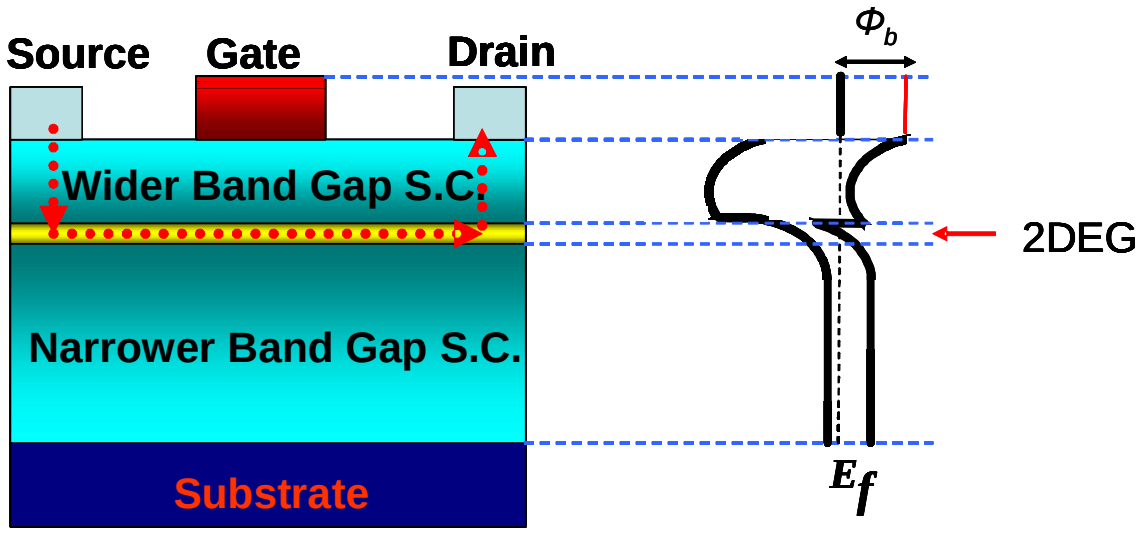

Figure 17. The basic operation of HEMT. The large band gap offset between the two semiconductors bend their conduction bands, thus creating 2-dimensional electron gas (2DEG) at the interface. This creates a high electron density sheet at the interface and enhances the electrons mobility by avoiding the electrons scattering by the impurities. The gate polarizes the electrons to confine more in the 2DEG. By altering the gate voltage, the rate of flow of the electrons through the 2DEG channel can be controlled.

Table 1. Selected 300 K material properties relevant to electronic device applications for Si, GaAs, and wide band gap semiconductors [74,75,76].

Property (at Room temperature)	Si	GaAs	4H-SiC	Diamond	InN	α-GaN (AlGaN/ GaN)	AlN
Energy Band gap, E_g (eV)	1.12	1.42	3.25	5.45	1.89	3.4 (for GaN)	6.2
Saturated Electron Velocity, v_{sat} ($\times 10^7$ cm/s)	1.0	1.0	2.0	2.7	2.5	2.5 (2.7)	1.4
Peak Electron Velocity, v_{max} ($\times 10^7$ cm/s)	--	2.1	--	--	4.3	3.1	1.7
Breakdown Field, E_B (MV/cm)	0.3	0.6	3	10	--	3	--
Electron Mobility, μ_n (cm^2 / V·s)	1400	8000	800	2200	3200	900 (2000)	135
Hole Mobility, μ_p (cm^2 / V·s)	500	400	50	1600	--	50	14
Static Dielectric Constant, ε_s	11.8	12.8	9.7	5.5	15.3	9.5	8.5
Thermal Conductivity, κ (W/cm·K)	1.5	0.5	4.9	20-30	--	1.3	2.85

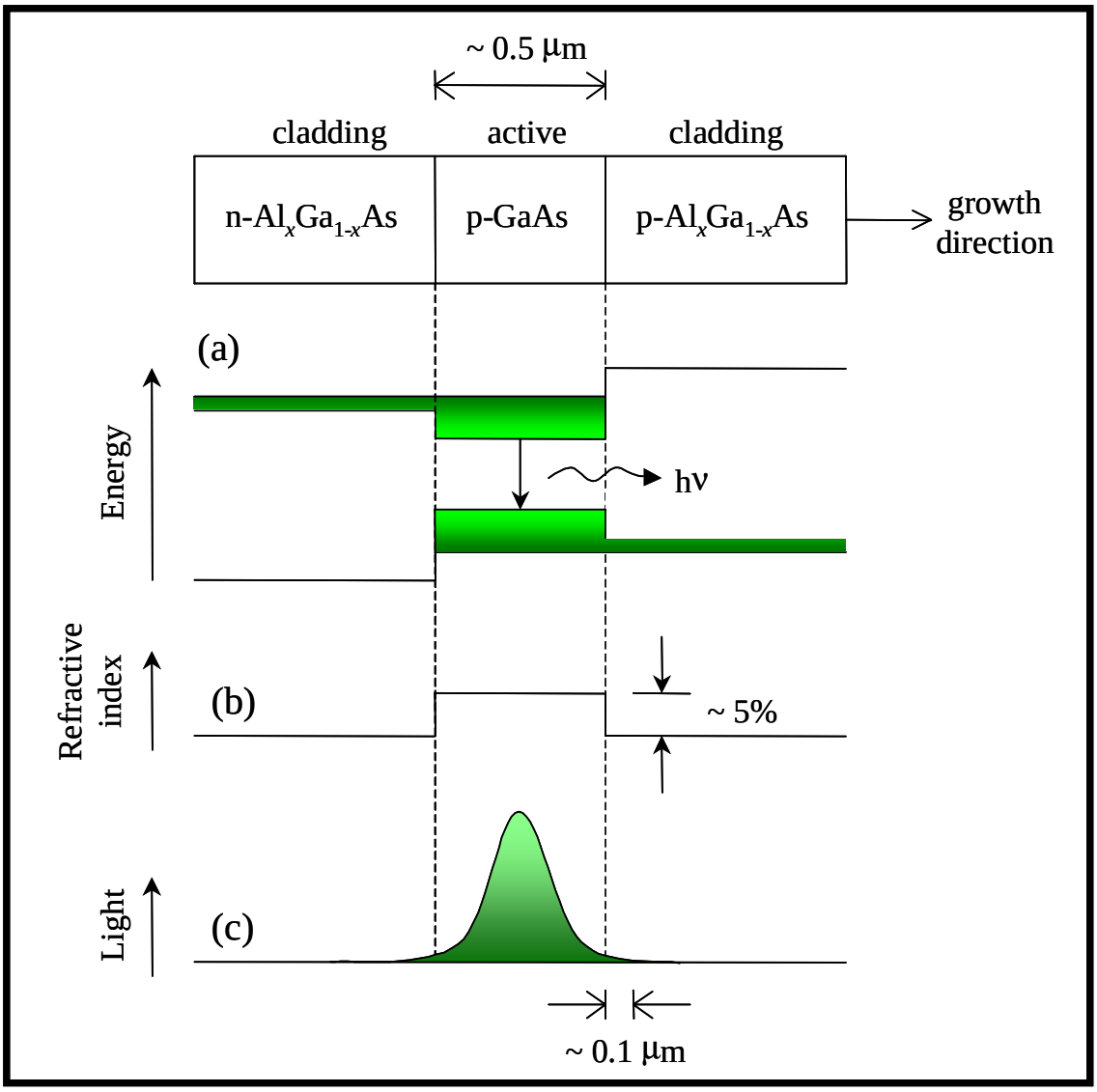

Figure 18. Schematic design of a double heterostructure (DH) fabricated using the GaAs/AlGaAs material system. The dimensions and energy band diagrams of the various layers are given in (a), the change in refractive index is shown in (b), and the confinement of light is given in (c). [Adapted from ref.[77]].

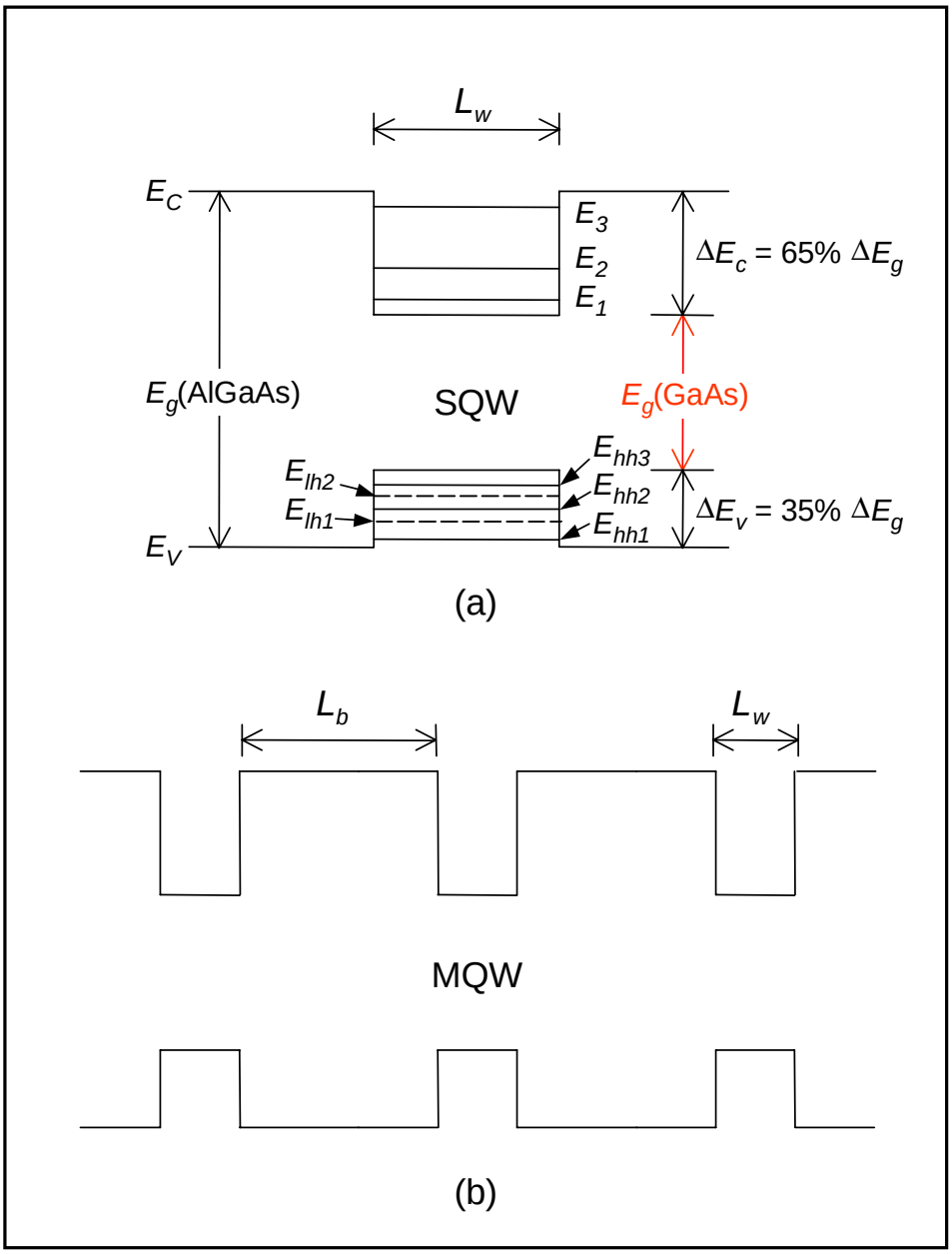

Figure 19. Schematic diagram of (a) single quantum well (SQW) and (b) multiple quantum well (MQW) structures. The quantum confined energy levels in the conduction band are denoted by E_n, where n = 1, 2, …, and those in the valence band are given as E_{hhn} where n = 1, 2, … (for heavy holes) and E_{lhn} where n = 1, 2, … (for light holes). Barrier and well width are denoted by L_b and L_w, respectively. The values of conduction band offset (ΔE_c) and valence band offset (ΔE_v) are also given for the GaAs/AlGaAs material system. [Adapted from ref. 64 and 78]

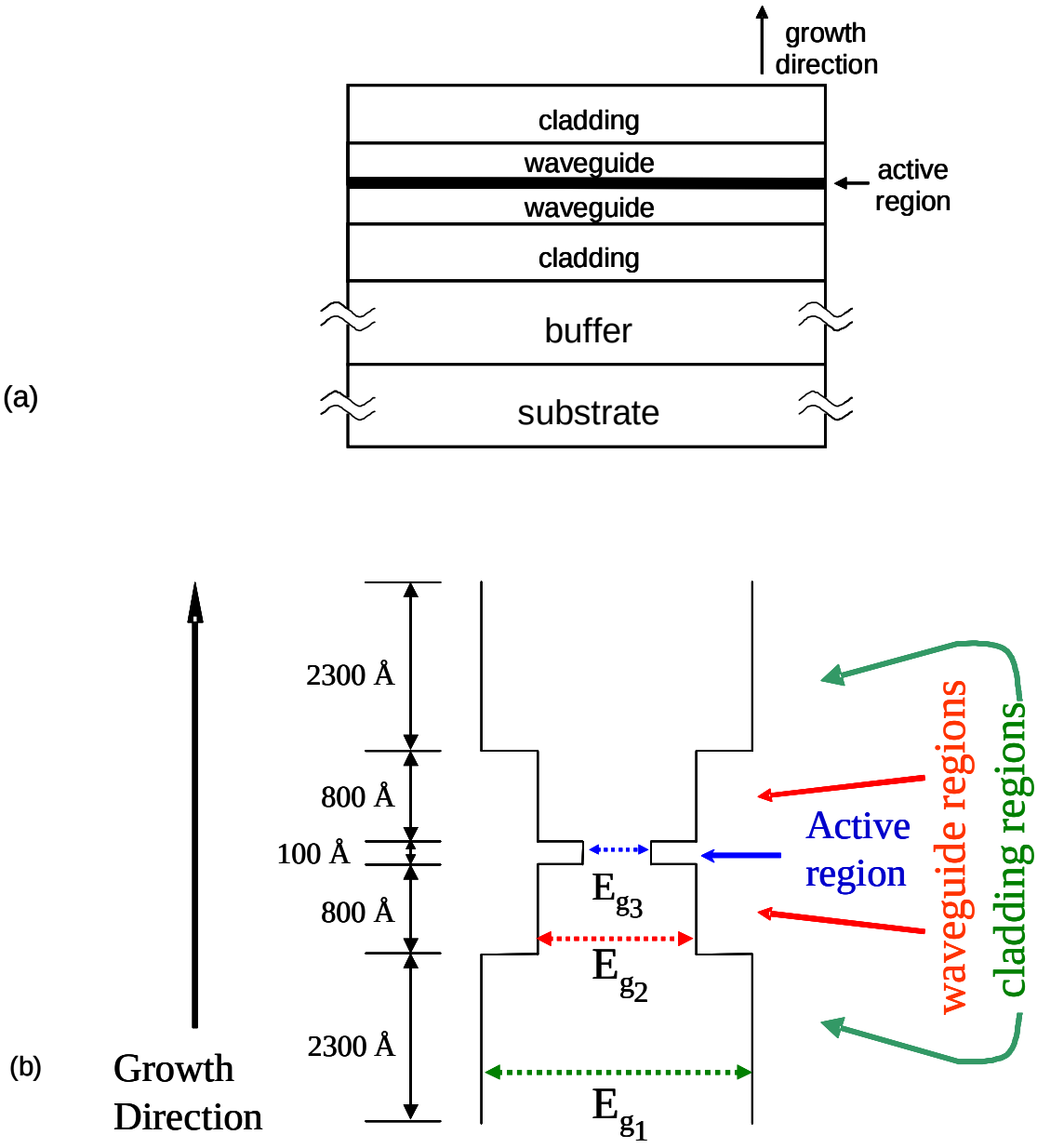

Figure 20. (a) Schematic drawing and (b) Schematic energy-band diagram of a typical separate confinement heterostructure (SCH). [Adopted from ref. 64]

PART II

EXPERIMENTAL INVESTIGATIONS

CHAPTER V

EXPERIMENTAL METHODS

Optical experiments essential to characterize semiconductor materials. Studying the interaction of photons with a semiconductor can yield direct insight into the physical processes taking place in the sample[64]. The knowledge gained through these experiments is useful in many ways, particularly in:

(1) Characterizing the optical properties of the material (*e.g.* refractive index, phonon energies, or exciton binding energy) or
(2) Assessing the optical quality of the material (e.g. stimulated emission or lasing threshold, luminescence efficiency, or emission wavelength).

The latter of these two seems more exciting, since it deals with actual devices, but the former is an extremely useful process. To be able to grow high quality devices, the research community must know the general optical constants of the material they are growing.

This chapter will introduce several of the most important optical characterization techniques in detail, with an emphasis on the experiments that were used in the research

performed by the author that is presented in this thesis. The experiments described here are, in order of presentation, photoluminescence, photoluminescence excitation, time-resolved photoluminescence, stimulated emission, absorption, photoabsorption, reflectance, and photoreflectance.

Photoluminescence (PL)

Photoluminescence (PL) is perhaps the basic of all the optical experiments used to characterize semiconductors. Figure 21 shows the basic PL experimental setup. The light source PL experiment could be a cw laser or a high power broadband lamp, e.g. Xe lamp, with the desired optical filter or a monochromator. Usually nowadays a laser light is used in PL experiments. The light beam is incident on a semiconductor crystal being studied. PL is commonly performed in the surface-emitting geometry, pictured in Figure 22.

For studying materials with band gap energy in the UV, a HeCd 325 nm or a frequency-doubled Ar^+ laser are commonly used, with a cw incident power of few mW to quite few tens of mW. The wavelengths used for the research performed by the author were 325 nm and 244 nm for HeCd and frequency-doubled Ar^+ lasers respectively. The laser light, which has photon energy greater than the band gap of the material being studied, excites electrons in the sample from the valence band to the conduction band. The vacant site left by the excited electron is called a hole and effectively has a positive charge. When an electron relaxes back down to the valence band (*i.e.* an electron recombines with a hole), a photon is emitted. These photons are collected and focused

into a spectrometer in which a diffraction grating disperses the light emitted from the sample into its constituent wavelengths and focuses a specific range of wavelengths on an output slit leading to a detector. Detection can be accomplished by two techniques, which involve different pieces of equipment.

The first technique makes use of a photomultiplier tube (PMT). This device converts incident photons into electrons, amplifies the electrons, and then measures the current flowing through a resistor due to these electrons. PMTs are extremely sensitive detectors and have a very good signal-to-noise ratio. Because the photons are converted to electrons, however, a PMT doesn't have the ability to discriminate between photons of different wavelength. Thus, the output slits of the spectrometer are made as narrow as possible and the grating must be scanned.

The second technique uses a Charge Coupled Device (CCD), which consists of a two-dimensional array of photodetectors. Because of the array nature of the CCD, and by fully opening the output slits of the spectrometer we can concentrate a range of wavelengths of light on different pixel areas on the detector. This allows the CCD to take spectrally resolved data in just one step; the grating does not need to be scanned. Although the data acquisition rate is must faster for CCDs, the signal-to-noise ratio and sensitivity are lower than that of PMTs. All PL measurements performed by the author and described in later chapters were achieved using the PMT as a detector.

The information obtained from PL results gives the researcher important insight into the radiative recombination processes in the semiconductor. The wavelength or energy position of the emitted light is usually the most important information gained through PL. This can tell us many important things about the sample, such as the value of strain in epitaxial layers, the crystalline type of the sample (*e.g.*, wurtzite GaN has a different bandgap energy than zincblende GaN), the composition of alloy materials, and can indicate the presence of quantized levels in separate confinement heterostructure (SCHs) or quantum wells (QWs). The intensity of the emission gives an idea as to the luminescence efficiency, which is important in designing bright light emitting devices. The width of the emission line, measured by the full width at half maximum (FWHM), gives information about the optical quality and homogeneity of the samples.

Photoluminescence Excitation (PLE)

Photoluminescence excitation (PLE) is an experiment that lets us examine which energy levels in a semiconductor contribute to a certain PL emission line. This is done by setting the detection wavelength at the desired PL line and scanning the excitation source (on the high energy side, since we don't expect to see any up conversion). In a sense, we are probing the higher energy bands to see which ones relax radiatively down by the PL transition in question. The experimental setup is shown in Figure 23. PLE can help classify the recombination mechanisms involved in radiative transitions. For instance, by studying the PLE spectra of GaN epilayers, Shan *et al.* determined the

relaxation scheme of hot bound and free excitons through longitudinal optical (LO) phonon and acoustic phonon emission[79].

Time-Resolved Photoluminescence (TRPL)

Time-resolved PL (TRPL) is an extremely important tool in semiconductor research that allows us to study the temporal profile of PL spectra. Several major changes must be made to the PL setup described in the previous section to allow for the acquisition of temporally resolved spectra[64]. A typical TRPL setup is shown Figure 24. It is absolutely necessary that a pulsed laser be used. The pulse duration and repetition rate of this laser can vary, but keep in mind that the minimum temporal resolution of the TRPL system is determined by the following three factors:

(1) The laser pulse duration.

It is necessary to make sure the pulse duration of the laser is considerably shorter than the luminescence lifetime being measured, *i.e.* a picosecond PL signal can't be measured using a nanosecond laser.

(2) The reaction time of the detector.

The appropriate detector must be used. Several choices exist, including photodiodes (~ 1 ns typical resolution, sampling units available down to several hundred ps), photon counting PMTs (~ 50 ps), and streak cameras (~ 2 ps).

(3) Various dispersive elements in the optical path such as spectrometers and lenses.

The third factor only comes into play when working at the extreme low end of the temporal resolution scale. To attain the minimum band width (maximum resolution) possible, it is necessary to keep the pump and collection beam paths as clear as possible. This means using thin lenses and cryostat windows, and even using bandpass filters instead of a spectrometer for spectral resolution.

The TRPL data presented in this thesis was taken using a streak camera. This apparatus allows the simultaneous measurement of PL intensity and wavelength versus time. The software lets us choose the region of this 3D data set to analyze: we can look at the temporal profile of a narrow wavelength range (TRPL) or at a snapshot of the whole spectrum at a certain time (TIPL).

TRPL is important because it provides a direct measurement of the decay time of photoexcited carriers. The recombination of localized carriers is governed not only by radiative recombination but also by the nonradiative transfer to and trapping in energy tail state[80]. The effective carrier lifetime τ_{eff} is given by

$$\frac{1}{\tau_{eff}} = \frac{1}{\tau_R} + \frac{1}{\tau_{NR}}. \qquad (9)$$

where τ_R and τ_{NR} are the radiative and nonradiative lifetimes in the semiconductor respectively. The nonradiative processes include multiphonon emission, capture and recombination at impurities and defects, Auger recombination, and surface recombination, as well as diffusion of carriers away from the region of observation.

Assuming a radiative efficiency of 100% at T = 10 K, the radiative efficiency as a function of temperature is expressed as[64]

$$\eta(T) = \frac{\tau_{eff}(T)}{\tau_R(T)} \approx \frac{I_{PL}(T)}{I_{PL}(T = 10K)} \qquad 10$$

From the above two equations, one can determine the radiative and nonradiative lifetimes as a function of temperature. This is a necessary step in the design, growth, and evaluation of light emitting devices, where short radiative lifetimes and long nonradiative lifetimes detrimentally affect performance.

Optical Pumping (Stimulated Emission and Lasing)

First, let's discuss the difference between stimulated emission (SE) and lasing. Both of these terms fall under the category of optical pumping experiments. Stimulated emission is a physical process of light emission. When an atom, ion, or molecule is excited to a higher energy by an electromagnetic field or a photon it will spontaneously emit a photon as it decays to the normal ground state. If that photon passes near another atom which emits light of the same frequency as the incident photon and is also at some metastable energy level, the second atom will be stimulated to emit a photon. i.e. the stimulated emission adds a photon. Both photons will be of the same frequency, polarization state, direction and phase as the stimulated wave.

On the other hand, lasing (light amplification by the stimulated emission of radiation) takes advantage of the SE process to build up the light output. The term lasing

is used whenever optical feedback is present. This is often identified by the observation of modes in the output spectra, which result from an optical cavity. The mode spacing $\Delta\lambda$ is related to the cavity length L through the following equation:[81,82]

$$\Delta\lambda = \frac{\lambda_o^{\,2}}{2L(n - \lambda_o dn/d\lambda)}, \tag{3-16}$$

where λ_o is the wavelength of a mode, n is the refractive index at λ_o, and $dn/d\lambda$ is the dispersion of the refractive index. This cavity can be intentional, such as mirror-coated facets or cleaved laser bars, or it can be "accidental," as in the case of cracks in the epilayer or the surfaces of microstructures such as self-formed pyramids.

The experimental setup for the study of SE and lasing is similar to that of PL, since we are looking at the light emitted from a sample that is being excited by a laser. The experimental setup used in this thesis is shown in Figure 25. The laser used in optical pumping, however, must be pulsed rather than cw. The reason for this is that to observe SE, we need to create a population inversion in the sample, *i.e.* there must be more free carriers in the conduction band than in the valence band. Because photoexcited carriers relax back down to the valence band via radiative or nonradiative recombination over a time scale that is typically in the ns or ps range, we must use a pulsed laser to create a population inversion before the carriers have a chance to decay. Additionally, the peak intensity of this laser pulse must be large enough to excite a sufficient number of carriers into the conduction band. Thus, chopping a cw laser beam or using an ultrafast shutter to obtain pulses is not an option.

The excitation density of the pump pulse is typically measured in kW/cm^2. For comparison, a pulsed laser focused to a 1 mm^2 spot with an average power of 5 mW, pulse duration of 10 ns, and a repetition rate of 10 Hz has a peak intensity of 5000 kW/cm^2. Over this same time scale, a cw laser running at 5 mW would only give us 5×10^{-9} W/cm^2 [Ref.64].

For UV excitation, several sources can be use, for example:

1. A XeCl Excimer laser
2. A tunable dye laser pumped by the above-mentioned Excimer laser. The Excimer-pumped dye laser emitted directly in the UV.
3. An injection-seeded Nd:YAG laser, λ = 1064 nm, which could be frequency tripled to give 355 nm or quadrupled to 266 nm using a nonlinear crystal.
4. The 532 nm second-harmonic of this Nd:YAG laser could be used to pump a tunable dye laser. The frequency output can then subsequently frequency doubled into the UV using another nonlinear single harmonic generation crystal. This could yield a wide range of wavelength selection.

Stimulated emission experiments are performed in the edge-emission geometry, pictured in Figure 26. The UV laser excitation source is focused to a line on the sample surface using a cylindrical lens. This forms a gain region that amplifies the SE signal before it is emitted through the edge of the sample. A continuously variable neutral density (ND) filter is used to attenuate the laser power. The resultant emission is collected from the edge of the sample and focused onto the slits of a 1 meter spectrometer

and detected by either a UV-enhanced CCD or an optical multichannel analyzer (OMA), which is a linear diode array, *i.e.* a one-dimensional CCD.

SE in semiconductors is characterized by a threshold, which occurs at the point that the gain in the cavity equals the losses. Below this threshold, we only observe spontaneous emission. Above this threshold, a new peak (or peaks) appears at the maximum of the gain curve. This new peak increases superlinearly in intensity and narrows with increasing excitation intensity as seen in Figure 66.

Optical SE experiments are crucial for research on potential new lasing materials, as well as for the characterization of LDs. Rather than go through the extremely expensive and time-consuming process of fabricating an LD just to test if it works or not (in the research labs and development stage, this can be a colossal undertaking), we can utilize optical pumping experiments. If the LD structure exhibits optically pumped SE/lasing with a reasonable threshold value, creating a successful device lies only in the matter of fabrication (etching, photolithography, contacts, *etc.*). We have cleared the device structure and material quality of any culpability if the LD fails to work properly.

Absorption

Absorption is a straightforward technique that measures the wavelength-dependence of the absorption coefficient of semiconductors. The typical absorption experimental setup is shown in Figure 27 (a). The broadband light from a Xe lamp for

example is sent through a monochromator and scanned across the wavelength range of interest. The resultant monochromatic light is focused onto a spot on the sample, and the light passing through the sample is collected and focused into a PMT connected to a lock-in amplification system. Lock-in is attained by optically chopping the excitation light when it exits the monochromator. The amplifier looks for a signal from the PMT with the same frequency and phase as the chopped beam. This technique greatly reduces the noise signal from stray light entering the PMT. By scanning the excitation light across the band gap region of the sample, we obtain an absorption spectrum. Absorption of light in a semiconductor is governed by Beer's Law:

$$I = I_o e^{-\alpha d}, \qquad (11)$$

where I is the output intensity (the scan we just obtained), I_o is the incident intensity (obtained by scanning the lamp with no sample present), α is the absorption coefficient, and d is the sample thickness. When calculating absolute absorption values, the reflection of the incident light from the sample surface must be taken into account. Optical density (OD), is a unit less parameter, is often used when the thickness of the sample is unknown. OD is given by:

$$\mathrm{OD} = \alpha d = -\ln\left(\frac{I}{I_o}\right) \qquad (12)$$

which is just the absorption coefficient times the thickness.

The thickness of the sample is very important in absorption measurements, not only because it is necessary for the correct calculation of α, but also because it can determine whether or not any photons can be observed. If the sample is too thick, so

many of the incident photons above the bandgap of the semiconductor are absorbed that the instruments cannot measure the small number that does make it through.

Photoabsorption (Pump-Probe Experiment)

The pump-probe technique is a frequently used method for extracting information about optical phenomena associated with high carrier concentrations, such as stimulated emission, gain. In pump-probe experiments, the sample is first excited with an intense and spectrally narrow laser beam. The changes in absorption or transmission are then probed with a weak and spectrally wide beam. An alternative technique uses a weak and spectrally narrow probe beam which is scanned in the frequency range of the pump beam. Usually, two spectra are required to extract information from pump-probe experiments. The first spectrum is taken in the presence of the pump beam while the second spectrum is taken without the pump. The difference between the two spectra gives information about the changes caused by the pump beam. There are two requirements for the intensity of the probe beam:

(1) It should be low enough so it does not introduce any changes to the optical properties of the sample.

(2) It should be high enough to give a good signal-to-noise ratio. As a rule of thumb, the intensity of the probe beam should be five times stronger than the luminescence arising from the pump.

The pump-probe technique can be used in both the continuous wave and pulsed regimes. However it is crucially important to satisfy the following conditions, which minimize lateral and longitudinal diffusion of the excited species:

(1) The probe beam should be temporally narrower than the pump. It should begin after the pump pulse starts and end before the pump pulse ends.

(2) The probe beam should be spatially smaller than the pump and it should probe only the central part of the pump.

In the case of pulsed pump-probe experiments, the pump pulse repetition rate should be low enough not to considerably increase the lattice temperature of the sample. One of the most difficult aspects of pump-probe experiments is the inhomogeneity of the excitation beam. The basic experimental setup for the pump-probe technique is shown in Figure 27 (b).

It was observed that AlGaN samples used in pump-probe experiments have additional limitations with regard to the sample thickness. In particular, if the sample is too thick, excitonic features can not be observed due to the limited signal-to-noise ratio of our instrumentation. However, if the sample is too thin, excitonic features are absent due to the inferior quality of the AlGaN epilayer close to the interface[58].

For more detail in describing the pump-probe technique we refer to suggestions given by Klingshirn *et. al.*,[83] Yamada *et. al.*,[84] Bohnert *et. al.*[85] and Bidynk[58].

Reflectance

Reflectance measurements are performed using a setup nearly identical to the one shown above for absorption. The only difference lies in the position of the sample and the detector, as can be seen in Figure 1 (c) For reflectance, the sample is tilted slightly in the plane of the optical table and the detector is rotated at an appropriate angle to measure the signal reflected from the sample surface. The reflectance spectrum is scanned across the band gap of the sample to yield information about the band gaps and excitonic features in semiconductors.

Photoreflectance

The basic photoreflectance (PR) setup is pictured in Figure 27 (d). The only change from reflectance is the addition of a weak modulating laser beam. The difference between conventional reflectance and PR is that the latter is a differential method utilizing a modulation of the built-in electric field through photoinjected carriers by a periodically modulated light beam, such as a chopped HeCd laser beam. The change in reflectivity, $\Delta R/R$, due to the modulation may be expressed as:

$$\frac{\Delta R}{R} = a\Delta\varepsilon_1 + b\Delta\varepsilon_2, \qquad (13)$$

where *a* and *b* are referred to as Seraphin coefficients and are related to the unperturbed dielectric function $\varepsilon = \varepsilon_1 + i\varepsilon_2$, while $\Delta\varepsilon_1$ and $\Delta\varepsilon_2$ are the changes in the real and the imaginary parts of the modulated dielectric function, respectively.[86] The differential changes in the reflectivity appear as sharp derivative-like line shape in the modulated reflectance spectrum, corresponding to specific transitions in the Brillouin zone.

Several additional experimental steps must be taken for PR measurements:

1. The chopper is moved from the lamp light to the laser light. The lock-in amplifier automatically measures the difference in the reflectance with and without modulation, simplifying the measurement (we don't have to take a reflectance scan with the laser, take a reflectance scan without the laser, then take the difference).
2. The laser power must be made low so as not to excite too much PL from the sample. There is no spectrometer between the sample and the PMT, so the entire spectrum of the PL signal contributes to a background level for PR. A balance between this PL background and the modulation field strength must be found.
3. A bandpass filter must be used to block the scattered laser light, which would saturate the PMT, but must still allow significant transmittance in the bandgap region.
4. Care must be taken to overlap the lamp and laser spots on the sample surface.

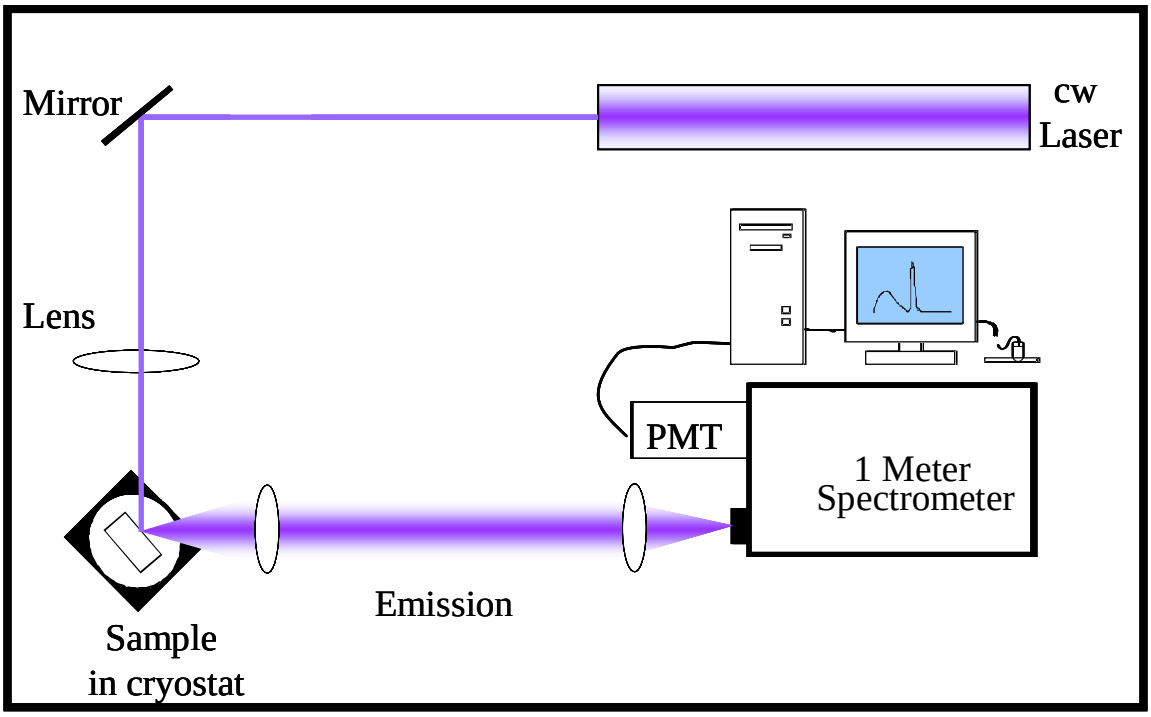

Figure 21. Photoluminescence measurement setup.

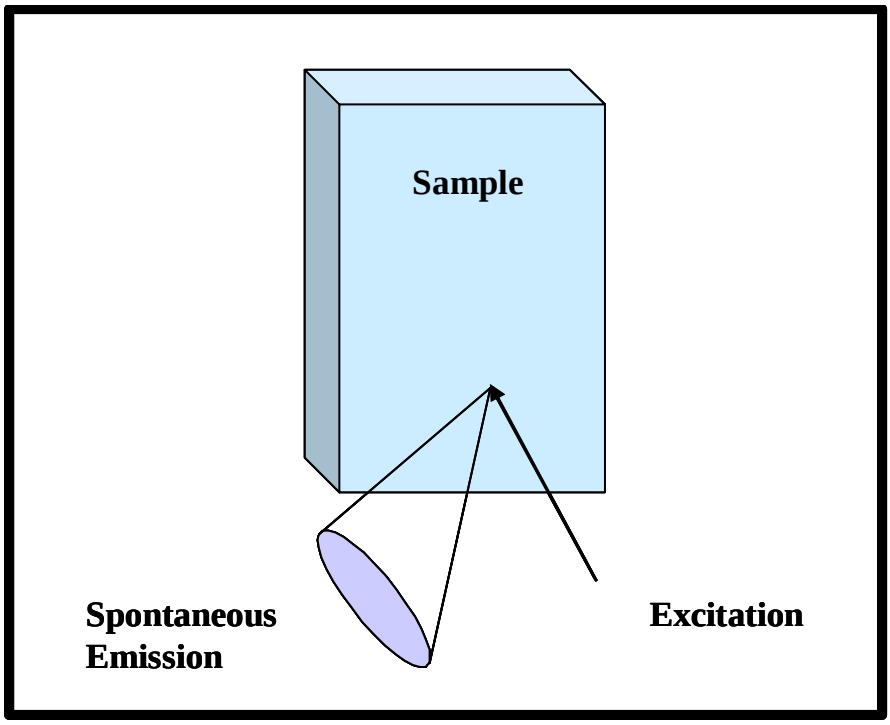

Figure 22. Schematic diagram of surface emission geometry.

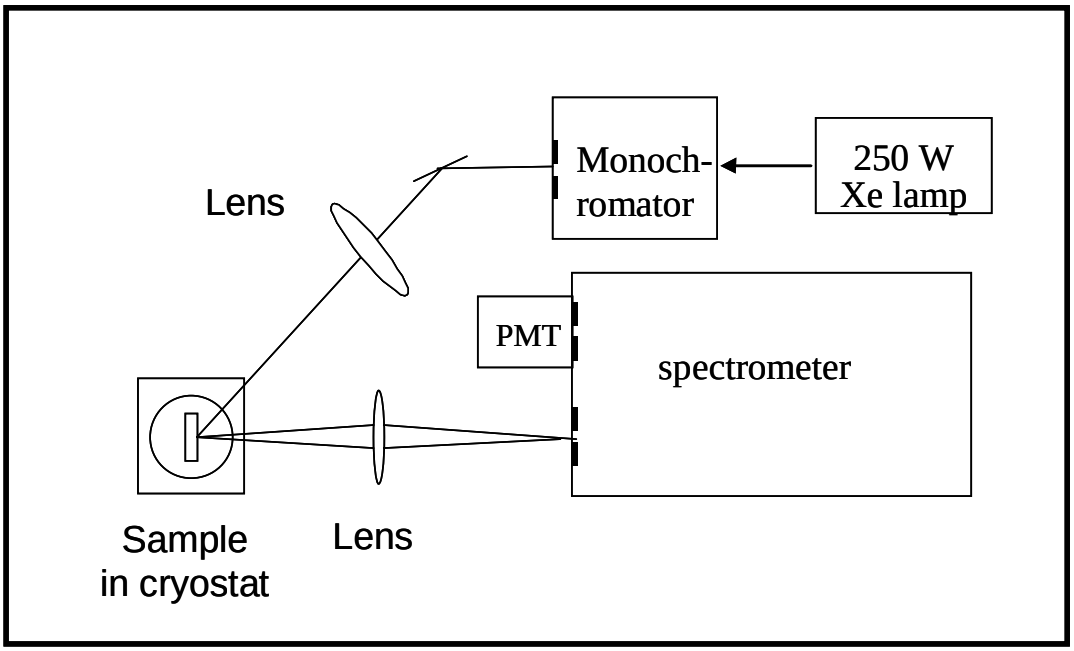

Figure 23. Typical PLE experimental setup. [Adopted from ref. 64]

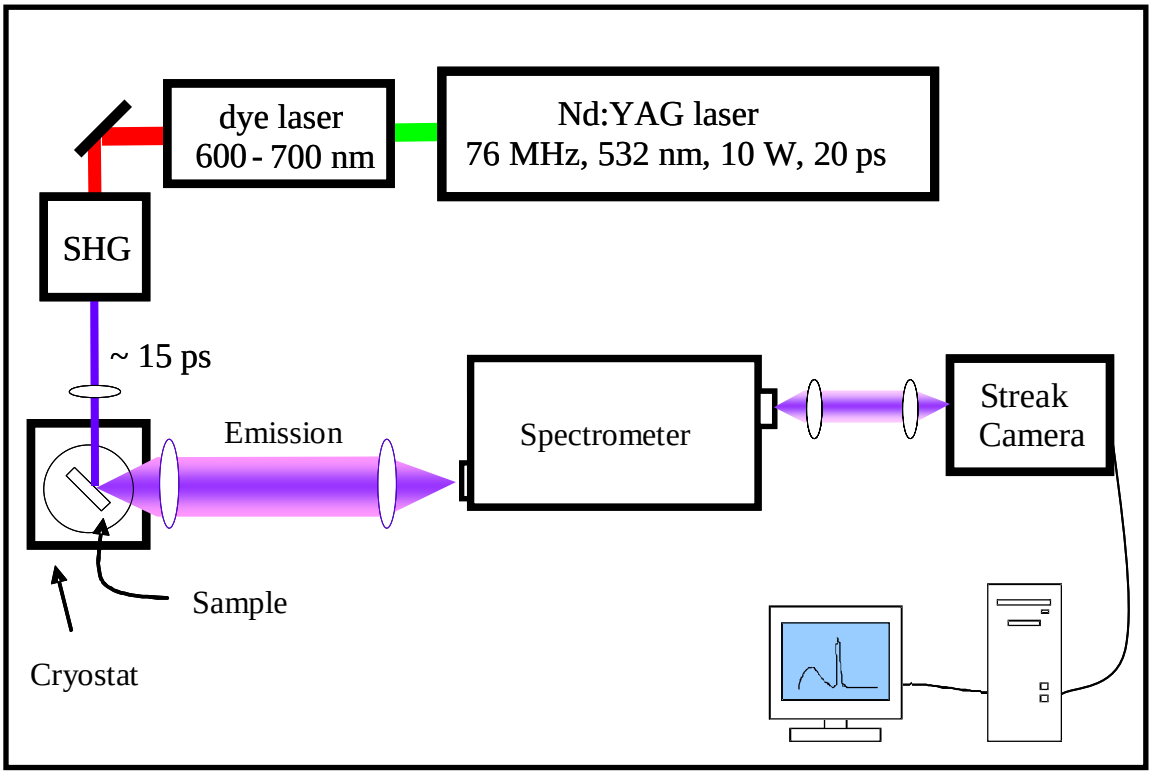

Figure 24. Time-resolved PL experimental setup. The sample is mounted in a Helium variable-temperature, angle-adjustable cryostat cooled by a closed-cycle helium refrigerator.

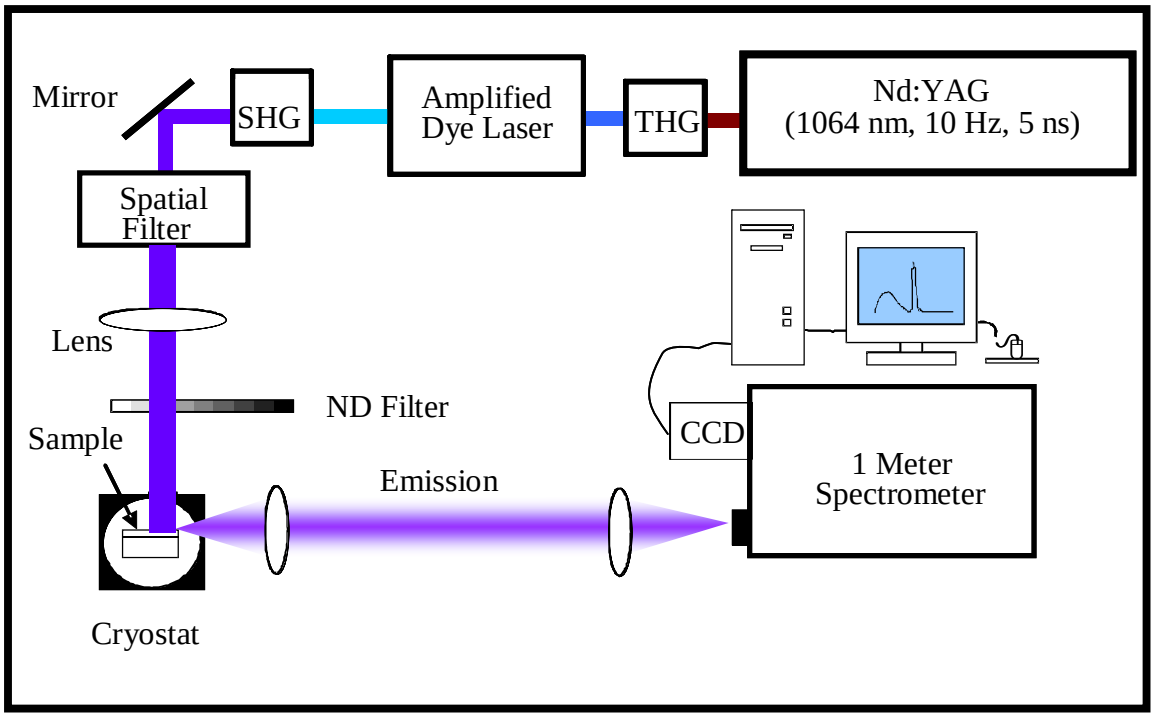

Figure 25. Stimulated emission experiment setup. The sample is mounted in a Helium variable-temperature, angle-adjustable cryostat cooled by a closed-cycle helium refrigerator. The sample excited by the pulsed laser beam focused by a cylindrical lens.

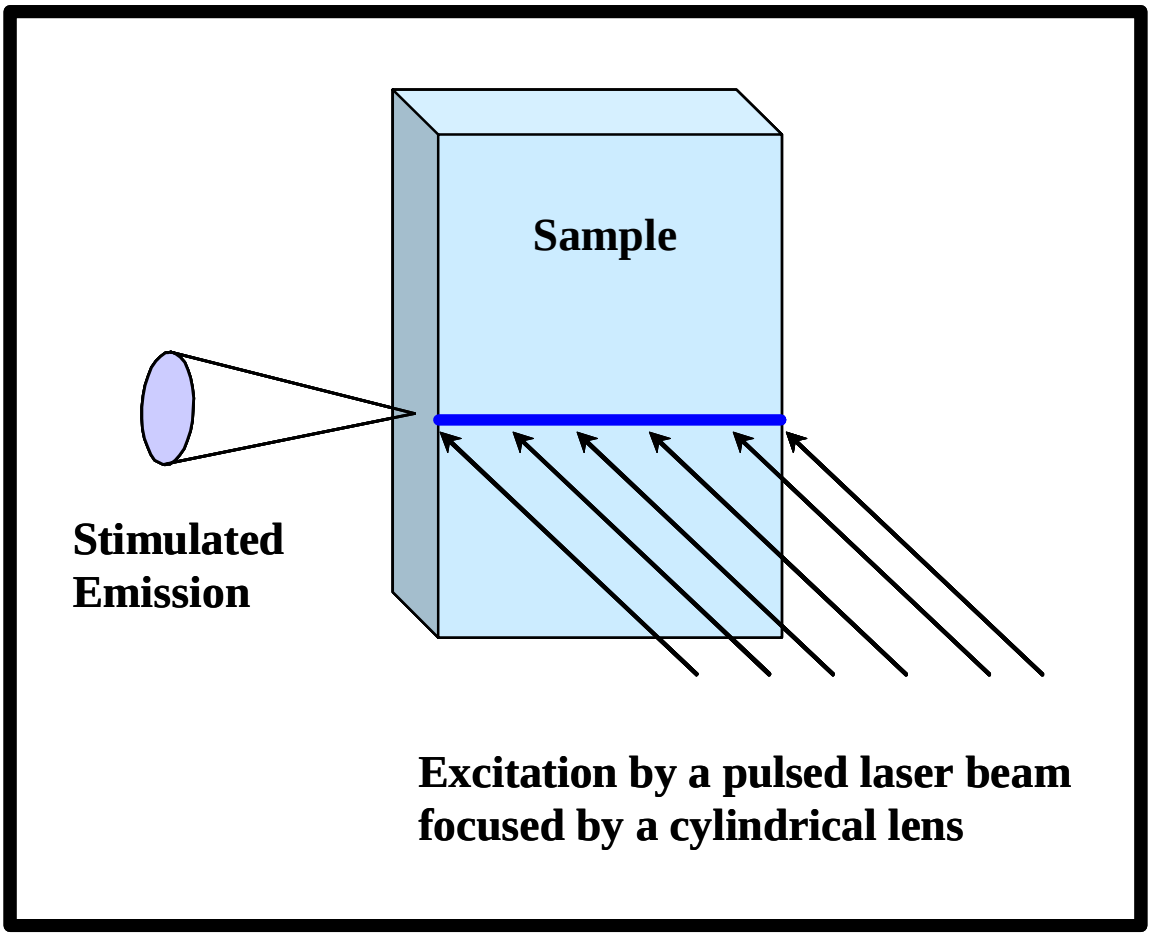

Figure 26. Schematic edge emission geometry used for the stimulated emission measurements.

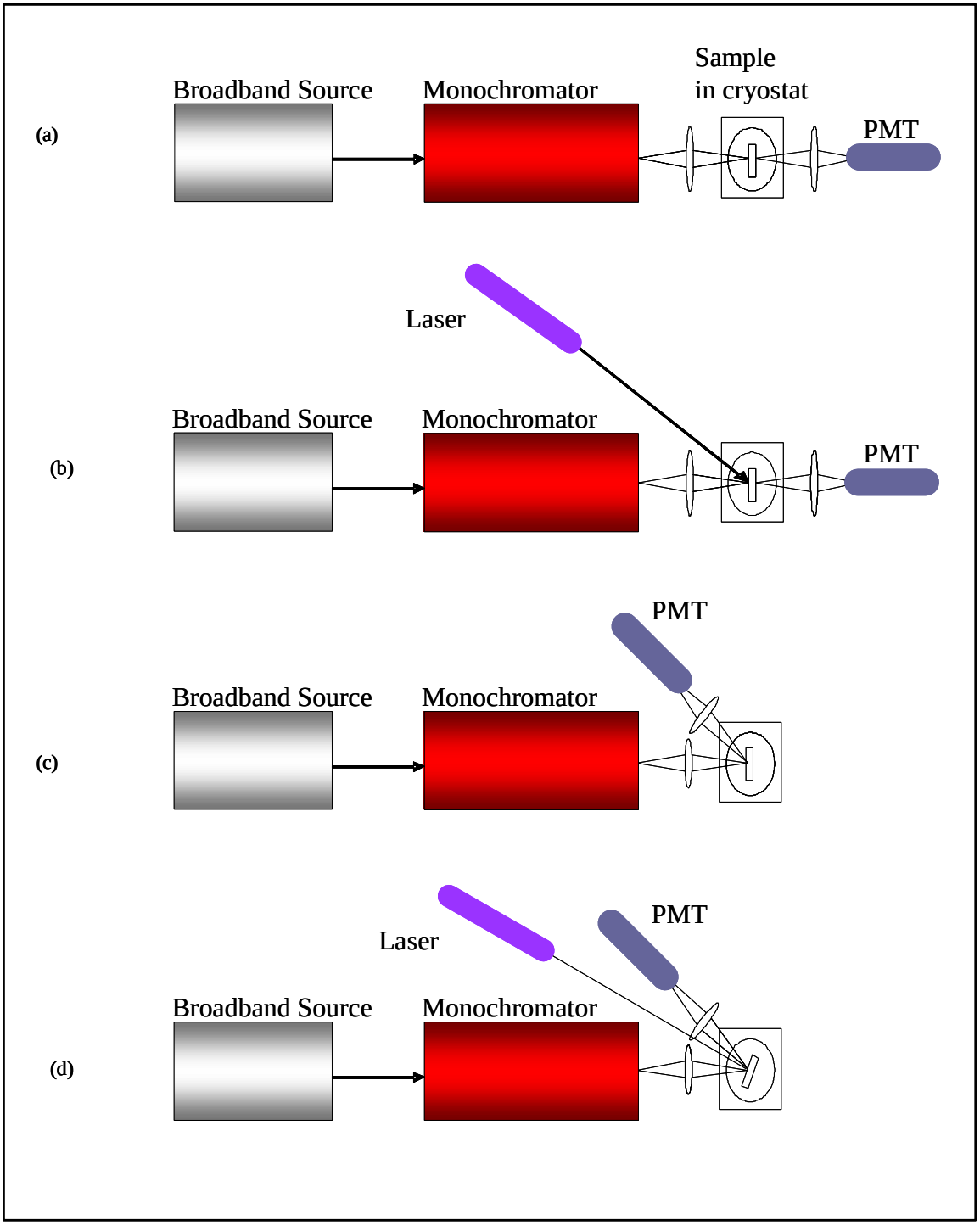

Figure 27. Basic experimental setups for the measurement of (a) absorption, (b) photoabsorption (c) reflectance, and (d) photoreflectance.

Chapter VI

Influence of Compressive Strain Induced by Sapphire Substrate On GaN Energy Gap Investigated by Laser lift-off

Introduction

The importance of the effects of the strain in the GaN epilayers due to the mismatch of the lattice parameters and coefficient of thermal expansion between GaN and the substrate materials has been realized [Bernard[59]]. Table 1 shows selected physical properties of the III-V nitrides, sapphire and SiC.

It is difficult to separate the effects of strain caused by lattice parameter mismatch from ones involving thermal-expansion mismatch to exactly determine their influence on the optical properties of GaN epilayers. However, the overall effect of strain generated in GaN on sapphire is compressive, which results in an increased band-gap (blue shift).

The lattice mismatch between GaN and sapphire substrate leads to high density of extended defects, such as dislocations [Lester et. al.[25] and Akasaki et. al.[87]]. High density of dislocations in GaN causes deterioration in the operation of optoelectronic devices mainly by [Porowski et. al.[31]]:

1. Serving as nonradiative recombination centers for electrons and holes leading to heat generation instead of optical emission.
2. Disturbing the epitaxial growth, therefore perfect flat structures are difficult to obtain.

In this work, we studied the influence of the compressive strain induced by sapphire substrate on GaN energy gap by means of laser lift-off for the substrate.

Experimental details

Four GaN epilayers grown on sapphire substrate by HVPE methods were prepared to examine the influence of the compressive strain induced by sapphire substrate on GaN energy gap by means of laser lift-off. The thicknesses of these samples have been measured using scanning electron microscope as 18 μm, 33 μm, 45 μm, 74 μm for samples numbered I, II, III, and IV respectively. The backside of the sapphire substrate was polished.

Temperature dependent photoluminescence (PL) experiments were performed using the 325 nm cw HeCd laser. The sample was mounted in a variable-temperature cryostat cooled by a closed-cycle helium refrigerator, and the PL spectra were recorded with a photomultiplier tube in conjunction with a 1 m high-resolution spectrometer.

Figure 21 shows the photoluminescence measurement setup and Figure 22 shows schematic diagram of surface emission geometry.

GaN decomposition performed using the laser lift-off (LLO) technique. 248 nm 20 ns KrF Lambda Physik Excimer laser pulse beam energy was utilized. The beam was defocused with a fused silica convex lens with a focal length of 30 mm through the polished sapphire face as in seen in Figure 28. A sapphire wafer was bonded to the surface of the GaN thin film using two parts "Durabond 950 FS" metallic adhesive mix from "Cotronics" which also has been tested to show slow reaction with HCl etching. The following bonding system has formed: "Sapphire substrate/GaN/adhesive/sapphire wafer" as seen in Figure 29.

The structure was placed on a motorized horizontal rail stage and the beam spread on sapphire side to insure homogenous distribution for the beam. The 248 nm 20 ns KrF Lambda Physik Pulsed Excimer laser beam energy was altered from about 200 mJ to 500 mJ respectively. After a successful lift-off, a thin Ga layer on the surface of the exposed interface was removed by etching process using a 1:1 solution of hydrochloric acid (HCl) and de-ionized water. The interfacial decomposed layer is expected to be very thin if compared to the film thickness. We estimated this layer to be in the range of the absorption penetration depth for the 248 nm incident beam that is less than 75 nm, in agreement with Wong et. al.[38]. The surface then cleaned by acetone and methanol. The lift- off quality has been examined using the PL technique.

Data and analysis

The temperature dependent PL showed that the free excitons dominated the spectrum, even at low temperatures as seen in Figure 30 to Figure 33. The intensity of the bound excitons decreases with increasing temperature due to thermal dissociation and becomes irresolvable for temperatures exceeding 60 K. As temperatures exceed 200 K, excitons broaden and eventually band-to-band recombination of free carriers dominates the photoluminescence spectra. The domination of the free exciton even at low temperature and the disappearance of the bound exciton at very low temperature, 60 K, indicated the low density of defects in the epilayers grown by HVPE technique. This is indication of low dislocation density. It is believed that the material quality associated with the HVPE process is actually higher than that of MOCVD and the deposition rate is 100 times faster that of MOCVD[88].

The shape of the two peaks 1LO and 2LO and the equal separation FX-1LO and 1LO-2LO, average 92 meV, indicate that these to peaks are longitudinal optical phonons replicas [Bernard[59]].

Characterization of the bonded GaN to sapphire wafer was performed using photoluminescence at temperature 10 K. Figure 34 to Figure 37 show comparison between the PL at 10 K for the samples before and after the lift-off. These data summarized in Figure 38 which shows the PL peak energy position for GaN before and

after the lift-off as a function in the original samples thickness. The PL emission from samples on sapphire has higher energy, indicating the presence of a compressive strain [Perlin et. al.[62] and Bernard[59]]. This residual strain is related to the difference between the thermal expansion coefficients of GaN ($5.059 \times 10^{-6} K^{-1}$) and that of sapphire ($7.5 \times 10^{-6} K^{-1}$) [Perlin et. al.[62]], which causes a biaxial strain to develop during the sample cool down process from the growth temperature.

For the four samples the peak energy red-shifted as the thickness of the epilayer increased in before or after the lift-off. This indication that the less the thickness the higher the density of the threading dislocation, and the higher the density of the nonradiative recombination centers. This is also, in agreement with Warren et. al.[89] conclusion "dislocations originate at the substrate interface, and the dislocations density decreases substantially with increasing film thickness away from the interface". Accordingly, the red shift of the peaks of the four samples after the lift-off indicates that the dislocation density decreased substantially with the separation of the substrate by the laser lift-off technique. In addition, the decrease in the rate of this red shift with increasing the thickness after the lift-off in comparison to that rate for the samples on sapphire is an indication that the lift-off is a powerful tool to enhance the performance of GaN based devices. Though this technology is sophisticated and expensive, it enables the use of GaN as substrates after reducing its dislocation density from 10^8 cm^{-2} before the lift-off to 10^6 cm^{-2} after the lift-off[36,90,91].

Figure 34 to Figure 37 indicate high quality lift-off as shown by comparison between of the peak full-width at half maximum of each sample before and after the lift-off. The FWHM showed little change in general after the lift- off as summarized in Figure 39, which indicated that the quality of the films did not alter by the separation of the substrate [Wong et. al.[38]].

Conclusion

Gallium nitride epilayers grown on sapphire by hydride vapor-phase epitaxy (HVPE) technique showed high optical quality by means of photoluminescence (PL) technique. The epilayers were successfully separated from the sapphire substrate using 248 nm 20 ns excimer laser. The sapphire substrate absorbed the laser radiation. This induced rabid thermal decomposition of the interfacial layer yielding Ga (metallic) and N_2 (gas). The epilayers were then bonded to sapphire wafers. The comparison between the peak full width at half maxima FWHM of the PL peaks of the GaN epilayers before and after the lift-off demonstrated that the structural quality of the GaN films was not altered by the separation and transfer process. We have shown that GaN/sapphire misfit generated strain. The thermal coefficients mismatch generated compressive strain, which results in an increase in the band gap (blue shift), and the lattice mismatch created dislocation lines. These dislocation lines produce nonradiative recombination centers. The presence of dislocations can be detrimental to the efficiency of optoelectronic devices. The red-shift of the peaks of the four samples after the lift- off indicates that the dislocation density decreased substantially with the separation of the substrate.

Table 2: Selected physical properties of the group III-V nitrides, sapphire and SiC. [Adopted from Ref. 92.]

Material	Lattice Parameter (nm)	Thermal Conductivity (W/cm K)	Thermal Expansion Coefficient (10^6/K)	Band Gap (eV)
w-GaN	a=0.3189 c=0.5185	1.3	a=5.59 c=3.17	3.39
w-AlN	a=0.3112 c=0.4982	2.0	a=4.2 c=5.3	6.2
w-In	a=0.3548 c=0.5760	4.9	a=4.2 c=5.3	1.89
SiC	a=0.308 c=1.512	4.9	a=4.2 c=4.68	2.996
Sapphire	a=0.4758 c=1.299	0.5	a=7.5 c=8.5	6.2

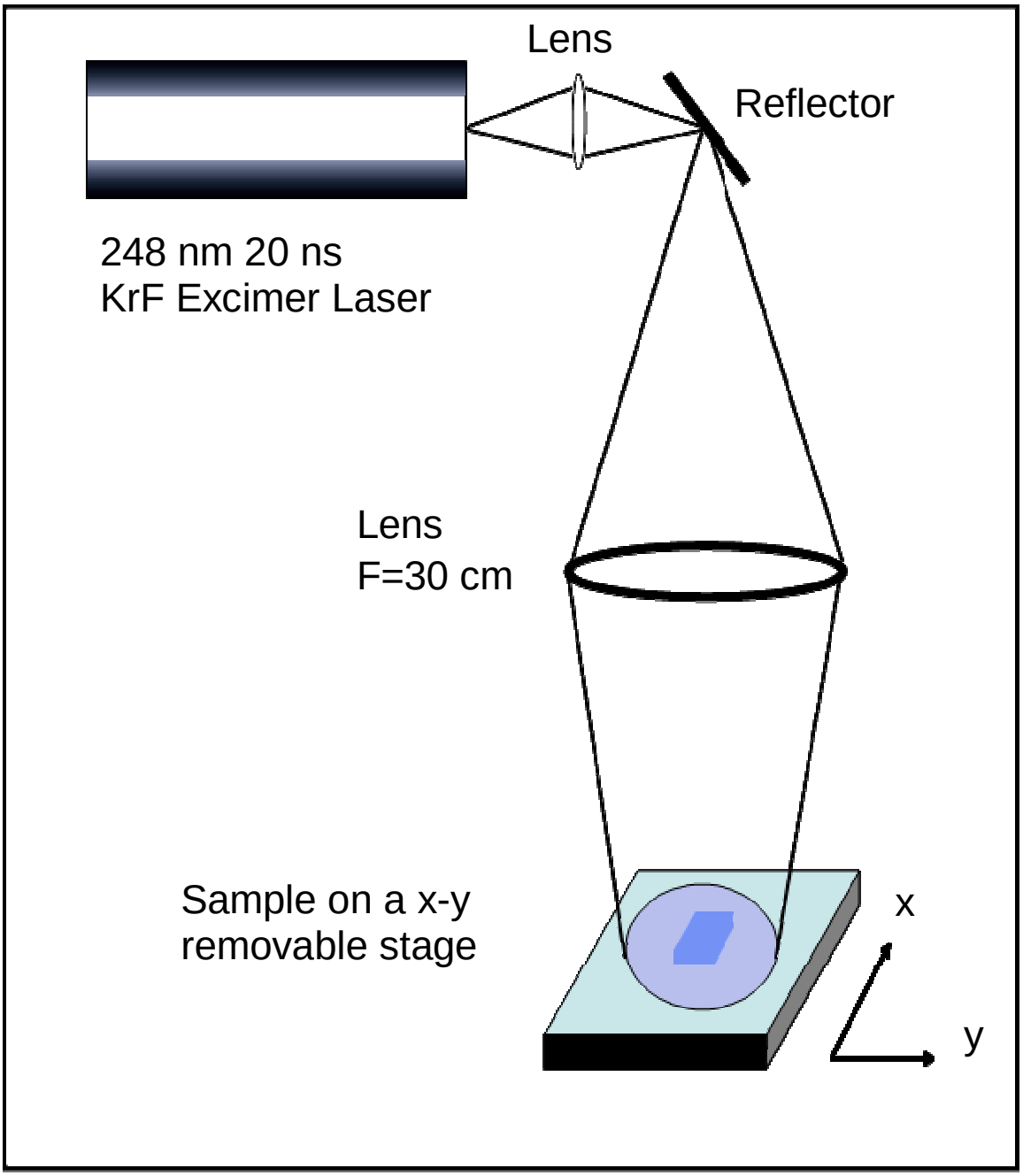

Figure 28. Schematic for the lift-off by the KrF pulsed Excimer laser system. The sample was placed on a motorized horizontal rail stage with a capability to move in x- or y-directions.

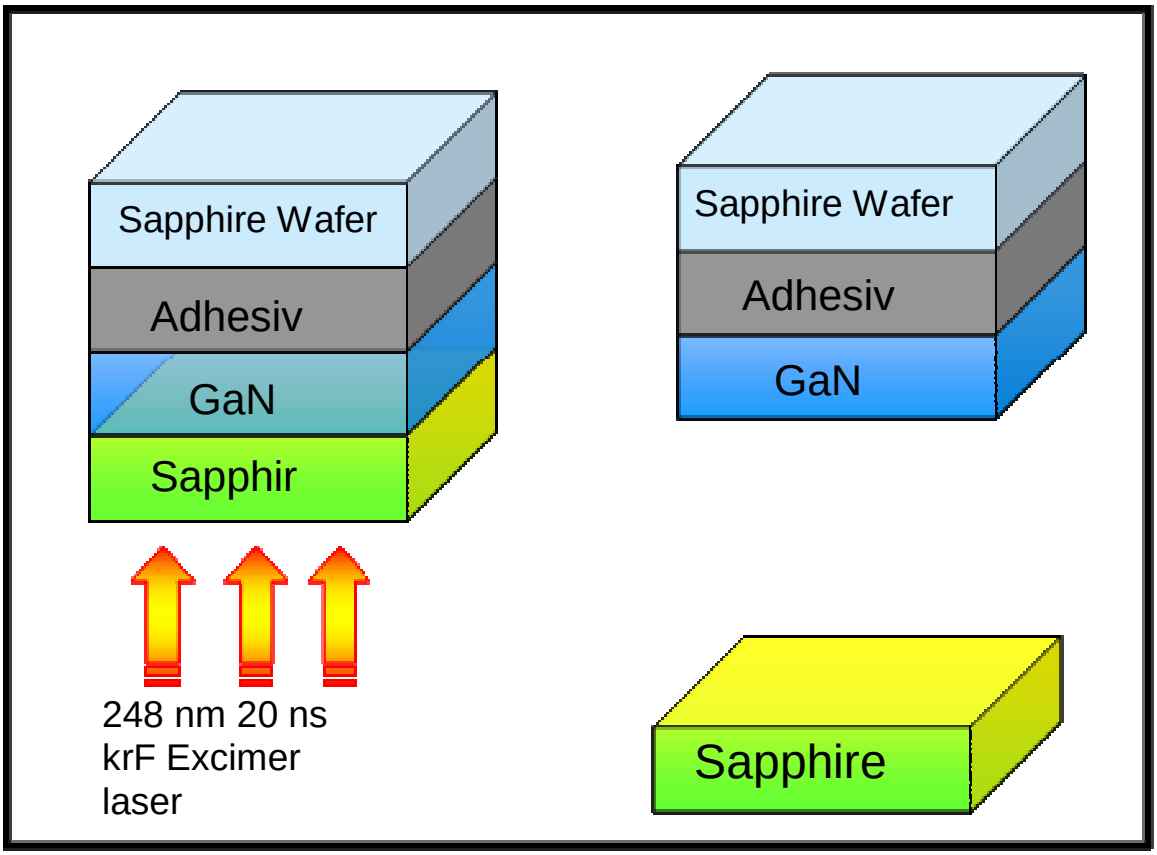

Figure 29. Laser lift-off for sapphire substrate.

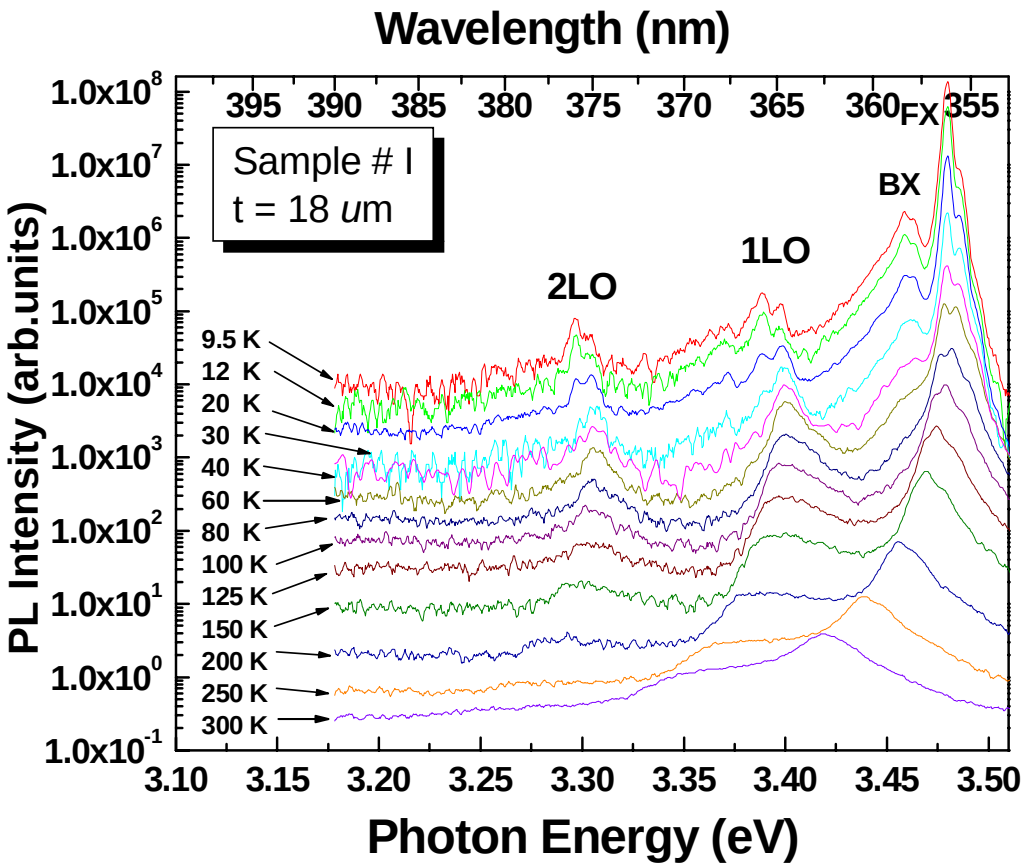

Figure 30. Temperature dependent PL for GaN epilayer (sample # I) grown on sapphire by HVPE technique. The thickness of the epilayer is 18 μm. The free exciton FX dominates the spectra at low temperatures. At temperature exceeding 60 K, the bound exciton BX becomes irresolvable. The two peaks to the left 1LO and 2LO are longitudinal optical (LO) phonons replica.

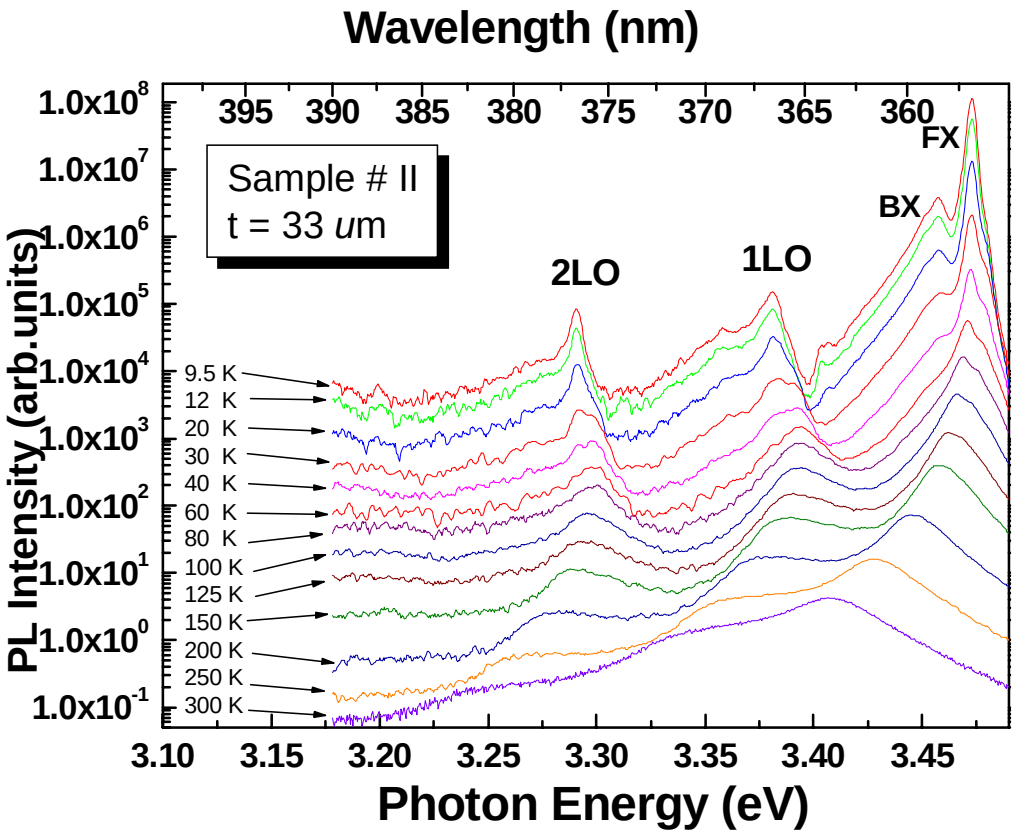

Figure 31. Temperature dependent PL for GaN epilayer (sample # II) grown on sapphire by HVPE technique. The thickness of the epilayer is 33 μm. The free exciton FX dominates the spectra at low temperatures. At temperature exceeding 60 K, the bound exciton BX becomes irresolvable. The two peaks to the left 1LO and 2LO are longitudinal optical (LO) phonons replica.

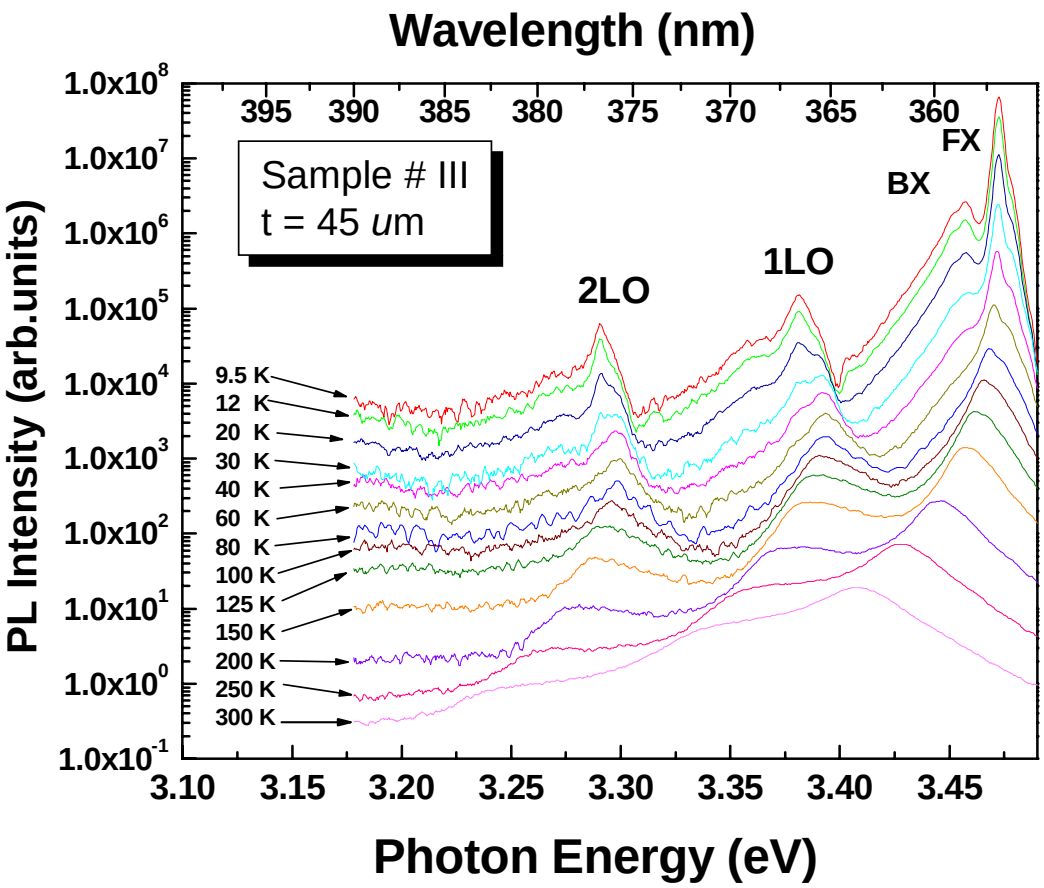

Figure 32. Temperature dependent PL for GaN epilayer (sample # III) grown on sapphire by HVPE technique. The thickness of the epilayer is 45 μm. The free exciton FX dominates the spectra at low temperatures. At temperature exceeding 60 K, the bound exciton BX becomes irresolvable. The two peaks to the left 1LO and 2LO are longitudinal optical (LO) phonons replica.

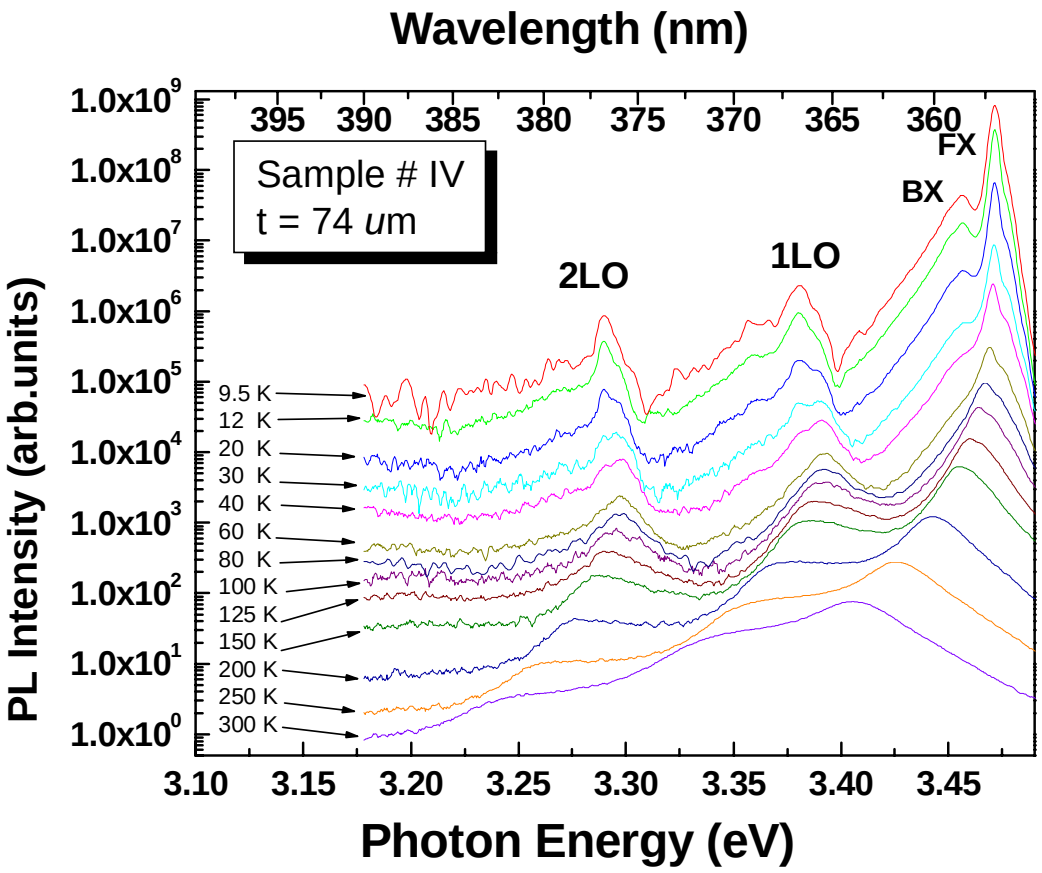

Figure 33. Temperature dependent PL for GaN epilayer (sample # IV) grown on sapphire by HVPE technique. The thickness of the epilayer is 74 μm. The free exciton FX dominates the spectra at low temperatures. At temperature exceeding 60 K, the bound exciton BX becomes irresolvable. The two peaks to the left 1LO and 2LO are longitudinal optical (LO) phonons replica.

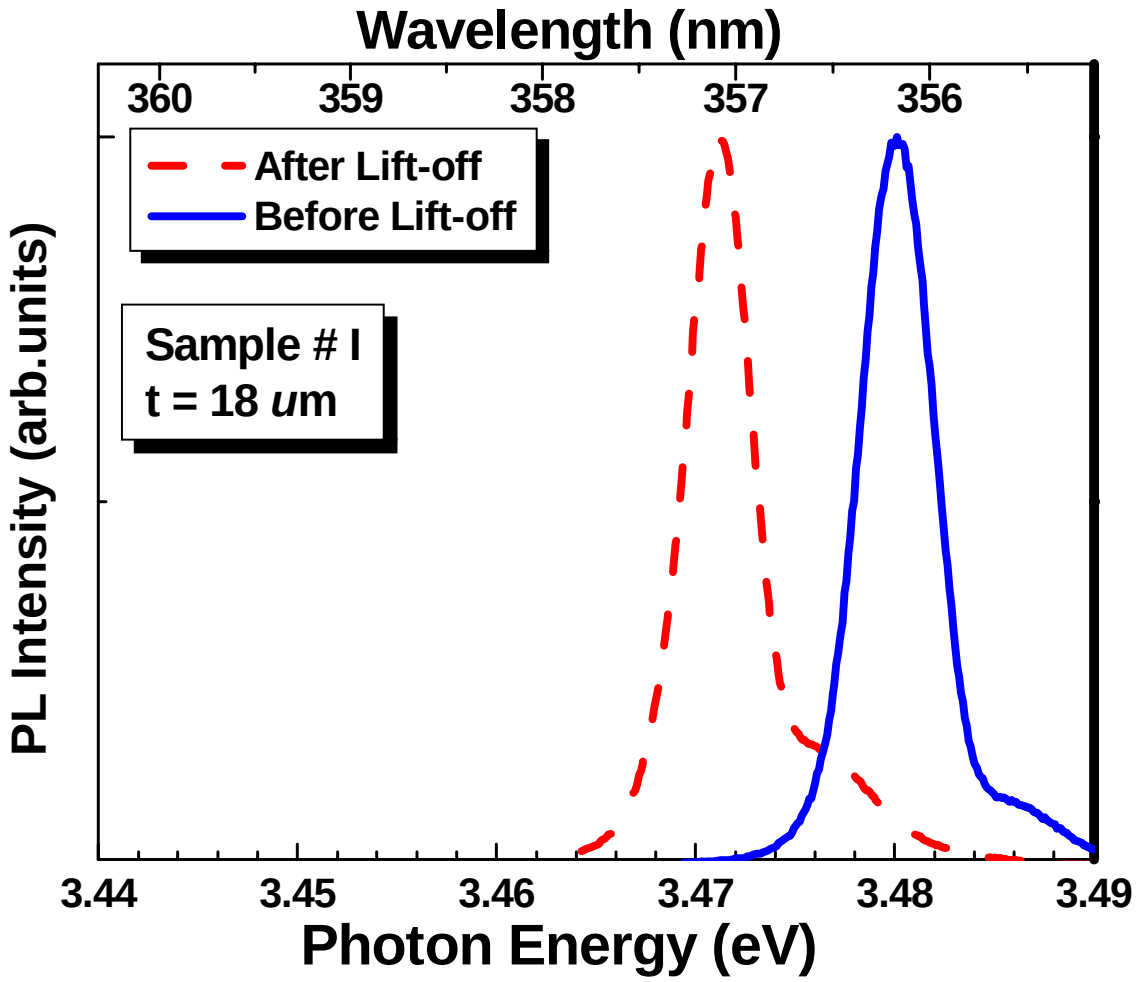

Figure 34. PL for GaN epilayer (sample # I) grown on sapphire by HVPE technique before and after the lift-off at temperature 10 K. The thickness of the epilayer is 18 µm. The shape and the full width at half-maxima FWHM of the free exciton indicate high quality damage free separation of GaN thin film.

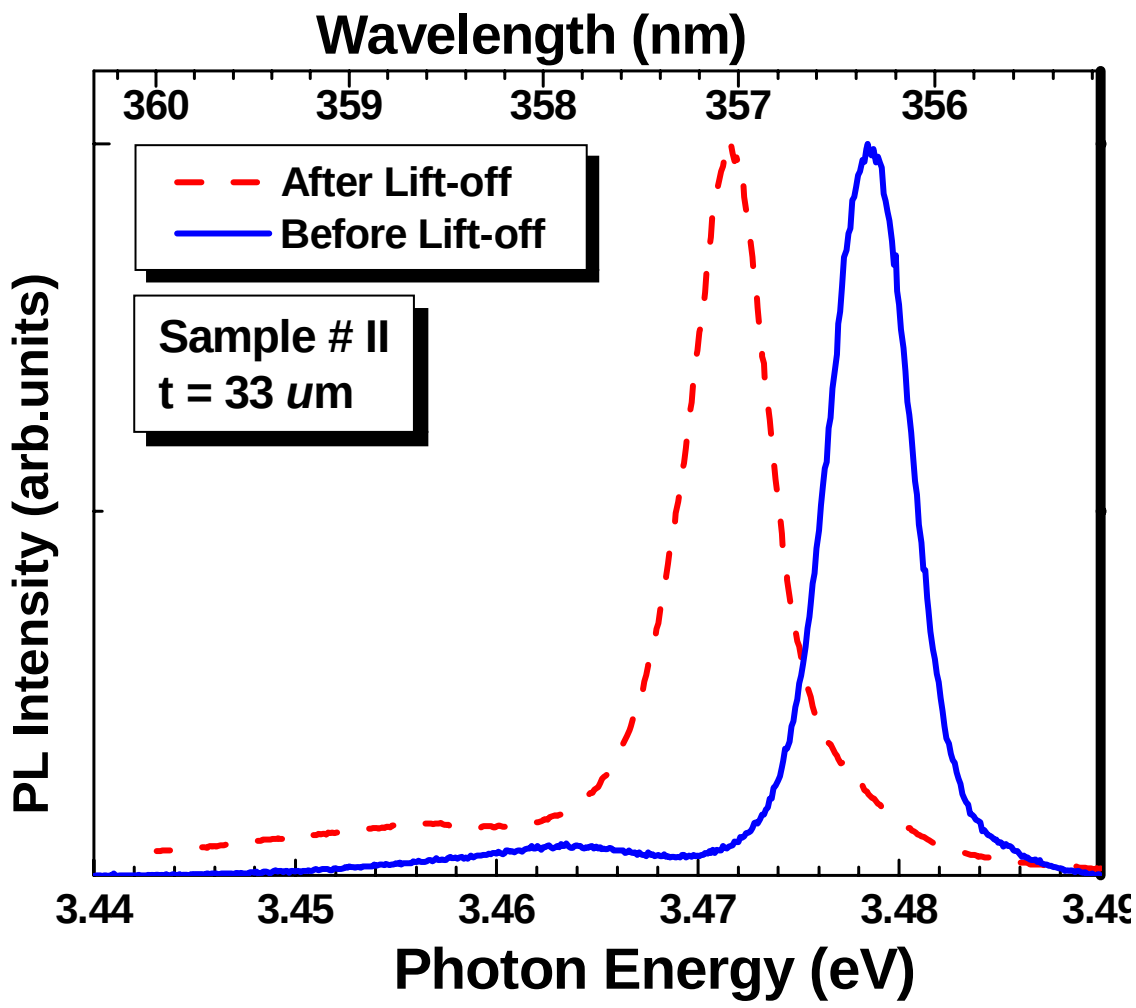

Figure 35. PL for GaN epilayer (sample # II) grown on sapphire by HVPE technique before and after the lift-off at temperature 10 K. The thickness of the epilayer is 33 µm. The shape and the full width at half- maxima FWHM of the free exciton indicate high quality damage free separation of GaN thin film.

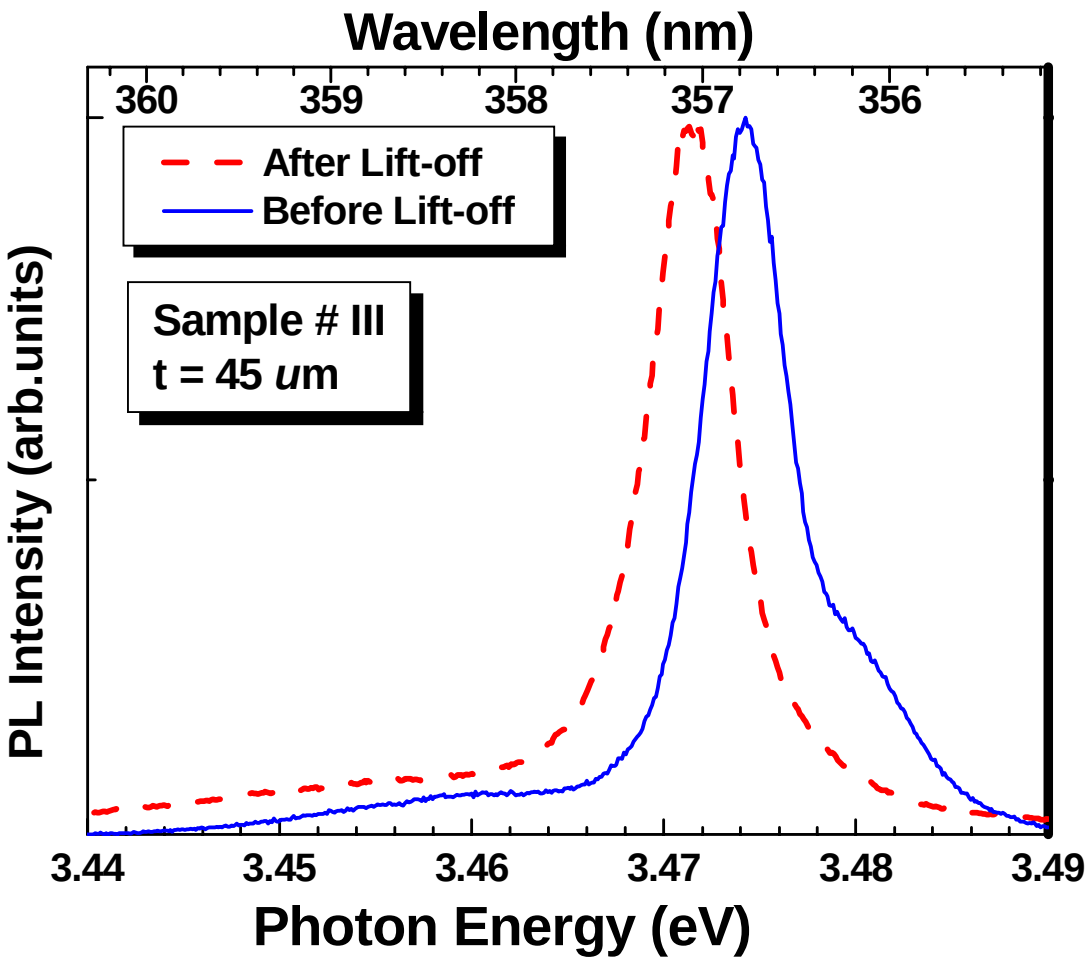

Figure 36. PL for GaN epilayer (sample # III) grown on sapphire by HVPE technique before and after the lift-off at temperature 10 K. The thickness of the epilayer is 45 µm. The shape and the full width at half- maxima FWHM of the free exciton indicate high quality damage free separation of GaN thin film.

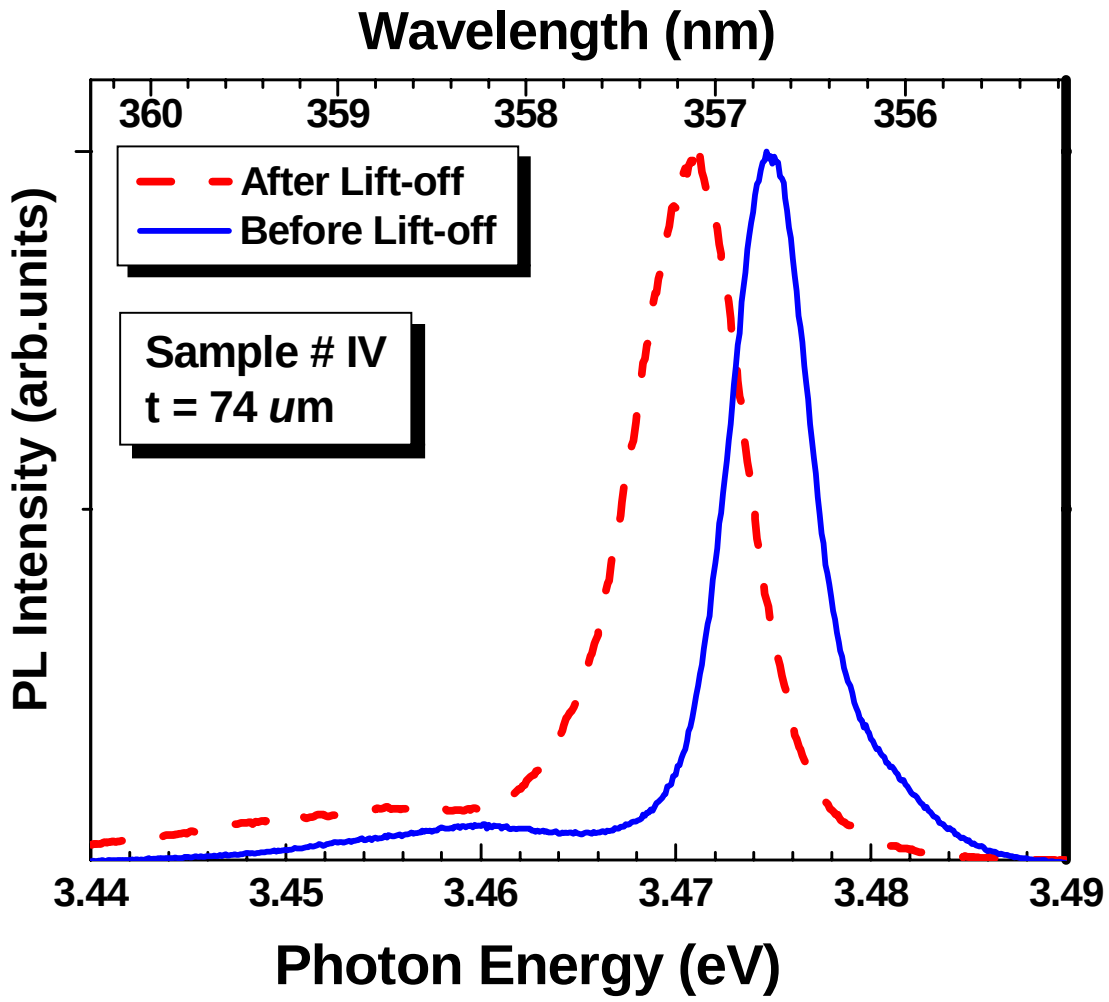

Figure 37. PL for GaN epilayer (sample # IV) grown on sapphire by HVPE technique before and after the lift-off at temperature 10 K. The thickness of the epilayer is 74 µm. The shape and the full width at half- maxima FWHM of the free exciton indicate high quality damage free separation of GaN thin film.

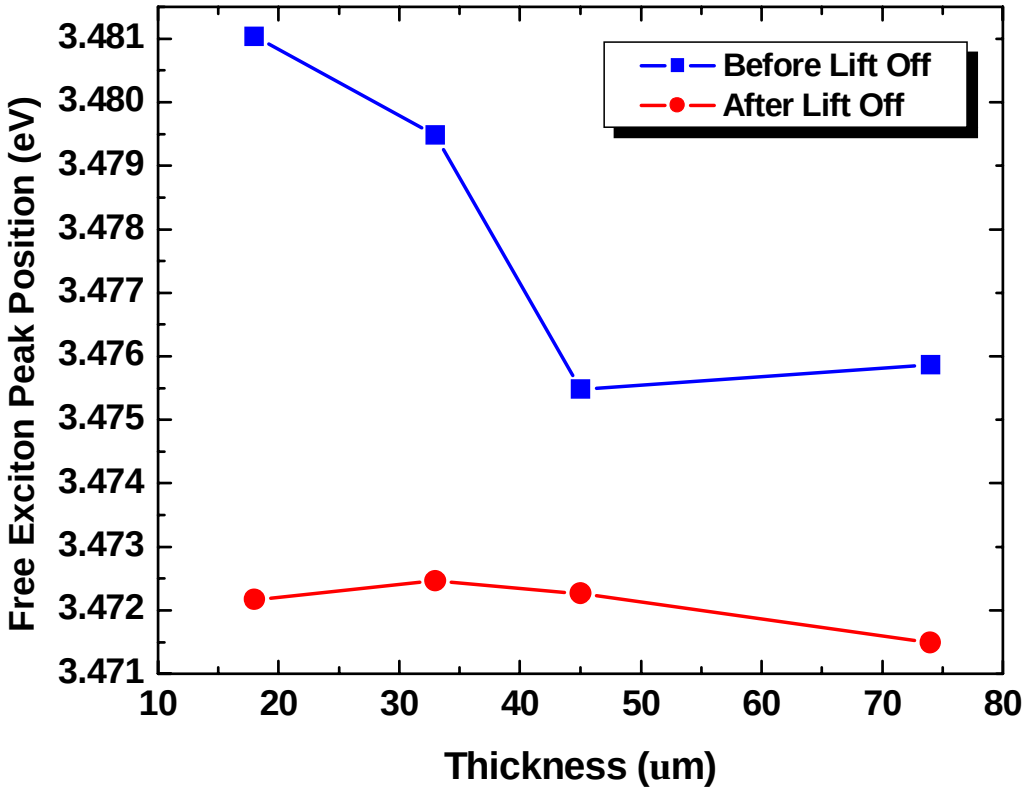

Figure 38. PL peak energy position for GaN before and after the lift-off as a function of the original samples thickness.

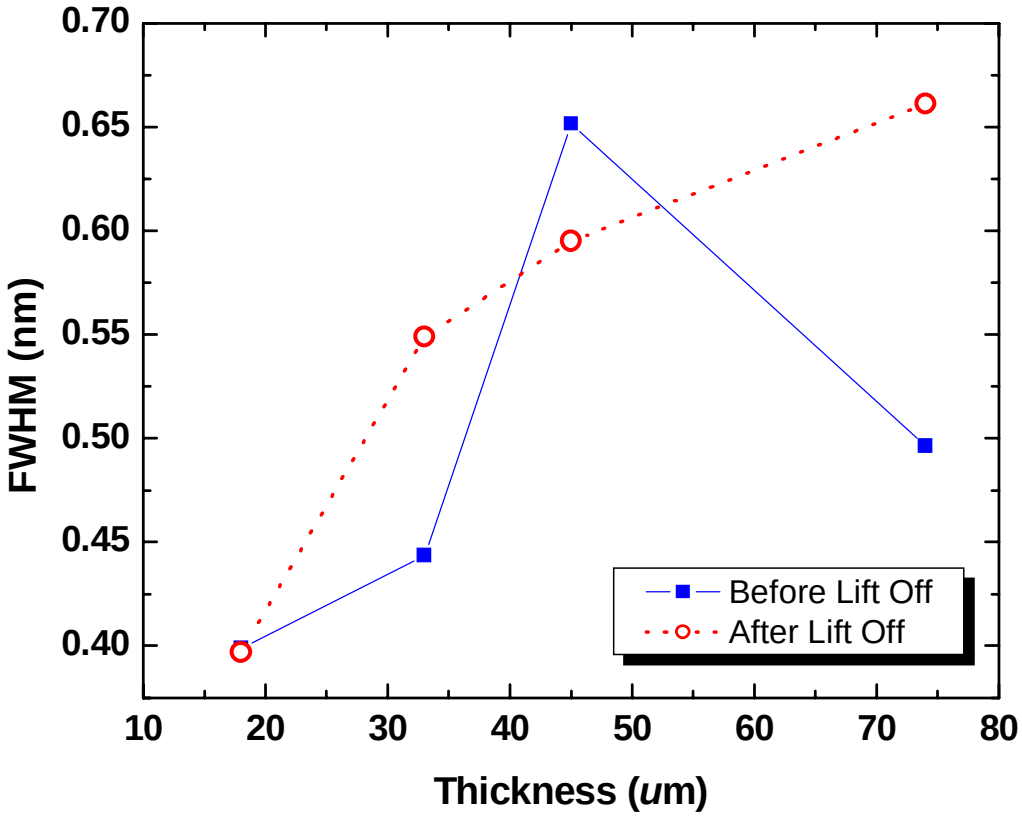

Figure 39. The FWHM for the free exciton versus the thickness of the samples before and after the lift-off. There is no significant change in the FWHM in general. The plot indicates fairly that the samples in general had not suffered thermal or mechanical damage during the separation.

Chapter VII

Investigation of Strain-Induced-Effects on the Optical Properties of $GaN/Al_xGa_{1-x}N$ Heterostructure by Means of Laser Lift-Off

Introduction

Typical exciton (free/bound) temperature dependent PL for GaN showed that as the temperature increased exciton peak energy decreased "red-shifted" as seen

Figure **11**. For AlGaN materials the "S-shaped" PL peak energy shift (decrease-increase-decrease) has been reported by many authors (e.g. J. J. Song and Cho[93]) as seen in Figure 42. They attributed this anomalous behavior to alloy non-homogeneities in the AlGaN epilayers with large Al contents.

We observed the "S-shaped" PL peak energy shift for 4-$GaN/Al_xGa_{1-x}N$ heterostructure described in Table 3 and Table **4**. In addition, we observed anomalous photoquenching in the PL intensity. We believe these abnormal behaviors are results of strain induced because of the difference in the lattice parameters and thermal expansion coefficients between GaN and sapphire and among the 4-$GaN/Al_xGa_{1-x}N$ layers, especially with large content of Al. However, we believe the most strain effect is the one

that is due to the GaN/sapphire misfit and the one that is due to misfit between GaN and AlGaN layer that deposited on it because of the larger misfit between GaN/sapphire and GaN/AlGaN with larger Al content as seen in Table 2.

It is difficult to separate the effects of strain caused by lattice parameter mismatch from ones involving thermal-expansion mismatch to exactly determine their influence on the optical properties of GaN epilayers. However, the overall effect of strain generated in GaN on sapphire is compressive, which results in an increased band-gap (blue shift). It is also more difficult to separate the effects of strain induced by the 4-GaN/$Al_xGa_{1-x}N$ layers in addition to GaN/sapphire strain from each other.

To examine this assumption, we performed lift-off for the sapphire substrate from the 4-GaN/$Al_xGa_{1-x}N$ heterostructure for the first time ever to the best of our knowledge.

The lattice mismatch between GaN and sapphire substrate leads to high density of extended defects, such as dislocations [Lester et. al.[25] and Akasaki et. al.[94]]. High density of dislocations in GaN causes deterioration in the operation of optoelectronic devices mainly by [Porowski et. al.[31]]:

1. Serving as non-radiative recombination centers for electrons and holes leading to heat generation instead of optical emission.
2. Disturbing the epitaxial growth, thereby making perfect flat structures difficult to obtain.

EXPERIMENTAL DETAIL

The two samples studied were grown using hydride vapor phase epitaxy (HVPE) method. The structure for the two samples was AlGaN/AlGaN/AlGaN/GaN/sapphire. The backside of the sapphire substrate was polished. Table 3 and Table 4 show descriptions for the two samples in detail. Layer numbering started from the substrate. AlGaN layers compositions were estimated by means of X-ray diffraction for both samples. The layer thicknesses were determined by scanning electron microscope SEM on a dummy wafer.

Wavelength-base and time-base photoluminescence (PL) experiments were performed using the 244 nm line of a frequency-doubled cw Ar+ laser. A typical PL setup is shown in Figure 21. The sample was mounted in a variable-temperature cryostat cooled by a closed-cycle helium refrigerator. The PL spectra were detected with a photomultiplier tube in conjunction with a 1-m high-resolution double-grating spectrometer.

GaN decomposition performed using the laser lift-off LLO technique. 248 nm 20 ns KrF Lambda Physik Excimer laser pulse beam energy was utilized. The beam was focused with a fused silica convex lens with a focal length of 30 mm through polished sapphire face as in seen in Figure 28. The structure was placed on a motorized horizontal rail stage and the beam spread on sapphire side to insure homogenous distribution for the beam.

A sapphire wafer was bonded to the surface of the GaN thin film using two parts "Durabond 950 FS" metallic adhesive mix from "Cotronics" which also has been tested to show slow reaction with HCl etching. The following structure has been formed:

"Sapphire substrate/GaN/AlGaN/AlGaN/AlGaN/adhesive/sapphire wafer". The 248 nm 20 ns KrF Lambda Physik Pulsed Excimer laser beam energy was altered from about 550 mJ to 750 mJ as seen in Table 6. After a successful lift-off, a thin Ga layer on the surface of the exposed interface was removed by etching process using a 1:1 solution of hydrochloric acid (HCL) and de-ionized water. Since the highest density of the threading dislocation is located at the GaN/sapphire interface the lift-off relive the stress and reduce associated defects caused by the lattice mismatch. The surface then cleaned by acetone and methanol.

We tried to find the best lift-off parameters so that no damage for any of the layers. From Table 5 the AlN and the GaN melting points are 3500 and 2800 K respectively and from Figure 40 the decomposition temperature for GaN is 1250 K at atmospheric pressure. Therefore obtaining a damaged free GaN side will lead to a damaged free, freestanding $GaN/Al_xGa_{1-x}N$ heterostructure. We estimated the decomposed surface layer of GaN to be in the range of the penetration depth of the 248 nm KrF pulsed laser that is about 75 nm, in agreement with Wong et. al. [38]. This is negligible in comparison with the GaN 2.2 μm layer thickness. Following each lift-off trial and after the etching, we performed PL scan at temperature 10 K to examine the quality of the sample after the lift-off and select the proper lift-off parameters. As seen in Figure 46, lift-off at energy 550 mJ showed no AlGaN peak emission, only GaN peak has been observed for the

excitation of the GaN side, whence damaged free GaN and consequently damaged free 4-GaN/$Al_xGa_{1-x}N$ heterostructure has been obtained.

Once we the obtained the best condition for free-damaged lift-off GaN surface we formed more complicated structure, that is:

"Sapphire substrate/GaN/AlGaN/AlGaN/AlGaN/vacuum grease/thin copper sheet /adhesive/thin Al foil/microscopic slide".

The reason for this structure was to obtain freestanding 4-GaN/$Al_xGa_{1-x}N$ layers in order to compare the PL emission from the AlGaN side before and after the removal of substrate. The microscopic slide was used to temporally support the sample during the lift-off procedures. The Al foil was used to wrap the microscopic slide, so that the removal of the structure is possible without a complicated technique by using a cutter to cut the Al foil. The Al foil also dissolves by the HCl in seconds. To dissolve the metallic adhesive we used 1:1 solution of HCl and de-ionized water. We tested all the materials used in this structure for HCl reaction separately. Al foil reaction was the fastest within few second. However, we avoided any contact between the HCl solution and the AlGaN side. To do so a square piece of thin copper sheet about 4 mm X 4 mm was attached to the most upper AlGaN layer with vacuum grease. The vacuum grease is very easy to take off by "Trichloroethyler". The AlGaN side is then can be cleaned by "acetone and methanol".

Small drops of HCl solution were applied on the metallic adhesive just above the thin copper plate. The area of the adhesive that covers the copper plate is dissolved within

minutes without any contact between the AlGaN layer and the HCl. The metallic adhesive surface was showered frequently by methanol during the chemical lift-off to avoid any diffusion of the HCl solution on the surface of the adhesive or to the layers. Once the area of the adhesive that covered the copper sheet is dissolved, the copper plate picked up and removed easily, making a window-like at the AlGaN side without any harmful procedures for the epilayers. The remaining adhesive served as a supporting frame for the freestanding 4-GaN/$Al_xGa_{1-x}N$ heterostructure layers as illustrated schematically in Figure 41. The sample then was cleaned by "Trichloroethyler, acetone and methanol" to remove the vacuum grease. The GaN surface etched using 1:1 solution of HCl and de-ionized water. The quality of the lift-off examined via the PL emission from the GaN side. The PL from the AlGaN side before and after lift-off has been measured using the setup described above.

Data and analysis

Figure 43 shows a comparison between the PL at temperature 12 K of the two samples described in Table 3 and Table 4. Sample # 387 showed deeper UV spectra. This deeper emission is due to the fact that sample # 387 has more 30% AlN content more than that of sample # 386. Several peaks appeared between the two majors peaks (A & B) of the sample # 387. We believe these peaks are due to the interference of the incident beam at the multilayer interfaces. Figure 44 shows the temperature dependent PL for sample # 386. The emission showed the "S-shaped" PL peak energy shift (decrease-increase-decrease). Furthermore the intensity of "peak B" quenched at temperature 160K (decreased from 12 K until 140K-increased at 160K-then decreased at 180 until 300 K).

This anomalous effect has seen more aggressively for the higher AlN content sample (# 387) as seen in Figure 45. The transition energy as a function of the temperature departed violently from the well-known Varshni equation [equation 9]. For peak (B), the change in the intensity showed fluctuation that is more aggressive. The intensity decreased until T=100 k then increased until T= 130 K then decreased again until T= 300 K.

Figure 47 shows the normalized PL integration intensity for the higher AlN content sample (# 387) on sapphire. As seen in the figure the intensity of "peak A" decreased as typically occurs in GaN. However, for "peak B" an anomalous behavior has been observed. At temperature T=100 K the intensity increased until T=130 K then decreased again until temperature T=300 K.

Figure 48 shows the PL peak energies for the peak (A) and peak (B) of both samples before and after lift-off at low temperatures. The PL emission for sample # 387 on sapphire has higher energy (blue shift), indicating the presence of a compressive-biaxial strain [Perlin et. al.[62] and Bernard[59]]. They related this residual strain to the difference between the thermal expansion coefficients of GaN ($5.59 \times 10^{-6}\ K^{-1}$) and that of sapphire ($7.5 \times 10^{-6}\ K^{-1}$) [Perlin et. al.[62]], which cause a biaxial strain to develop during the sample cool down process from the growth temperature. However, the situation here is very much more complicated than in the case of only GaN epilayer deposited on sapphire. The structure consisted of four layers deposited on sapphire, therefore there many mismatches among this structure. This complexity seen more clearly in the case of

sample # 386. As seen in Figure 48 for sample # 386, peak (A) red-shifted while peak (B) blue-shifted.

On the other hand, for the sample with lower AlN (Sample # 386), the fluctuation in the PL peak energy reduced after the lift-off and the Varshni equation fitting showed smother curve than before the lift-off. For the sample with higher AlN concentration (Sample # 387), the PL peaks energy showed red-shift in general, however the curve is still far from obeying the Varshni equation[95]

$$E_T = E_0 - \alpha T^2/(\beta + T) \qquad (14)$$

where E_0 is the transition energy at 0 K, E_T is the photon energy at temperature (T), and α and β are Varshni thermal constants. This is agrees with Cho et. al.[93], that is the anomalous emission behavior increased as the Al content increased. We believe the irregularity increased as the Al content increased because the strain induced by the physical constants misfit increased as the Al content increased.

The intensity behavior after the lift-off

After the lift-off, we noticed that the intensity decreased in time at the same temperature. To confirm that this phenomenon occurred after the lift-off only, we performed a PL time-base scan for the samples at peaks A and B before the lift-off at temperature 12 K, and excitation power 10 mW. No change in the intensity has been observed before the lift-off. Figure 49 shows the time base scan for sample # 387, peak B, on sapphire.

The temperature dependent-time base scans PL for the same sample (#387) is shown in Figure 50 for “peak B”. After the alignment and optimization of the setup, the sample lifts in dark at room temperature for long time. The sample then is cooled in dark to temperature 12 K and left for about 30 min then excited at laser power 10 mW. Time base scan at “peak B” has been taken for time t=20,000 sec. The sample is annealed again at 300 K for 30 min in dark then cooled to 50 K for about 30 min and excited and scanned for time t=20,000 sec, and so on for temperatures 100 K, 150 K ,200 K and 300 K. The observed photoquenching is temperature dependent. For example at 12 K and 50 K when illumination is turned on the PL emission starts to decrease to go through a minima with a time constant that depend on the temperature. For temperature 12 K this decrease lasts about 800 sec and for temperature 50 K about 400 sec. Then the emission intensity starts to increase with a much longer time constant. At temperature 50 K the final emission after a along time even exceeds the initial values for both the 12 K and 50 K emission observed before any photoquenching.

The temperature dependent-time base scan at “peak A” is seen Figure 51 is performed with the same procedure used for peak B. The scans showed photoquenching however the detail is some how different and the photoquenching did not recovered even at room temperature.

Proposed Models

1. Before the lift-off

Figure 52 (a) shows the relationship between the PL intensity and the temperature for sample # 387, peak (B), before the lift-off and the relationship between the PL peak position and the temperature before the lift-off for the same sample and peak. Figure 52 (b) shows the relationship between the PL intensity and the temperature for peaks (A) and (B) of sample # 387 before the lift-off. Figure 52 (c) shows a proposed model for the photoquenching of the temperature dependent PL intensity and peak position of the 4-GaN/$Al_xGa_{1-x}N$ heterostructure, sample # 387- peak (B), shown in Figure 52 (a) and Figure 52 (b) before the lift-off of sapphire substrate. From T = 12 K to T ~ 100 K, metastable neutral defects centers captured some electrons in a nonradiative process. The emission is due to band-to-band transition, with relatively low intensity, between electrons in conduction band that are not captured and the holes in the valance band. From T >100 to T = 130 K, the rapid redshift indicated that phase change in the material has happened most likely due to a modification of the strain from compressive to tensile or because of substantial relaxation for the strain. The rapid increase in the intensity indicated that there is no more trapping i.e. the metastable defects are not active any more. For temperatures T > 130 to T = 300 K the intensity is normalized to show consistent decrease with “peak A” and the peak energy showed the normal redshift with increasing temperature.

2. After the lift-off

The “decrease-increases-decrease” in the intensity with time at 12 K, shown in Figure 50, is corresponding to three different luminescence mechanisms [Laiho et. al.[96]].

This indicated the existence of three channels of metastable defects that can be generated at the current excitation conditions and temperature [Huang et. al. [97] and Kuisma et. al.[98]].

On the other hand, Figure 48, the peak energy versus temperature, showed a "zigzag-like" behavior. This indication that the generation or the activation of the metastable defects channels is temperature dependent i.e. they turned on/off in a temperature dependent manner. This is also seen in the change of intensity with time at different temperature, Figure 50. The photoquenching recovered thermally at temperature 200 K<T <300 K for the peak (B) but it did not recover for the peak (A) even at T = 300 K. Some articles reported thermal recovery at temperature as high as 520 K, for example for GaAs defects [Kuisma et. al.[98]]. Figure 53 shows a model to describe the energy transitions after the lift-off. After the substrate was removed, the strain is relaxed but at very low temperature, the metastable defects still trap electrons. One of the possible mechanisms, (for example at 12 K with a help from Figure 50), as the highest metastable level is trapping electrons, the intensity decreased with time. Once this level is saturated, there is no more trapping at this level, the intensity reached minimum, electron-holes recombination is started to optimize, the intensity started to increase. At time, about 10000 sec the intensity reached maximum then started to decrease in longer time t > 20000 sec. The long time for the increase and the longer time for the decrease is indication that the lower defect levels are populated by more complicated paths [Laiho et. al.[96]]. From Figure 48 (for peak B, sample # 387), it is expected that the metastable levels lay between photon energy $h\nu$ = 4.62 eV and $h\nu$ = 4.645 eV (λ = 268.36 nm to λ = 266.92 nm). In order to detect and identify these defect levels, several excitation energies

need to be used in this limit. Unfortunately, in this UV range the choices are very limited for the PL.

In GaAs, the metastability is associated with the lattice relaxation [Krambrock et. al.[99]]. The metastability in GaAs is usually studied by utilizing different excitation energy at different temperatures so that these metastable states can be activated independently and therefore can be identified. For example Kuisma et. al.[98] generated a metastable state of As_{Ga} effectively with photon energy, $h\nu$ = 1.15 eV and generated a second metastable state for the same sample with $h\nu$ =1.075 eV. Unfortunately, due to experimental limitation the optical generation could not apply for this study.

However, we believe the metastability is associated with strains induced by the lattice and thermal coefficients mismatch between the GaN and the sapphire substrate and the mismatch between the GaN and the AlGaN layer that are directly deposited on it especially the layers of higher Al content. The strains induced metastable defects. The behavior and the detection of these defects can be altered or modified if the strains are modified thermally or by the lift-off for sapphire substrate.

Conclusion:

We performed laser lift-off for GaN/AlGaN multilayer for the first time to the best of our knowledge. We compared the PL at low temperatures before and after the lift-off at low temperatures. From the PL emission, the sample on sapphire has higher energy, indicating the presence of a compressive-biaxial strain.

Though the separation of the sapphire substrate made some modification for the peak energy, we noticed that the intensity after the lift-off changed with time significantly. This indicates the existence of metastable defect channels in the samples. Two models are proposed to describe the way these metastable channels work before and after the lift-off for the sapphire substrate. Further investigations need to be done for these anomalous behaviors.

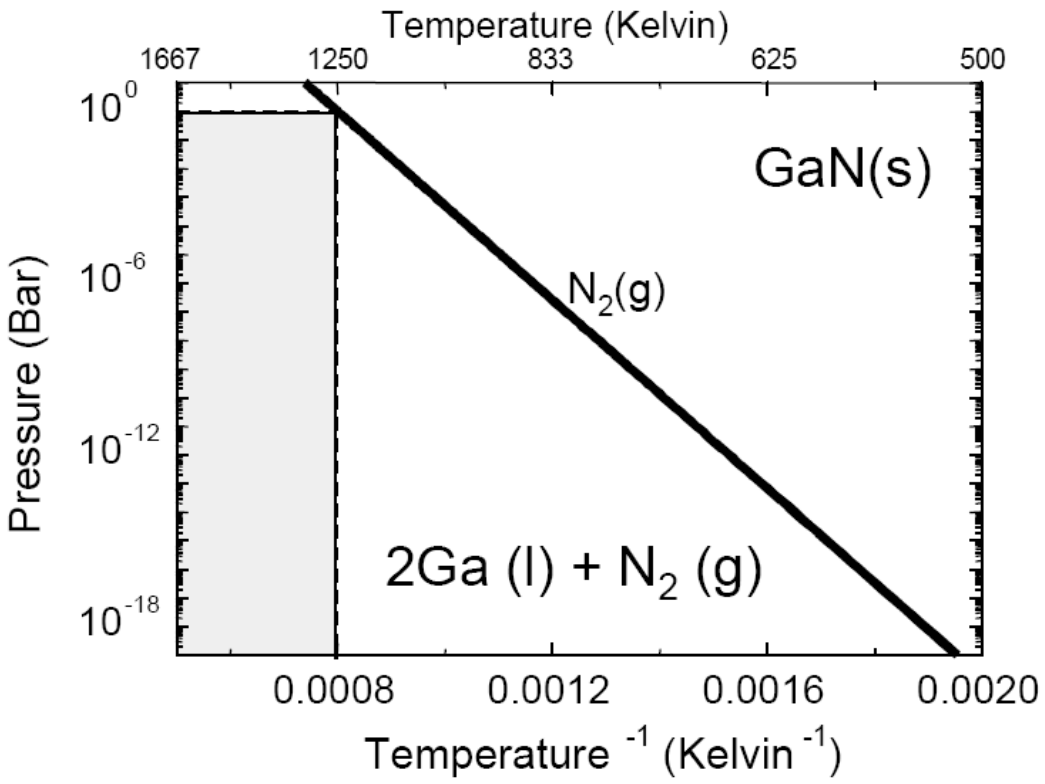

Figure 40. Pressure-temperature curve for GaN. The rectangular area to the left is where GaN decomposes at 1250 K. [Adopted from Ref. 100]

Table 3 : Description of sample # AP386

Layer #	Material	AlN Content, Mole %	Doping	Thickness, μm
Layer # 4	AlGaN	28.8	No	0.38
Layer # 3	AlGaN	13.5	No	0.17
Layer # 2	AlGaN	24	No	0.34
Layer # 1	GaN	0	No	2.19
Substrate	Sapphire	Sapphire		

Table 4: Description of sample # AP387

Layer #	Material	AlN Content, Mole %	Doping	Thickness, μm
Layer # 4	AlGaN	38.3	No	~0.4
Layer # 3	AlGaN	14.3	No	~0.2
Layer # 2	AlGaN	33.4	No	~0.4
Layer # 1	GaN	0	No	~2.2
Substrate	Sapphire	Sapphire		

Table 5: Melting points of the group III-V nitrides.

Material	Melting Temperature (K) theoretical	Reference
AlN	3500	101
GaN	2800	101 and 102
InN	2200	103

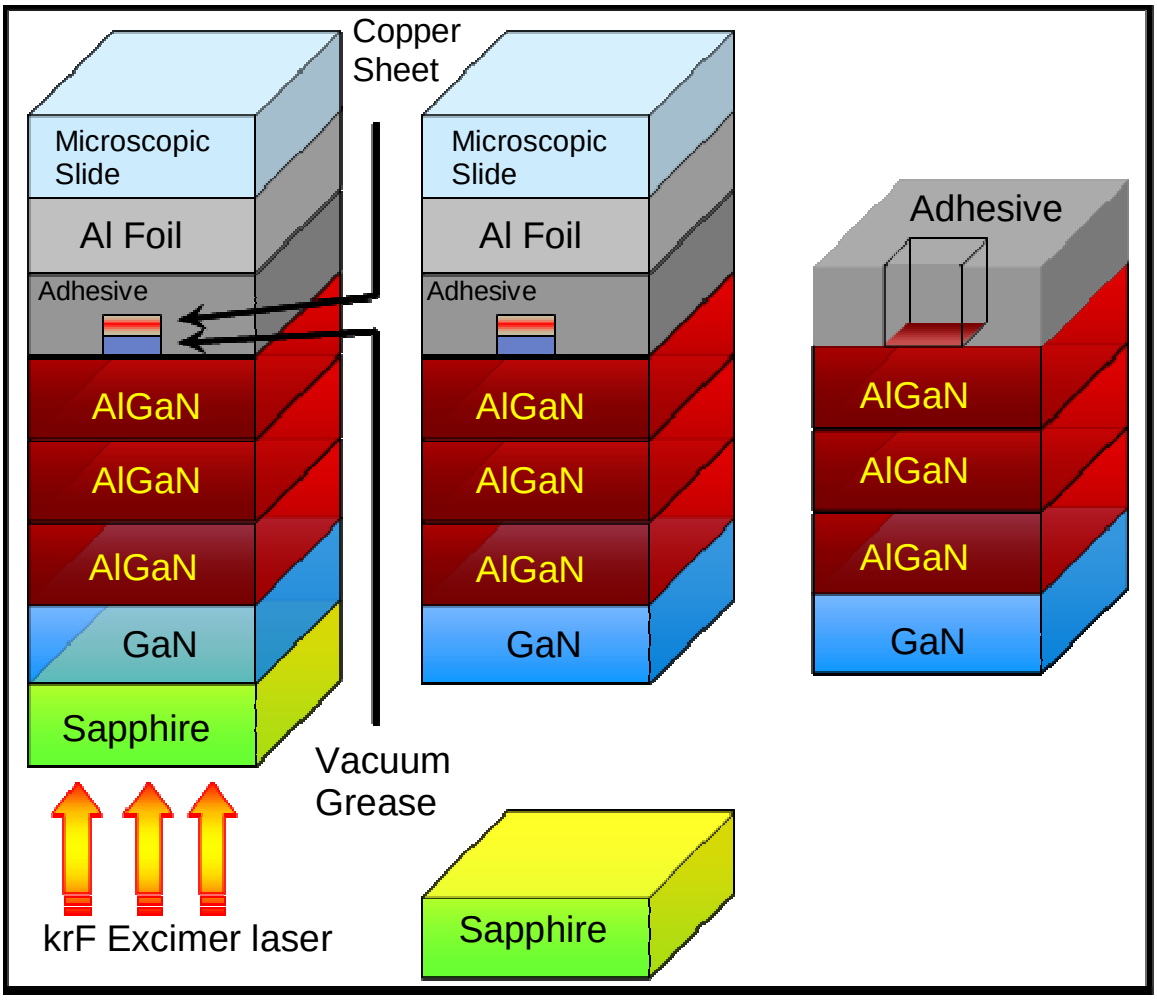

Figure 41. Laser lift-off for sapphire substrate, and the freestanding 4-GaN/$Al_xGa_{1-x}N$ heterostructure after the chemical lift-off for a part of the adhesive. The rest of the adhesive served as a supporting frame. The figure shows a cross-section in the structure. The dimensions are not to scales.

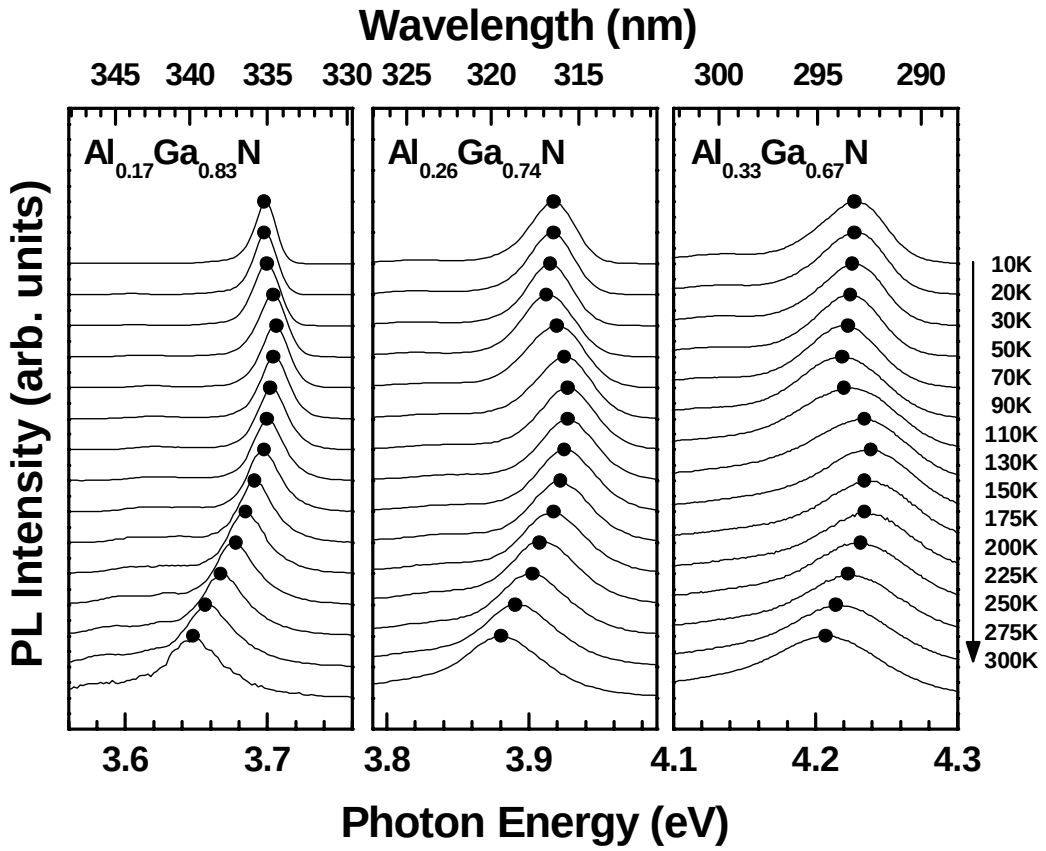

Figure 42. PL Spectra for GaN/AlGaN heterostructure in the temperature range from 10 K to 300 K. The emission peak shows S-shaped (increase-decrease-increase) behavior with increasing temperature. After Cho and J. J Song.[93].

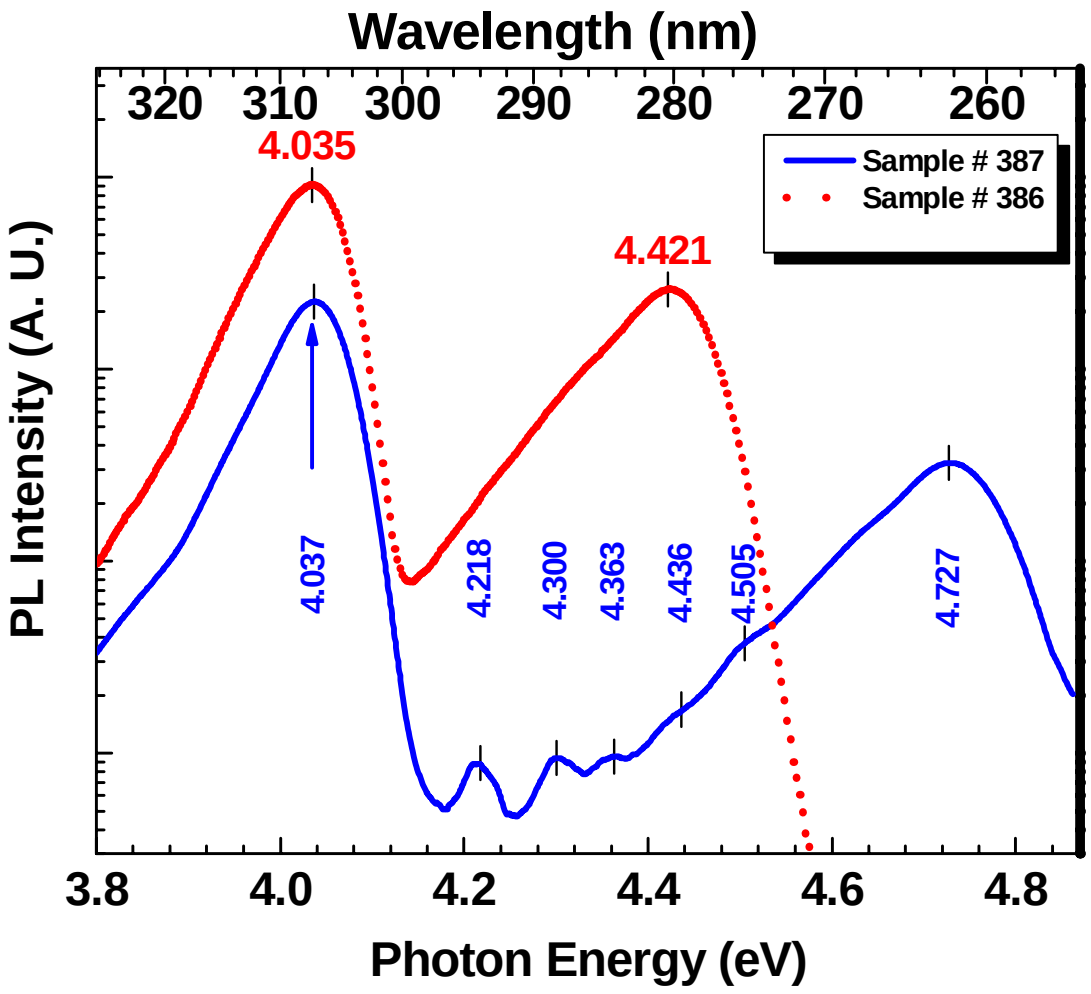

Figure 43. The PL spectra for the two 4-GaN/$Al_xGa_{1-x}N$ heterostructure samples at temperature 12 K.

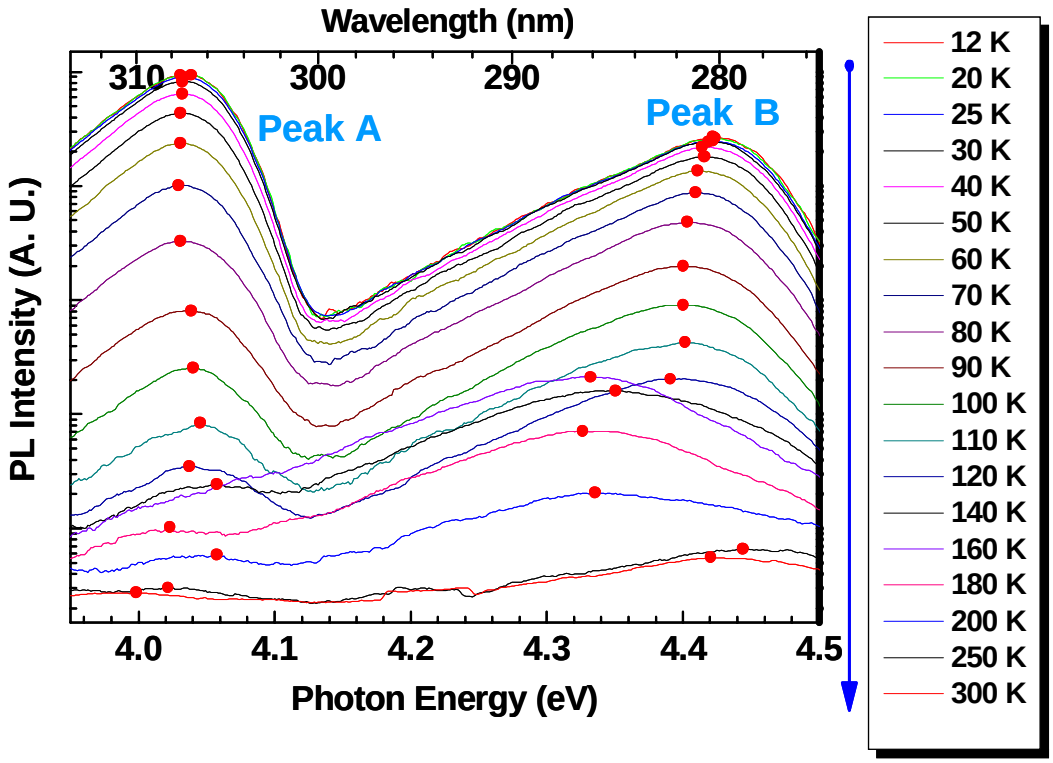

Figure 44. Temperature dependent PL for sample # 386.

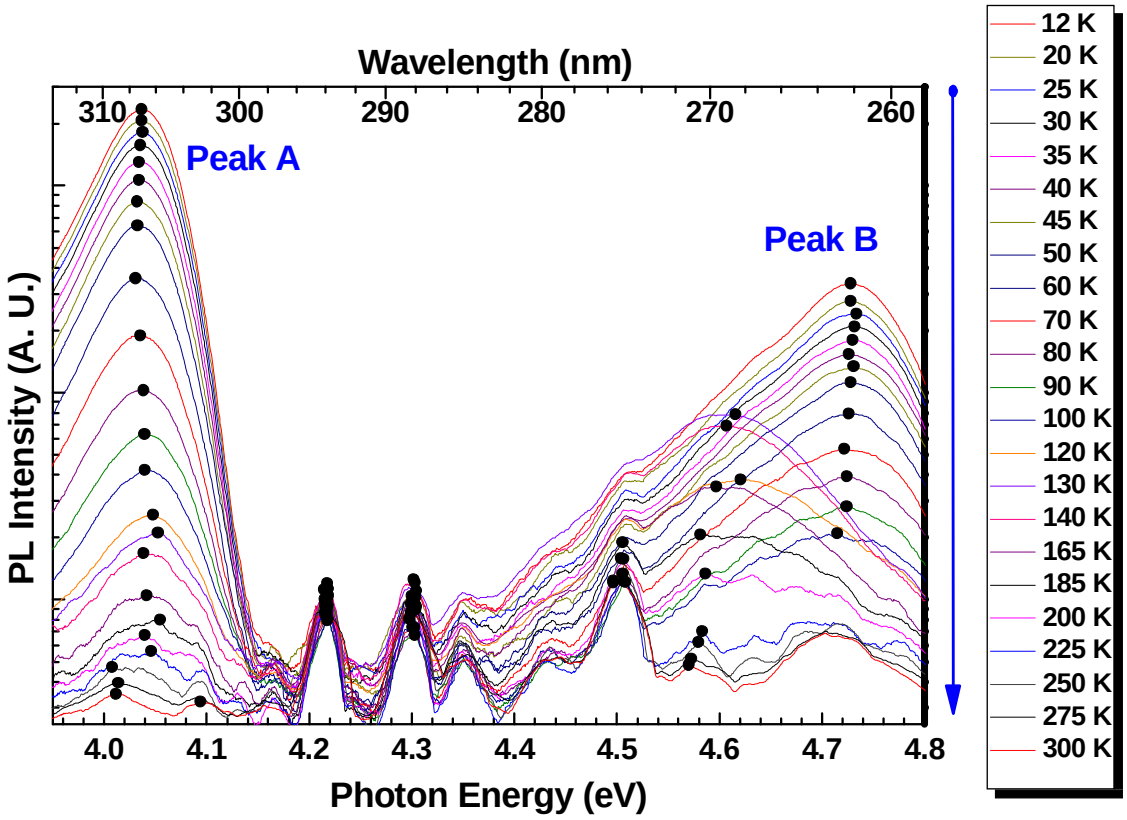

Figure 45. Temperature dependent PL for sample # 387.

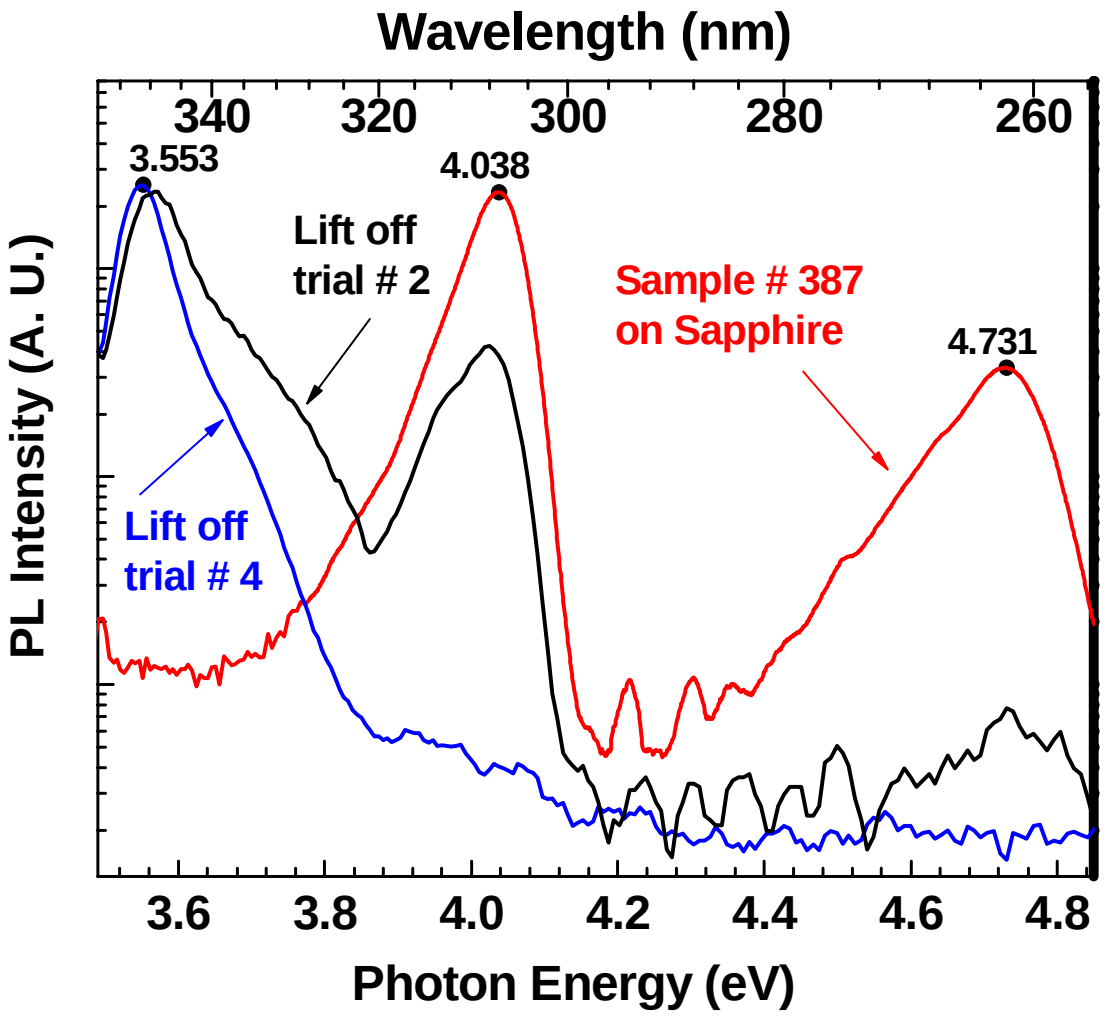

Figure 46. The PL at temperature 10 K for sample # 387 on sapphire and after two lift-off trials. The trials parameters shown in Table 6.

Table 6. Lift-off parameters.

Trial #	Energy (mJ)	Exposure time (sec)	Repetition rate (Hz)
1	~ 750	~ 60	5
4	~ 550	~ 120	5

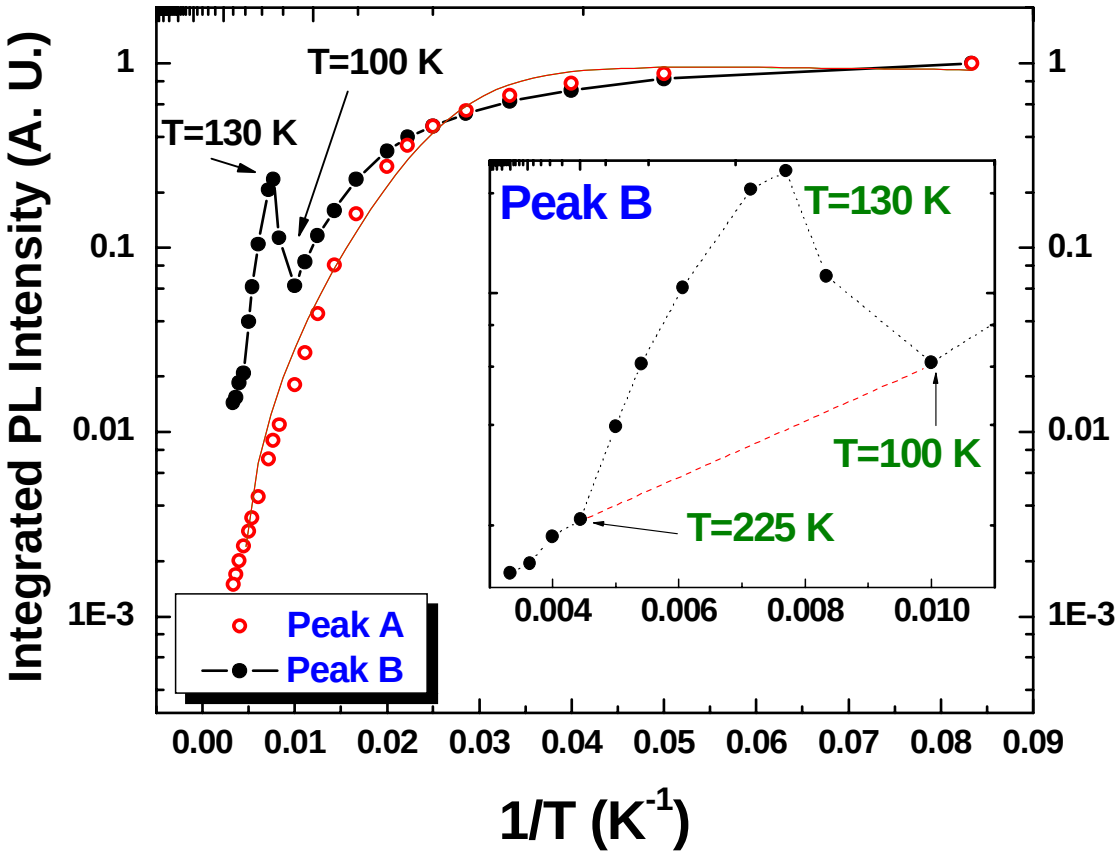

Figure 47. The normalized integrated intensity for sample # 387 on sapphire.

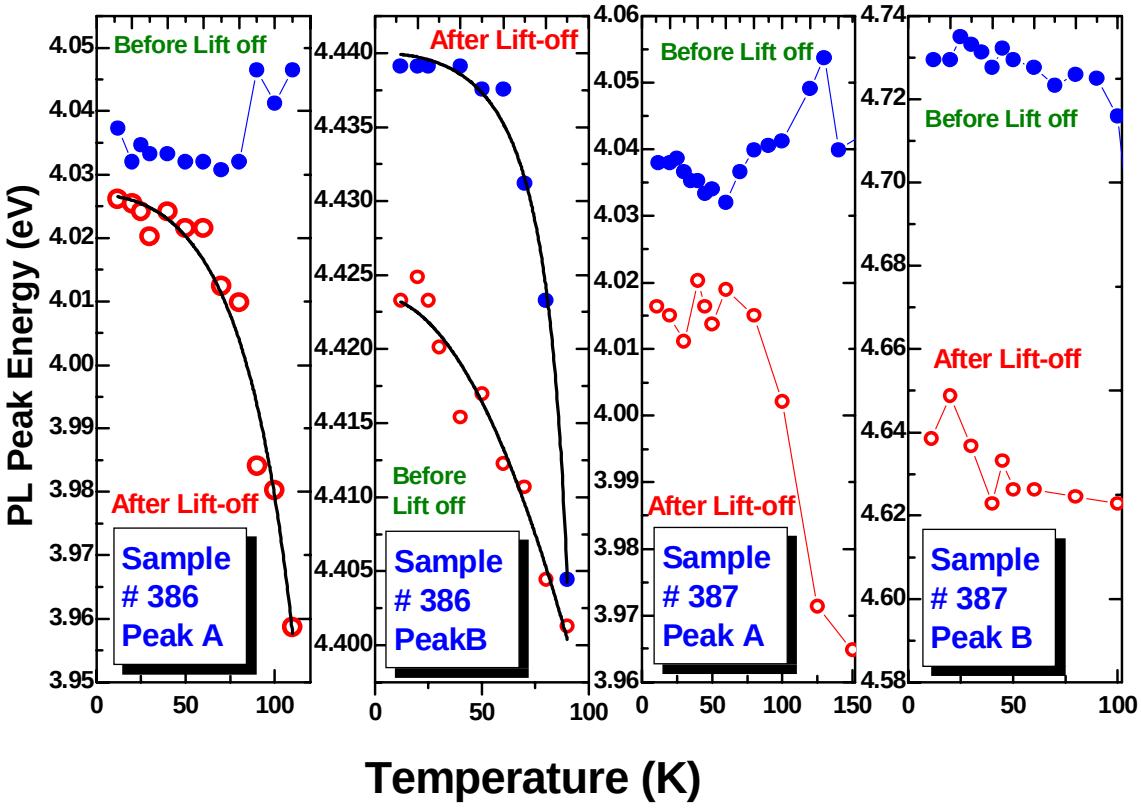

Figure 48. PL peak energy for samples # 386 and # 387 before and after the lift-off for sapphire substrate.

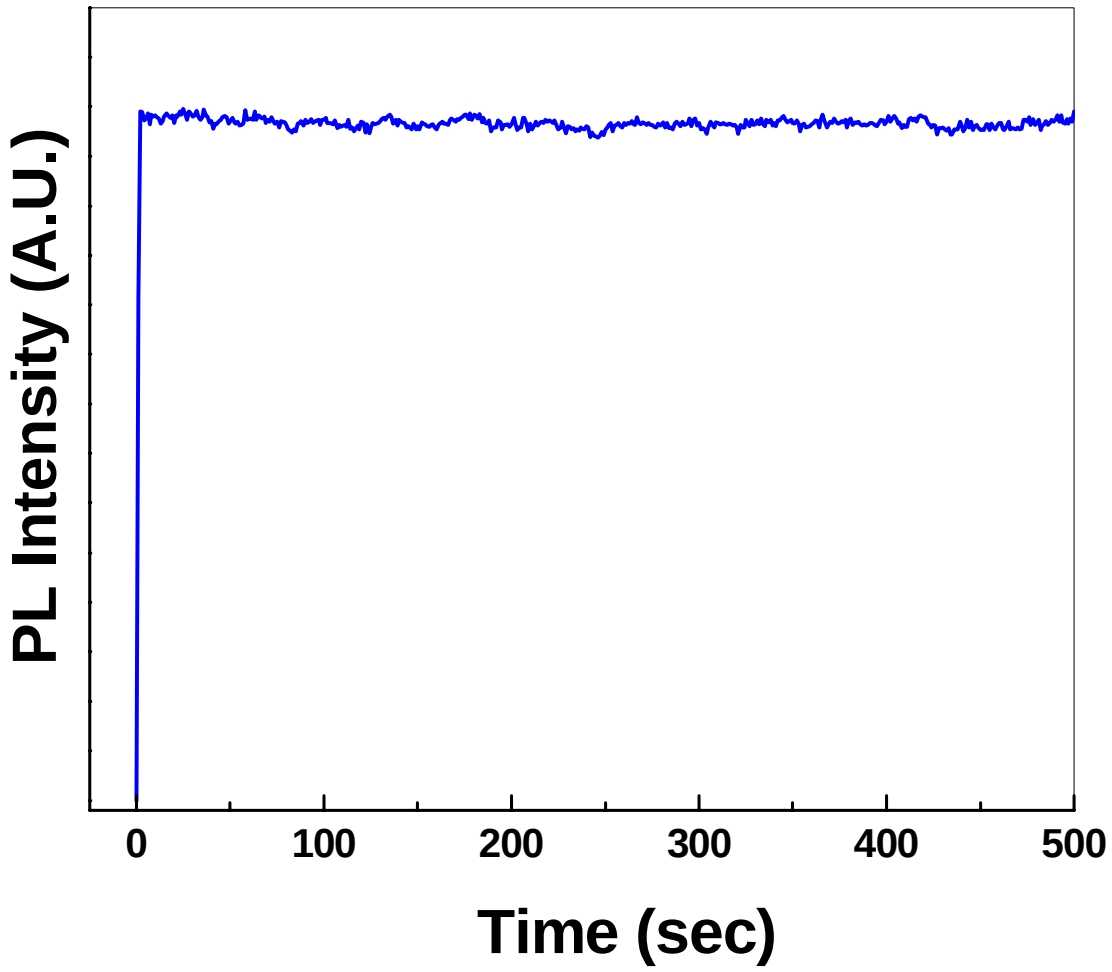

Figure 49. Time base scan at 10 K for sample # 387 on sapphire at peak 269.4 nm, temperature 12 K, and excitation power 10 mW.

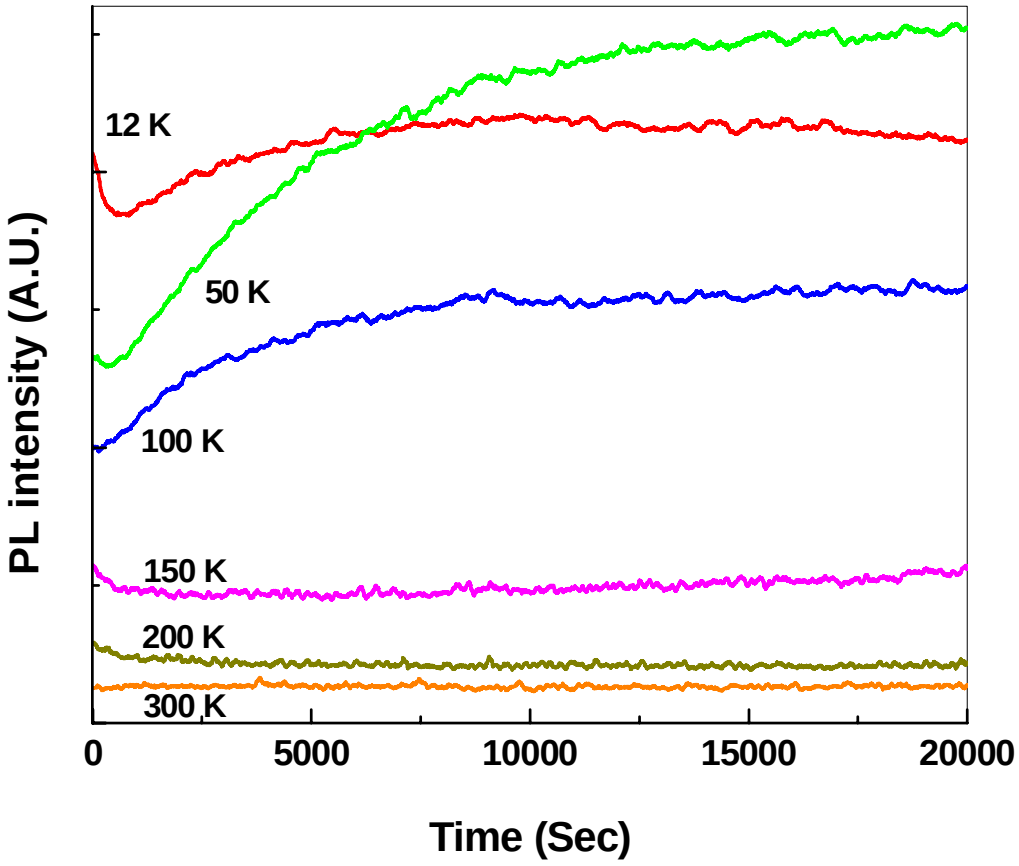

Figure 50. Temperature dependent-time base scan for sample # 387 after lift-off at peak (B).

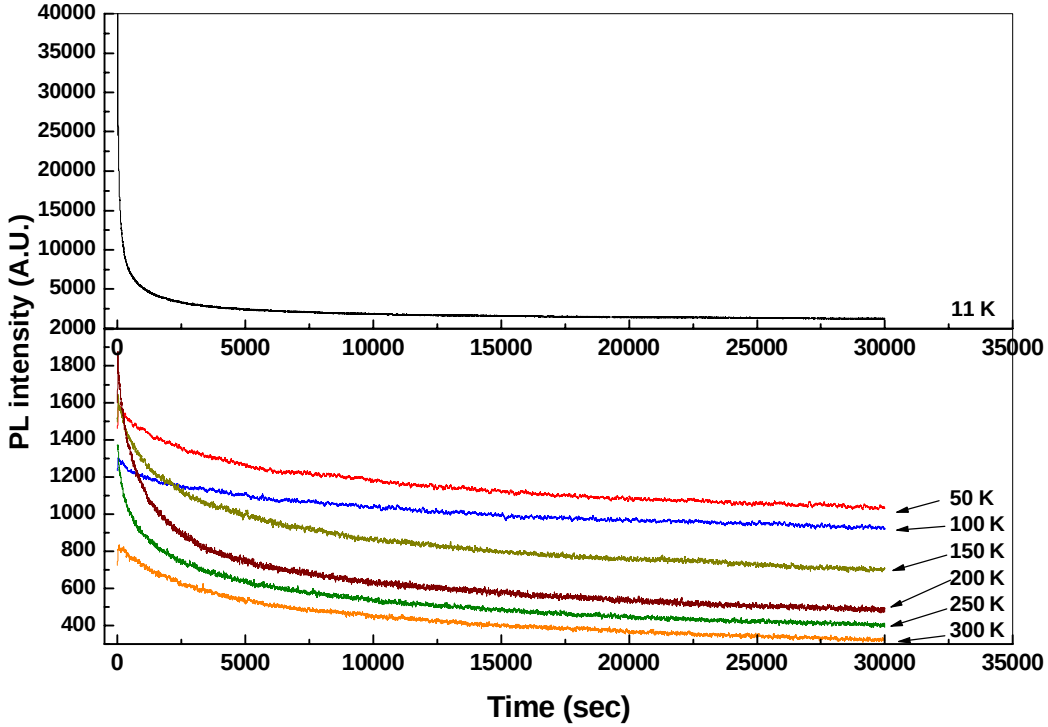

Figure 51. Temperature dependent-time base scan for sample # 387 after lift-off at their peaks.

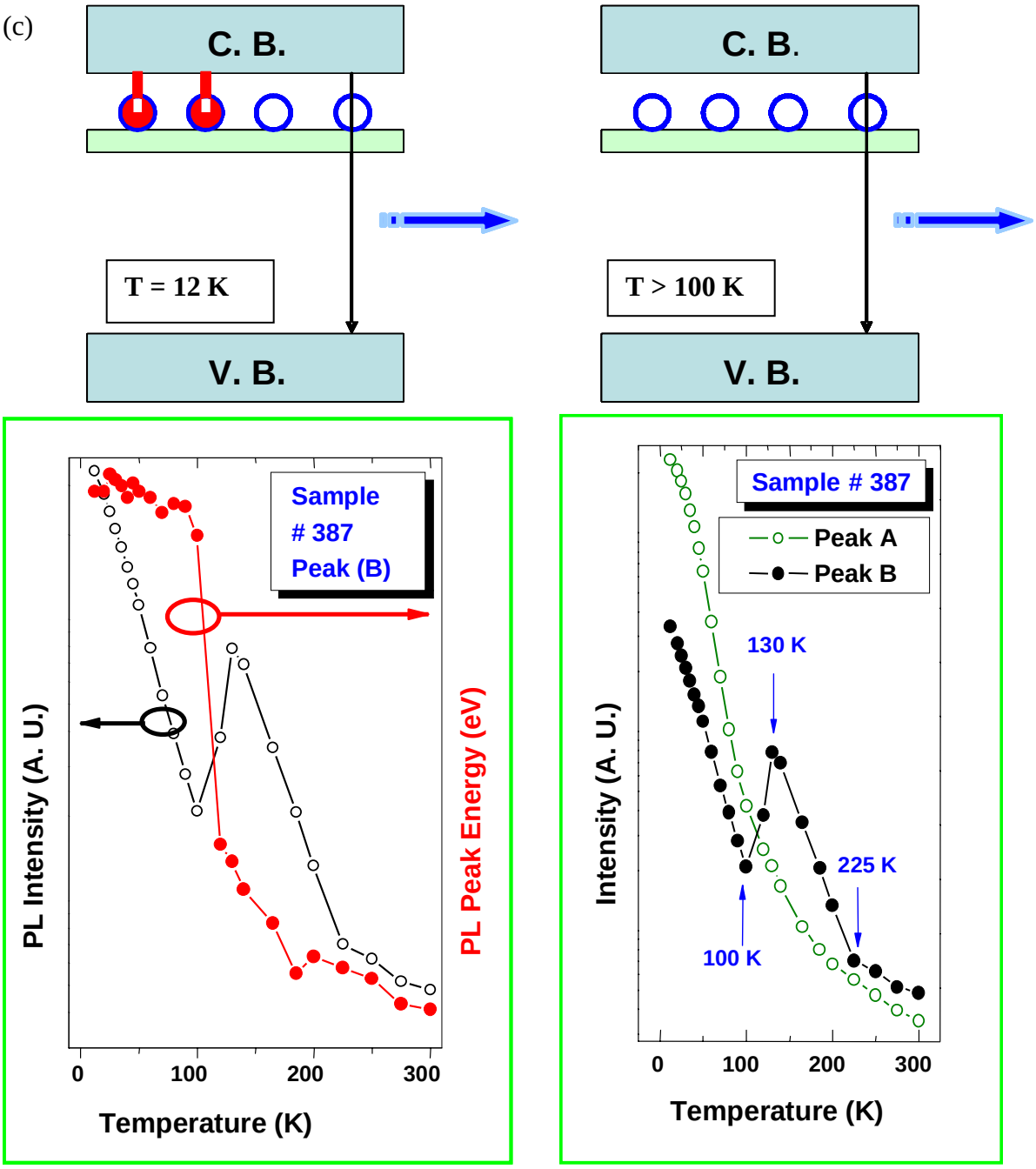

Figure 52. (a) Shows the relationship between the PL intensity and the temperature for sample # 387, peak (B), before the lift-off and the relationship between the PL peak position and the temperature before the lift-off for the same sample and peak. (b) Shows the relationship between the PL intensity and the temperature for peaks (A) and (B) of sample # 387 before the lift-off. (c) A proposed model for the photoquenching of the temperature dependent PL intensity and peak position of the 4-GaN/$Al_xGa_{1-x}N$ heterostructure, sample # 387, shown in Figures (a) and (b) before the lift-off of sapphire substrate.

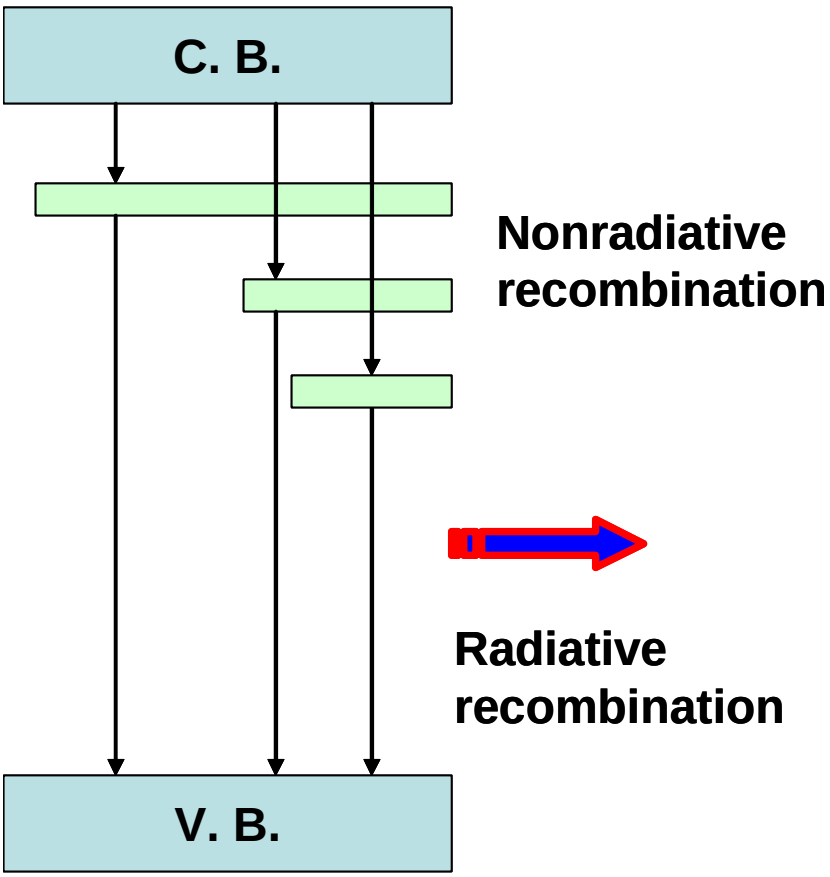

Figure 53. A proposed model for the photoquenching of the temperature dependent PL of the 4-GaN/$Al_xGa_{1-x}N$ heterostructure after the lift-off for sapphire substrate.

CHAPTER VIII

Investigation of the Strain and Piezoelectric Effects on The Optical and Electrical Properties of $Al_{0.2}Ga_{0.8}N$/GaN Heterostructure Grown by HVPE for HEMT (High Electron Mobility Transistor) Applications

Introduction

A major problem for the performance of AlGaN/GaN heterostructure is a high dislocation density at the AlGaN/GaN interface. In this chapter, we present the effect of strain due to lattices/thermal coefficient mismatches between GaN and sapphire substrate and between GaN and AlGaN epilayers on the optical properties of GaN/$Al_{0.2}Ga_{0.8}N$ grown on a *c*-plane sapphire substrate by HVPE (hydride vapor phase epitaxy) for HEMT applications. It is well known that the strain due to lattice/thermal expansion mismatches generates many crystal defects and dislocations that have a profound effect on the optical and electrical properties of heterostructure.

$Al_{0.2}Ga_{0.8}N$/GaN heterostructure was grown by hydride vapor phase epitaxy on a c-plane sapphire substrate for HEMT applications. The theory and the basic of operation of the 2-dimentional electron gas (2DEG) and the HEMT are explained in details chapter IV. Capacitance-voltage measurements showed a very high carrier concentration, but Hall measurements showed a low mobility. We believe the low mobility is a consequence of the lattice/thermal expansion misfit between GaN epilayer and sapphire and between $Al_{0.2}Ga_{0.8}N$ and GaN epilayers. The effects of these misfits have investigated by photoluminescence measurements.

Photoluminescence (PL) was measured over a temperature range of 10 to 300 K. Free excitons, Γ_5 and Γ_6, were observed. Three other peaks were observed at higher energy than the free excitons. We believe these three peaks are polariton excitons PX_1, PX_2 and PX_3. Two donor-bound excitons (DX_1 and DX_2) were also observed. A very strong broad emission peak observed is related to the recombination between the two-dimensional electron gas (2DEG) electrons in the conduction band and the holes in the valance band. Another peak occurs just below most upper sub-bands of the 2DEG and exhibits excitonic behavior. We attribute this peak to interface exciton (IX).

Experiment details

The sample investigated was an $Al_{0.2}Ga_{0.8}N$/GaN structure grown by hydride-vapor-phase-epitaxy (HVPE). The sample started with a very thin 2.0 μm layer of

undoped GaN grown on c-plane sapphire. Next, a 40.0 nm undoped $Al_{0.2}Ga_{0.8}N$ layer was grown on the GaN layer by HVPE. The photoluminescence (PL) was measured using the 325 nm line of a cw HeCd laser. The sample was mounted in a variable-temperature, angle-adjustable cryostat cooled by a closed-cycle helium refrigerator, and the PL spectra were recorded with a photomultiplier tube in conjunction with a 1-m high-resolution spectrometer. Figure 21 shows the photoluminescence measurement setup and Figure 22 shows schematic diagram of surface emission geometry.

The carrier concentration in the $Al_{0.2}Ga_{0.8}N$/GaN heterostructure was measured by the Capacitance-Voltage profiling technique. The electron mobility was determined from Hall measurements.

Data and Analysis

I. Free Excitons

Figure 54 shows the near band gap temperature dependent PL spectra. Two peaks identified as free excitons Γ_5 and Γ_6 dominated the spectra. Γ_5 and Γ_6 have photon energies of 3.4902 eV and 3.4843 eV at temperature 10 K respectively, and a separation of 5.9 meV. These values are in excellent agreement with the values reported by Fang et. al.[104] of 3.492 eV and 3.486 eV with a separation of 6.0 meV for a $Al_{0.15}Ga_{0.85}N$/GaN heterostructure with a 2.0 μm thick GaN layer grown on sapphire by metalorganic chemical vapor deposition (MOCVD). These free excitons were also seen by Reynolds et.

al.[53,105] for freestanding 200 µm thick GaN grown on sapphire by HVPE. Figure 55 shows the PL integrated intensity as a function of temperature for the free excitons Γ_5 and Γ_6. The solid lines in the Figure are fits to the equation [Kovalev et. al.[106]]:

$$\frac{I(0)}{I(T)} = \frac{1}{1 + C\exp(-\frac{E}{kT})} \qquad (15)$$

where I (T) is the intensity at temperature T, C is a prefactor, k is Boltzmann's constant, and E is the binding energy of the free exciton. To calculate the binding energy for Γ_5 and Γ_6 we have to take in account that Γ_5 and Γ_6 are under the influence of the DX_1 and DX_2 below 60 K. However higher temperatures free more of the donor-bound excitons, thus creating more Γ_5 free excitons and free donors [Viswanath et. al.[107]]. For this reason, the Γ_5 binding energy is deduced from the slope for the temperature region T > 60 K, where the donor-bound excitons DX_1 and DX_2 have collapsed and have only a negligible effect on the Γ_5 free exciton.

We obtained binding energy for Γ_5 as 35.6 meV using equation (10) [Viswanath et. al.[107]]. The value of the free exciton Γ_5 binding energy is much higher than the binding energy of A and B free exciton[1]. This is expected since the strain has some temperature dependent [108] and Γ_7^V, and Γ_9^V (A and B sub-valance band of GaN) transform to Γ_5^V, and Γ_6^V when the crystal field is modified by applied magnetic field and/or strain [Reynolds[53], Chen[54], and Kitaev[55]]. By adding the binding energy of Γ_5 to its transition energy at 10 K, E (Γ_5) = 3.490 eV, we obtain a band gap energy of 3.5256 eV. The band

[1] The binding energy of the *A* exciton is about 20 meV. A value of binding energies of the B and C excitons is about 18 meV. [J. Appl. Phys. **87**, 3, 965 (2000)].

gap for bulk GaN is 3.5 eV and 3.39 at temperatures 1.6 K and 300 K respectively [Bernard[59]]. The band gap of the epilayer is enlarged by the significant mismatch between the lattice constants of the sapphire substrate and the very thin 2.0 μm GaN layer and the difference in their thermal expansion coefficients. These mismatches give rise to misfit strain [Viswanath et. al.[107]]. This mismatch strain generates many crystal defects and dislocations that have a profound effect on the optical and electrical properties. Dislocations originate at the substrate interface[25, 109, 110] and the dislocations density decreases substantially with increasing film thickness away from the interface [Warren et. al.[111]]. The mismatch strain also increases the band gap energy, the exciton energies, and the separation between the exciton energies, which makes the excitons more resolvable. The strain decreases with increasing layer thickness. Deviation of the free-exciton energies in thin (< 4 μm) epilayers from the values reported for thick samples was explained by the strain effect. Volm et. al.[112] reported A (n=1) exciton energies of 3.4799 and 3.4962 eV for GaN of thicknesses 400 and 3.0 μm, respectively, grown on sapphire. This shows that the strain effect increased the transition energy of the A exciton (n=1) by about 16 meV. Similarly, they reported B exciton energies of 3.4860 and 3.505 eV for the 400 and 3.0 μm thick GaN epilayers, respectively, showing a strain-induced 19 meV shift. For the 3 μm sample, they also measured the A exciton (n=2) energy of 3.5162 eV with a binding energy of 26.1 meV, which sums to a band gap energy of 3.5423 eV.

Further evidence that strain increases the exciton energy is that our 2.0 μm thick GaN grown by HVPE on sapphire has a Γ_5 energy 8.6 meV higher than the Γ_5 (3.4814 eV) reported by Reynolds et. al.[53] for a free standing, strain-free 200 μm thick GaN layer,

grown on sapphire by HVPE. In addition, the separation Γ_5 - Γ_6 was 2.9 meV for their freestanding, strain-free 200 μm thick GaN layer while for our sample and that of Fang et. al.[104], the separation is about 6.0 meV.

A thermal activation energy of 16 meV for the Γ_6 free exciton was calculated for the temperature region T > 30 K, where DX_1 and DX_2 have less influence. To find the binding energy of Γ_6, we first fitted the integrated intensity of Γ_5 for the temperature range of 10 to 120 K, not shown in Figure 55 where Γ_5 is under the influence of the donor bound excitons, to obtain a binding energy about 27 meV. Then, we subtracted this value from the 35.6 (Γ_5 binding energy calculated earlier) to obtain 8.6 meV. Therefore, the bound excitons' influence on the free exciton Γ_5 decreases its binding energy by 8.6 meV. Assuming that the bound excitons have similar influence over the Γ_6 binding energy, we subtracted this value from the calculated activation energy of Γ_6, i.e. [16 eV – 8.6 eV = 7.4 meV], which is the binding energy for Γ_6. This is in good agreement with separation Γ_6 - Γ_5 = 5.9 meV measured from the temperature dependent PL as mentioned above.

II. Donor-Bound Excitons

Figure 54 shows two shoulders appearing below Γ_6. They behaved as what would be expected for bound excitons i.e. they collapsed at faster rate and lower temperatures than the free excitons Γ_5 and Γ_6. The first is the donor-bound-exciton, designated DX_1, 12.4 and 6.5 meV below Γ_5 and Γ_6 respectively at transition energy 3.4778 eV with intensity less than that of Γ_6. The position, separation and intensity relative to Γ_6 are

reasonable to what have reported by Reynolds et. al.[53,113] and Fang et. al.[104]. Figure 56 shows a fit for the integrated PL intensity for DX_1 as a function of the temperature following the Equation [Bernard[59]] :

$$\frac{I(0)}{I(T)} = \frac{1}{[1 + C_1 \exp(-E_b / kT) + C_2 \exp(-E_{Loc} / kT)]} \qquad (16)$$

where I (T) is the intensity at temperature T K, I (0) is the temperature at 0 K, C_1 and C_2 are prefactors determine from the fitting parameters, k is Boltzmann's constant. The thermally activated dissociation of bound exciton must involve two activation energies. One is the localization energy E_{Loc} and the higher is the donor binding energy E_b from which we can define the associated free exciton. The fitting gave E_{Loc}=4.4±0.1 meV and E_b=14.0±0.2 meV. The later is in excellent agreement with the separation between the Γ_5 and DX_1 transition energy 13.6 meV, which proves that Γ_5, is the associated free exciton to the bound exciton DX_1 i.e. $DX_1 - \Gamma_5 + D_1$.

The second shoulder 10.4, 16.9 and 22.8 meV below DX_1, Γ_6 and Γ_5 respectively at transition energy 3.4674 eV as seen in Figure 54, is corresponding to the donor-bound exciton DX_2 associated with Γ_6. The fitting obtained by Equation (2) shown in Figure 56 gave E_{Loc}=9.84 meV and E_b= 16.43 meV. The binding energy obtained for this shoulder is in an excellent agreement with the separation between this feature and Γ_6 (16.9 meV). This is an indication that this peak is another donor-bound exciton DX_2 associated with Γ_6 i.e. $DX_2 - \Gamma_6 + D_2$.

The great difference in the localization energies between DX_1 (E_{Loc}=4.4±0.14 meV) and DX_2 (E_{Loc}=9.84±0.02 meV) prove that they are not the same donor-bound excitons [Bernard[59]].

The presence of defect-induced two donor states in this structure is due to the threading dislocations present in the structure because of lattice mismatch as well as unintentional doping [Furis et. al.[114]]. Therefore, the free excitons can be associated with recombination processes involving defects localized on donor states.

III. Polariton Excitons

Other features are observed at energies 3.4971 eV, 3.5057 eV and 3.5158 eV about 6.9 meV, 15.7 meV and 25.8 meV above Γ_5 respectively, at T = 10 K, as seen in Figure 54 which we believe these features are polariton excitons PX_1, PX_2 and PX_3 respectively. These values are in reasonable agreement with the values reported by Fang et. al.[104] for $Al_{0.15}Ga_{0.85}N$/GaN heterostructure grown by MOCVD, where E (Γ_5) = 3.492 eV, PX = 3.505 eV with separation 13.0 meV.

The polariton exciton energy is defined as the energy of the interacting free exciton and photon i.e. polariton [Sell et. al.[115]]. To understand this definition we need to invoke the effects of the lattice mismatch and thermal coefficients mismatch between GaN and sapphire.

- The lattice mismatch

It is well known that GaN grows epitaxially on substrates (such as c-plane sapphire) in a columnar grain structure. These columns have a wurtzite (hexagonal) crystal structure.

It is also well known that these columns tend to rotate about their c axes. These columns can tilt by small angles with respect to the average c-axis direction of the total epitaxial layer because of the dislocation results from the GaN-sapphire substrate lattice-mismatch. The number of the columns is corresponding to the average number of the dislocation lines orientations.

- The thermal coefficients mismatch

Under the influence of (1) spin-orbit and (2) the crystal field, the valance band split into Γ_9^V, Γ_7^V, and Γ_7^V sub bands which called usually A, B and C. The crystal field is depending on the ratio between the lattice parameters. A magnetic field and/or a strain produce polarization field that may alter these ratios and therefore Γ_7^V, and Γ_9^V transform to Γ_5^V, and Γ_6^V [Reynolds[53], Chen[54], and Kitaev[55]].

The interaction between this polarized field and incident photons creates "polariton" and since this polarized field created new free exciton Γ_5, the name "polariton exciton" is used too. In other words, the interaction between the free exctions and photons creates "polariton excitons".

In summery "The form of three polariton excitons is associated with the existence of three columns or hexagonal grains having different orientations due strain induced by GaN-substrate lattice mismatch" [Reynolds et. al.[108]]. These columns may tilt or twist independently with the change of the physical conditions such as the temperature change.

According to Hopfield[116], Reynolds[113], Gil[117] and Stepniewski[118], the relationship amongst the polarizability (β), the free exciton (Γ_5), and the polariton excitons (PX) is given by

$$\Delta E = E(PX) - E(\Gamma_5) = E(\Gamma_5)\frac{2\pi\beta}{\varepsilon}, \qquad (17)$$

where E (PX) is the energy of the polariton exciton, $E(\Gamma_5)$ is the photon energy of the Γ_5 free exciton, β is the polarizability and ε is the dielectric constant, which varies between 5.15 and 5.73 depending on the author[113].

Figure 57 shows the measured photon energies of the free excitons Γ_5 and Γ_6 and the polariton excitons as function of the temperature and the fitting obtained using the Varshni equation[95],

$$E_T = E_0 - AT^2 / B + T \qquad (18)$$

where E_0 is the transition energy at 0 K, E_T is is the photon energy at temperature (*T*), and "*A*" and "*B*" are Varshni thermal constants. Table 7 shows the values chosen for these constants. Reynolds et. al.[108] have examined the polariton excitons; they concluded that the polariton exciton transitions shift to lower energies with increasing temperature at

faster rate than do other exciton transitions, since the strain and accordingly the polarizability has some temperature dependent.

Figure 58 shows the variation of the polarizability calculated using the polariton excitons –free exciton splitting formula, equation (12), with temperature (the value used for the dielectric constant is $\varepsilon = 5.15$). As shown in the figure, generally the polarizability decreased as the temperature increased. The polariton exciton therefore has two factors contributing to its energy shift with increasing temperature (1) the shift in band gap, which observed in other exciton transitions and (2) the decrease in polarizability. That explain why the polariton excitons red-shifted at faster rate than the free exctions with increasing temperature [Reynolds et. al.[108]]. Reynolds et. al. matched the energy shift with a linear and a quadratic temperature-dependent to the Varshni equation as follows:

$$E_T = E_0 - AT^2/(B-T) - (A_1T + A_2T^2)\times 10^{-3} \quad (19)$$

where the constants A and B are the same as those used for Γ_5. The other constants are taken to be A_1 = -2.16 ± 0.0357 and A_2 = 0.515 ± 0.0027 eV/K as seen in Table 7. In our work, the three-polariton excitons shifted at lower energies with increasing temperature at faster rate than the free excitons transitions as seen in Figure 57, which prove that these peaks are for polariton excitons. We noticed also that the constant "B" has the same value for both PXs and Γ_5 because of their coupling.

For further evidence that these features are for polariton excitons, we calculated their thermal activation energies. Figure 59 shows the fit of the integrated PL intensity to Equation (1) for PX_1, PX_2 and PX_3. Thermal activation energies 153 ± 7, 107 ± 4 and

11.8 ± 1 meV have obtained for PX_1, PX_2 and PX_3 respectively. The values of PX_1 and PX_2 thermal activation energies are very much higher than the binding energy of free exciton[2], which prove that these peaks cannot be free excitons. Figure 57 shows a dip at temperature 30 K in the polariton exciton curves. The depth of this dip decreased as the polariton excitons depart from the free exciton Γ_5. From Figure 58 there is a dip in the polarizability of PX_1 at 30 K, therefore we believe the observed dip in Figure 57 due to the dynamic of the strain change with temperature. The columns could twist and/or tilt relative to each other and to the average c-axis as the temperature increases in a random way. This could lead to a bend in the peak energy-temperature curve. We believe also that the random and independent behaviors of these columns is the reason for the unsystematic change in the oscillation strength (the integrated intensities) of the polariton excitons with increasing temperature as seen in Figure 59.

IV. The 2-Dimensional Electron Gas (2DEG) and The Interface Exciton (IX)

Figure 60 shows the PL spectra of the GaN/$Al_{0.2}Ga_{0.8}N$ heterostructure measured at 10 K. 6 emission lines were observed at emission energies 77, 85, 97, 104, 114, and 130 meV below free exciton Γ_5. These peaks are attributed to recombination between the electrons in the 2DEG triangular quantum well at different sub-bands and the photoexcited holes in the valance band. The transition energies for these peaks are in

[2] The binding energy of the *A* exciton is about 20 meV. A Value of binding energies of the *B* and *C* excitons is about 18 meV. [J. Appl. Phys. **87**, 3, 965 (2000)].

reasonable agreement with a previous observation [Nam et. al[119]]. The formation of the 2-dimentional electron gas (2DEG) is explained in chapter IV.

The red shift of the DX_1 exceeds that of the 2DEG sub-bands as the temperature increased. Similar observation has been reported by Fang et. al.[104] and Shen et. al.[120]. They concluded that the peaks below the DX correspond to transitions from 2DEG sub-bands to the valance band.

Figure 61 shows the carrier concentration profile versus the depth measured in the $GaN/Al_{0.2}Ga_{0.8}N$ heterostructure obtained from the capacitance-voltage measurements. As seen, the truncated curve indicates that the carriers are located primarily near the $GaN/Al_{0.2}Ga_{0.8}N$ heterointerface, inside the GaN layer.

The Capacitance-Voltage (C-V) profiling technique showed very high carrier concentration near the $GaN/Al_{0.2}Ga_{0.8}N$ interface 2.0×10^{20} cm^{-3} (sheet density, $n_s= 2.0\times10^{13}$ cm^{-2}) as seen in Figure 61. However, low electron mobility about 800 cm^2/Vs at 300 K and 3000 cm^2/Vs at 70 K was obtained as measured by Hall measurements as seen in Figure 62. The concentration of the carries near the interface as seen in Figure 61, and the drastic change in the electron mobility with temperature seen in Figure 62, indicate spatial carrier confinement, and the formation of a 2DEG near the $GaN/Al_{0.2}Ga_{0.8}N$ heterointerface [Ambacher et. al.[121] and Shen et. al.[120]].

Though the GaN/$Al_{0.2}Ga_{0.8}N$ heterostructure showed a very high carrier concentration, it showed low electron mobility. The large band gap offset between the AlGaN and GaN makes the transfer of electrons extremely efficient resulting in a 2DEG of very high density [Hsu et. al.[122]]. However, the large differences in the lattice/thermal coefficients between the GaN and sapphire and between GaN and $Al_{0.2}Ga_{0.8}N$ led to low mobility. These reasons for the electron low mobility can explained as following:

1. Strain due to lattice and thermal expansion misfit between GaN and sapphire

GaN/sapphire lattice constants mismatch (~15%) and the thermal expansion coefficients mismatch give rise to misfit strain [Viswanath et. al.[107]]. This mismatch strain generates many crystal defects and dislocations that have a profound effect on the optical and electrical properties. The highly dislocated wurtzite crystal can picture as hexagonal columns or prisms rotated relatively to each other by a small angle, with inserted atomic planes to fill the space between two columns [Weimann et. al.[123]]. On average, there is only one threading dislocation line per prism [Weimann et. al.[123]]. Several articles indicated that an edge dislocation is negatively charged [for example Hansen et. al.[124], Cherns et. al.[125], and Oila et. al.[126]]. Weimann et. al.[123] attributed the charged dislocation lines to the existence of traps along the dislocation lines. Empty traps are electrically neutral, while filled traps are negatively charged. Empty traps captured electrons while the negatively charged lines acted as scattering centers. We believe these traps contributed to the observed low mobility in the GaN/$Al_{0.2}Ga_{0.8}N$ structure. The Dislocations originate at the substrate interface[25, 127, 128] and the dislocations density

decreases substantially with increasing film thickness away from the interface [Warren et. al.[129]]. However, it is expected that the density of the dislocation is still very high even at the top of the very thins 2.0 μm GaN layer, therefore electron scattering and trapping still can take place at and near the GaN/$Al_{0.2}Ga_{0.8}N$ interface.

Furis et. al.[130] reported that threading dislocation produces defect-induced donor states. In an a study by Li et. al.[131] on different AlGaN/GaN heterostructure samples, a sample with DX at 3.476 eV showed low 2DEG electron mobility. While a very high quality sample with much lower density of donors led to significant improvements in the 2DEG electron mobility as high as 1500 cm^{-2}/Vs at room temperature and 10310 cm^{-2}/Vs at 77 K. We have observed two bound-donor excitons DX_1 and DX_2 at 3.4778 eV and 3.4674 eV respectively at 10 K for GaN/$Al_{0.2}Ga_{0.8}N$ and obtained low mobility as 800 cm^2/Vs at 300 K and 3000 cm^2/Vs at 70 K. The observation of the two donors DXs in the undoped GaN is a proof that the negatively dislocation lines produced defect-induced donor states which acted as scattering centers and contributed to the low electron mobility.

2. Effect of piezoelectric field generated by AlGaN/GaN lattice mismatch

The C-V truncated curve in Figure 61 showed unexpected peak close to the 2DEG peak. It is interesting to contrast the variation of the PL intensity of the 2DEG and the unusual peak just above it with temperature, as seen in Figure 63. As the strength of this peak increased, the 2DEG relative intensity decreased. We believe this strange feature is

the so called interface exciton IX that is observed in 2DEG GaAs/AlGaAs heterostructure [Ashkenazi et. al.[132]]. We believe this is the first observation for the interface exciton in AlGaN/GaN heterostructure to the best of our knowledge. When the temperature increased from 10 K to 50 K, the Γ_5 free exciton and the $2DEG_{(n=4)}$ peak shifted to lower energies 1.2 meV and 0.8 meV respectively since the band gap shrank as the temperature increased. The smaller shift of the $2DEG_{(n=4)}$ peak shows that the separation between the free exciton and the 2DEG decreases with increasing temperature. Similar observation has reported by Shen et. al.[120]. The IX blue shifted 2.15 meV for the same temperature change. After the 2DEG collapsed, the energy of the IX normalized so that the resulting red shift is 0.7 meV from temperature 10K to 100 K while the Γ_5 free exciton red-shifted 6.8 meV for the same temperature change.

The 2.5 % lattice mismatch between AlGaN and the GaN epilayer generated piezoelectrically induced charges. The direction of the piezoelectric field in AlGaN grown on GaN is parallel to the c-axis and opposite to the growth direction [Yu et. al.[133]]. This supported by the C-V profiling technique, as seen in Figure 61, where the concentration of electrons shown only in the GaN layer. The electric field induced by the piezoelectric polarization at $GaN/Al_{0.2}Ga_{0.8}N$ interface pushed the photoexcited holes away from the AlGaN/GaN interface very rapidly [Shen et. al.[120]]. We believe these drifted holes attracted electrons form the 2DEG to recombine radiatively and create the interface exciton IX just near the 2DEG quantum well. We believe also that this strong piezoelectric field is the reason of the formation of the 2DEG in the GaN layer not at the interface as excepted. As the temperature increased more electrons screened out of the

2DEG quantum well to recombine with the drifted photoexcited holes and enhance formation of the interface exciton IX. The creation of the interface exciton reduced the electron-hole recombination between the electrons in the 2DEG quantum well and the holes in the valance band. In addition, the formation of the 2DEG inside the GaN not the GaN/$Al_{0.2}Ga_{0.8}N$ heterointerface made the electrons in the 2DEG vulnerable to be captured by the trapping centers and to be scattered by the scattering centers located at the dislocation lines and therefore reduced the mobility.

The penetration depth of the 325 nm HeCd laser used for the PL should be comparable to the C-V depth. The power of the incident HeCd laser diminishes as 1/e with distance from the material surface as well as the carrier concentration measured by the C-V technique. Using an $Al_{0.2}Ga_{0.8}N$ absorption coefficient, 3.2 X 10^4 cm^{-1}, obtained from the literature, [Angerer et. al.[134]], we obtained a penetration depth 3125 Å. This penetration depth is sufficient to penetrate the first $Al_{0.2}Ga_{0.8}N$ 40 nm (400 Å) layer. The calculated penetration depth for of the HeCd into a GaN layer (absorption coefficient ~10^5 cm^{-1}) is about 1000 Å, in excellent agreement with Haberer et. al.[135] calculated using a GaN extinction coefficient of 0.26. Clearly, the HeCd beam penetrated the $Al_{0.2}Ga_{0.8}N$ 40 nm (400 Å) completely then penetrated the GaN layer at a depth comparable to the 600 Å depth measured by the C-V as seen in Figure 61.

Conclusion

The sample under investigation was GaN/$Al_{0.2}Ga_{0.8}N$ heterostructure. The Capacitance-Voltage (C-V) profiling technique showed very high carrier concentration at the $Al_{0.2}Ga_{0.8}N$/GaN interface, while the Hall measurements showed low mobility. It is well known that the lattice/thermal expansion mismatches strain generates many crystal defects and dislocations that have a profound effect on the optical and electrical properties. In order to investigate the presence of the strain in the structure, we performed photoluminescence (PL) measurements. Γ_5 and Γ_6 free excitons and three polariton excitons designated PX_1, PX_2, and PX_3 were observed. The observation of these excitons is great evidence of the presence of strong strain at the GaN/sapphire interface.

According to our investigation we believe the low mobility is due to the by lattice/thermal expansion mismatch between the GaN epilayer and sapphire and between GaN and $Al_{0.2}Ga_{0.8}N$ layers. These can summarize as following:

1. GaN/Sapphire mismatch

   The misfit created threading dislocation lines. The space between these lines is filled with traps. Empty traps are electrically neutral, while filled traps are negatively charged. Empty traps captured electrons and the negatively charged lines acted as scattering centers, which contributed to the low mobility.

2. GaN/ $Al_{0.2}Ga_{0.8}N$ mismatch

The large band offset between the $Al_{0.2}Ga_{0.8}N$ band gap and GaN band gap created 2DEG quantum well with very high sheet density. However, lattice parameters misfit created a strong piezoelectric field. This strong electric field pushed the 2DEG quantum well inside the GaN layer. This makes the electrons in the 2DEG vulnerable to the scattering by the localized donor's centers and traps by the trapping centers. The GaN/sapphire misfit induced-threading-dislocation lines created the trapping and scattering centers. Figure 64 illustrates the mechanisms of these processes.

In addition, we believe the piezoelectric polarization at $Al_{0.2}Ga_{0.8}N$/GaN interface pushed the photoexcited holes away from the $Al_{0.2}Ga_{0.8}N$/GaN interface very rapidly. These holes attracted electrons from the 2DEG quantum well to form what so called interface exciton IX near the 2DEG quantum well. We believe the creation of the interface exciton reduced the electron-hole recombination between the electrons in the 2DEG quantum well and the holes in the valance band and therefore contributed to the low mobility.

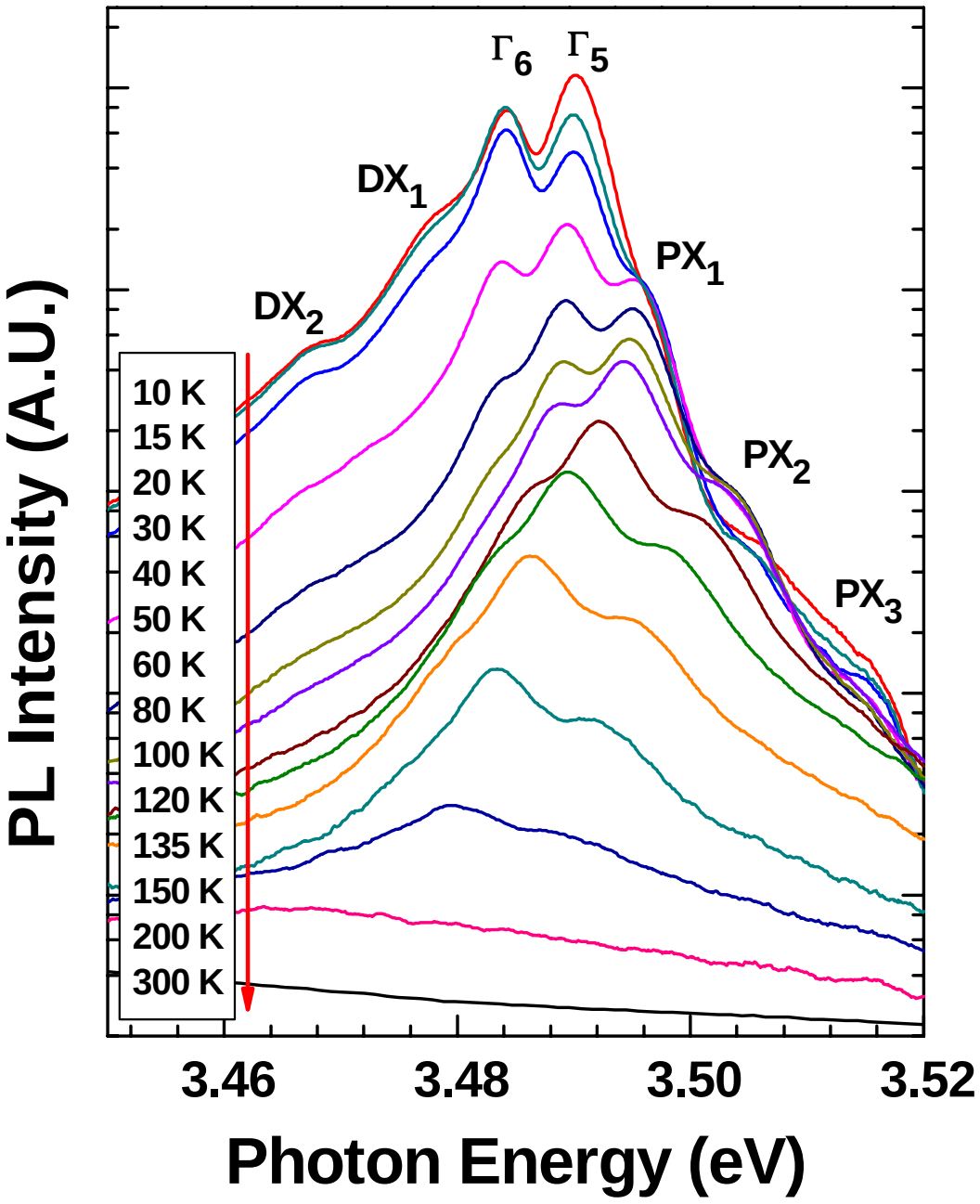

Figure 54. Temperature dependent PL of the $Al_{0.2}Ga_{0.8}N$/GaN heterostructure. The spectra clearly show two donor-bound excitons (DX_1 and DX_2), two free excitons (Γ_5 and Γ_6), and three polariton excitons PX_1, PX_2 and PX_3. The corresponding temperatures are shown on the graph. The spectra are displaced vertically for clarity.

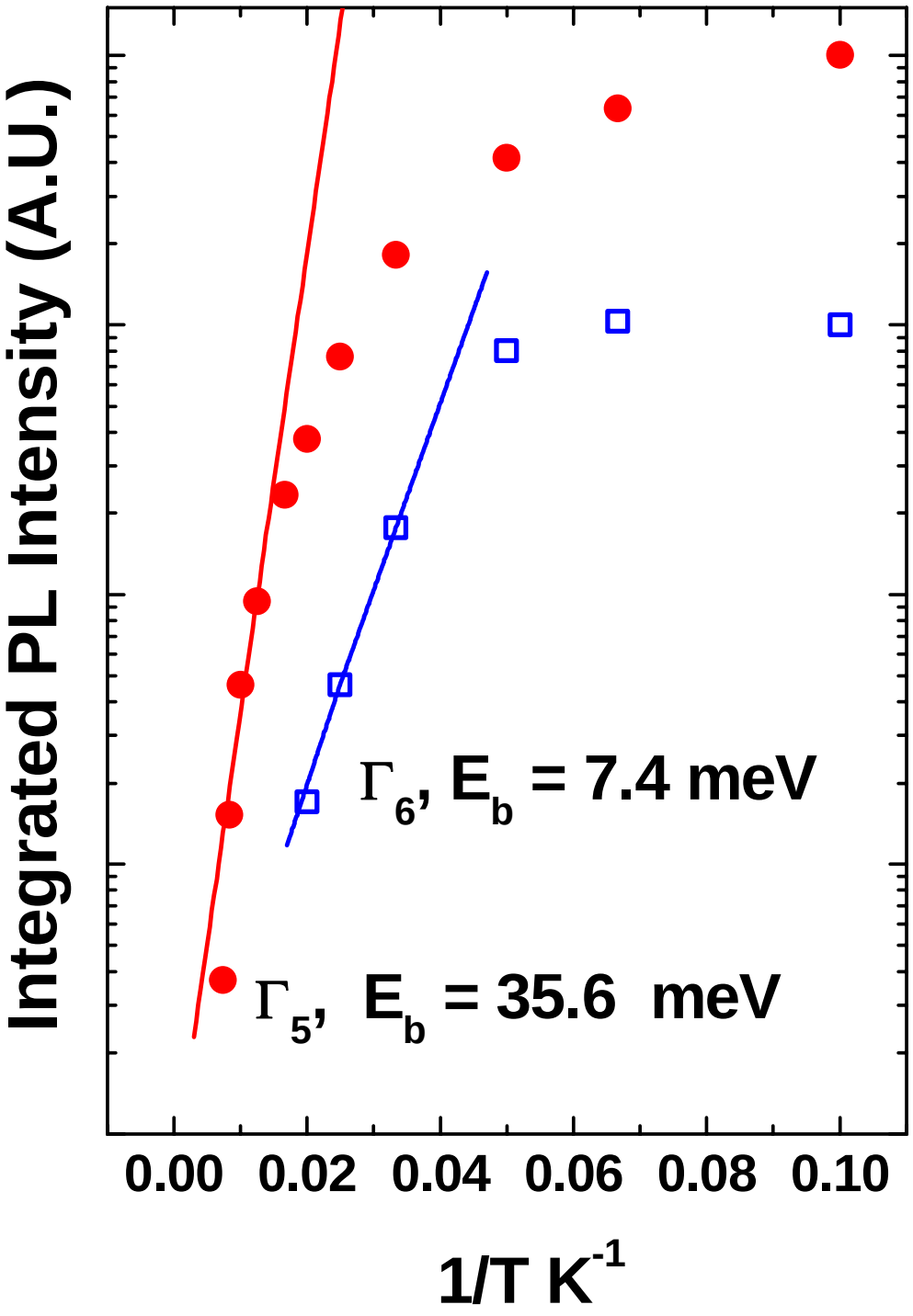

Figure 55. Temperature dependent of integrated PL intensity of Γ_5 and Γ_6, for the $Al_{0.2}Ga_{0.8}N$/GaN heterostructure grown on sapphire using HVPE technique. The solid lines are fits of these data using Eq. (10). Plots are displaced vertically for clarity.

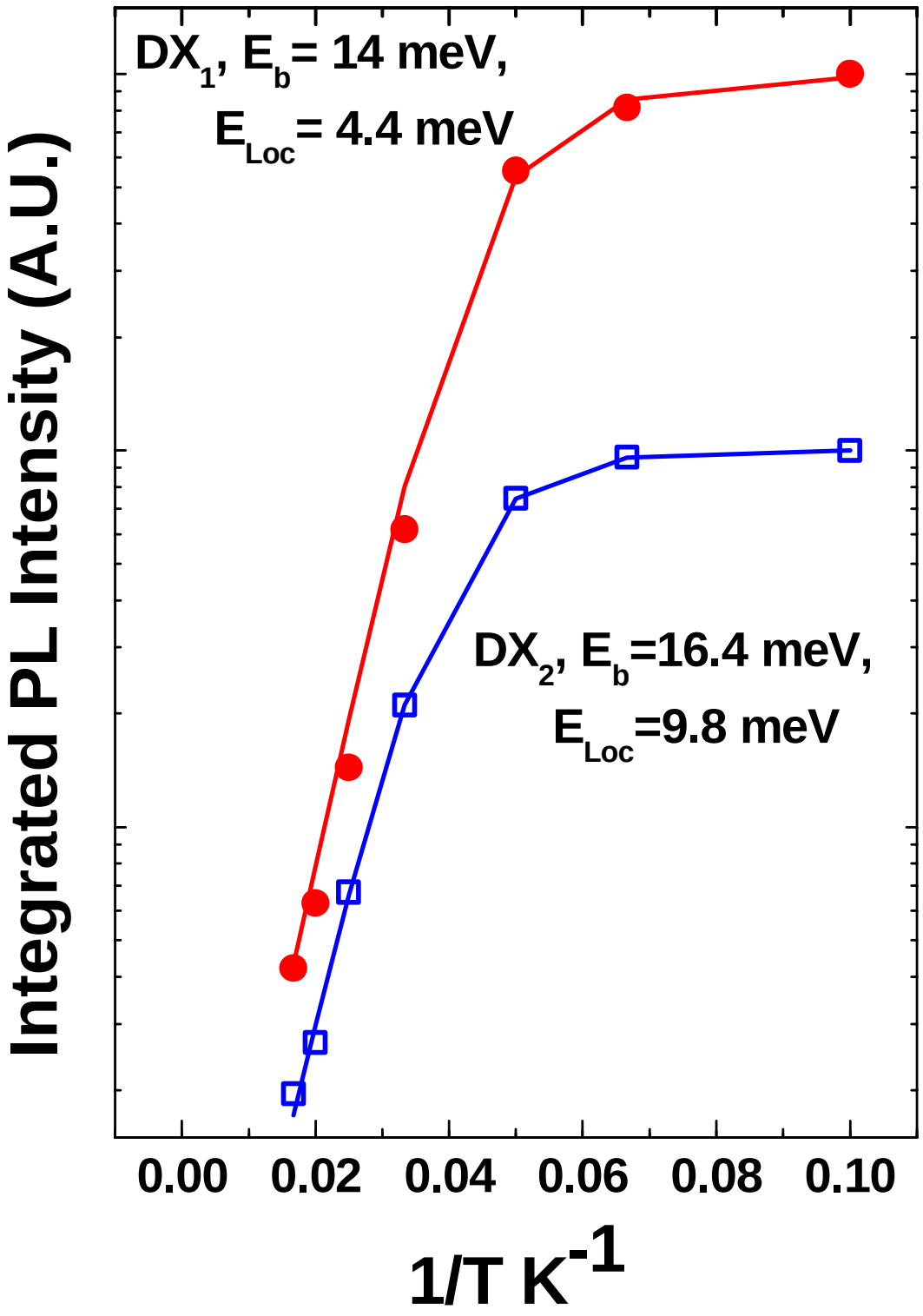

Figure 56 . Temperature dependent of integrated PL intensity of DX_1 and DX_2 for the $GaN/Al_{0.2}Ga_{0.8}N$ heterostructure. The solid lines are fits of these data using Eq. (11). Plots are displaced vertically for clarity.

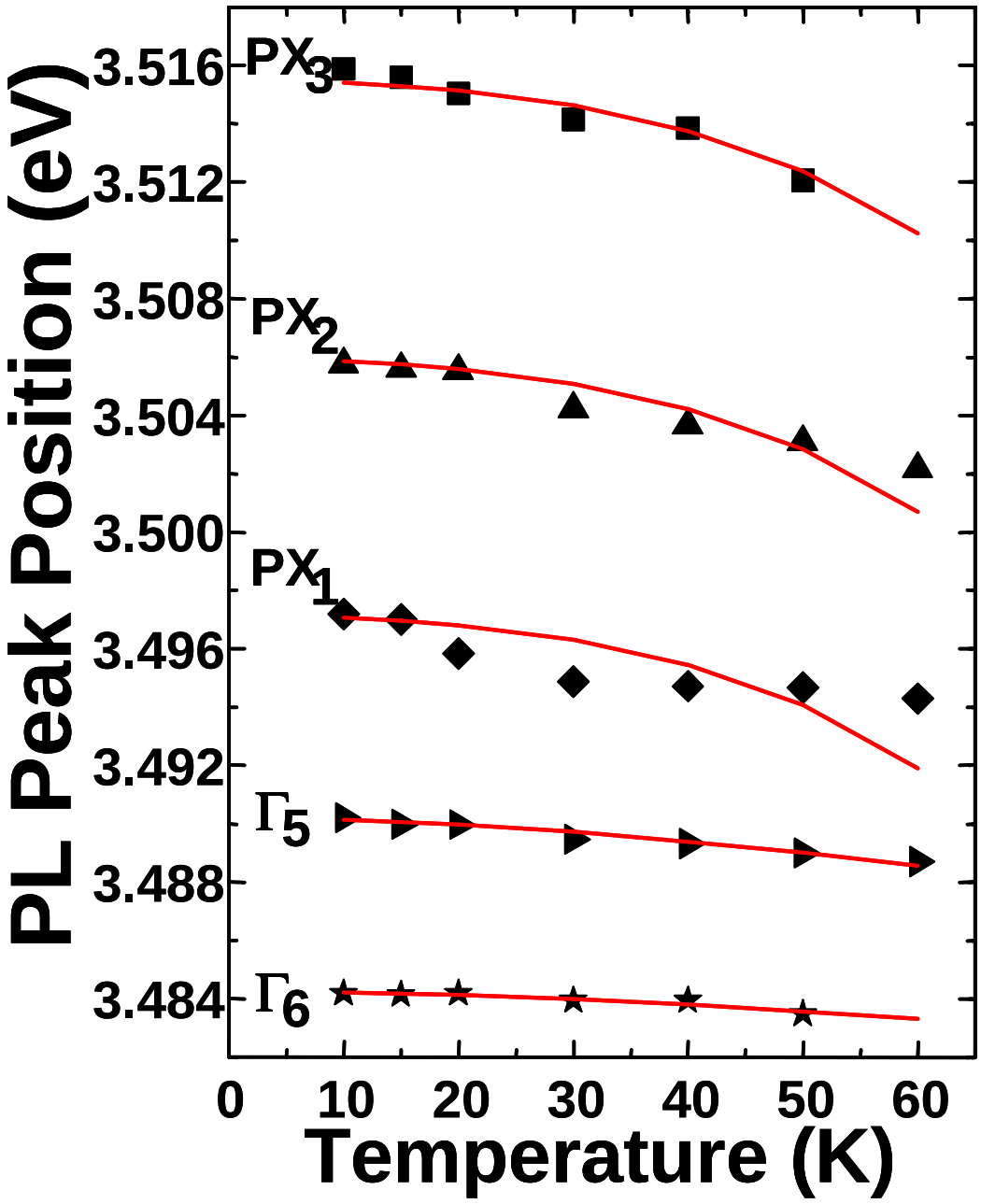

Figure 57. Temperature dependent of the PL peak position of the Γ_5 and Γ_6 free excitons and the PX_1, PX_2, and PX_3 polariton excitons seen in the PL emission of $Al_{0.2}Ga_{0.8}N$/GaN heterostructure. The solid lines are fits of these data. Γ_5 and Γ_6 are fitted using Eq. (13) while PX_1, PX_2 and PX_3 are fitted using Eq. (14).

Table 7. Varshni parameters obtained from the fitting of the peak positions of the temperature dependent of the $GaN/Al_{0.2}Ga_{0.8}N$ heterostructure to equation (13) and (14).

Peak	E_0 (eV)	A (10^{-5} eV/K)	B (K)	A_1 (eV/K)	A_2 (eV/K)
Γ_5	3.49020 ± 0.00005	8 ± 0.00001	115 ± 9	N/A	N/A
Γ_6	3.48425 ± 0.00006	8 ± 0.00001	240 ± 48	N/A	N/A
PX_1	3.49729 ± 0.00048	8 ± 0.00001	115 ± 5	-2.16 ± 0.0357	0.515 ± 0.0027
PX_2	3.50607 ± 0.00028	8 ± 0.00001	115 ± 5	-2.16 ± 0.0357	0.515 ± 0.0027
PX_3	3.51561 ± 0.00015	8 ± 0.00001	115 ± 5	-2.16 ± 0.0357	0.515 ± 0.0027

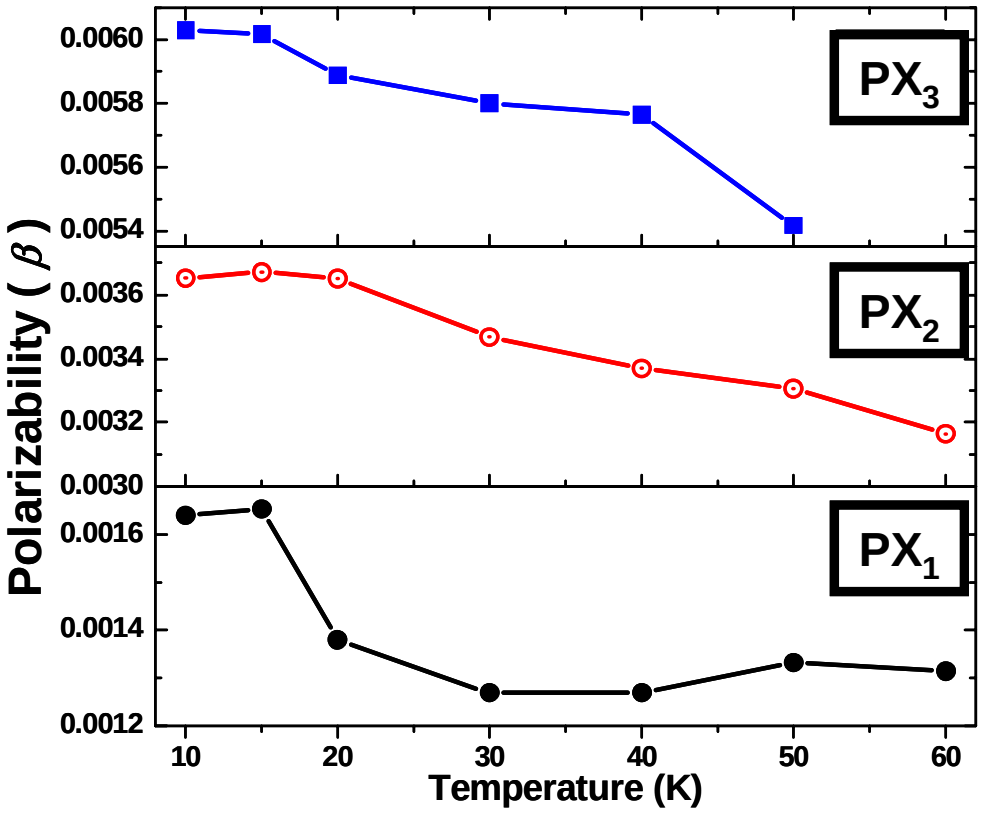

Figure 58. The variation of the polarizability corresponding to the three-polariton excitons PX_1, PX_2, and PX_3 with the temperature.

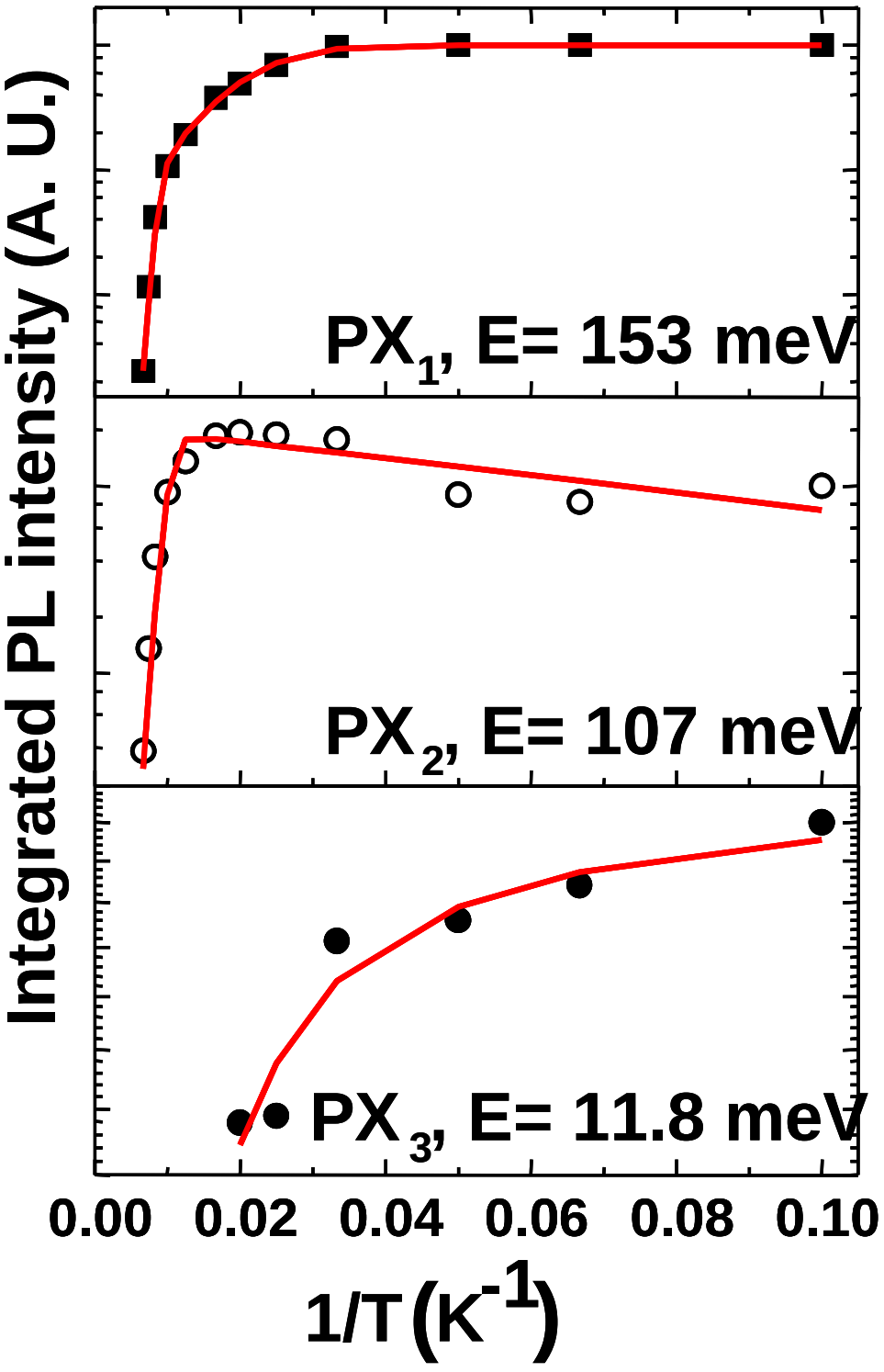

Figure 59. Temperature dependent of integrated PL intensity of the PX_1, PX_2, and PX_3 polariton excitons of an $Al_{0.2}Ga_{0.8}N/GaN$ heterostructure grown on sapphire by HVPE. Fits with Eq. (10) are shown with solid lines. The plots are displaced vertically for clarity.

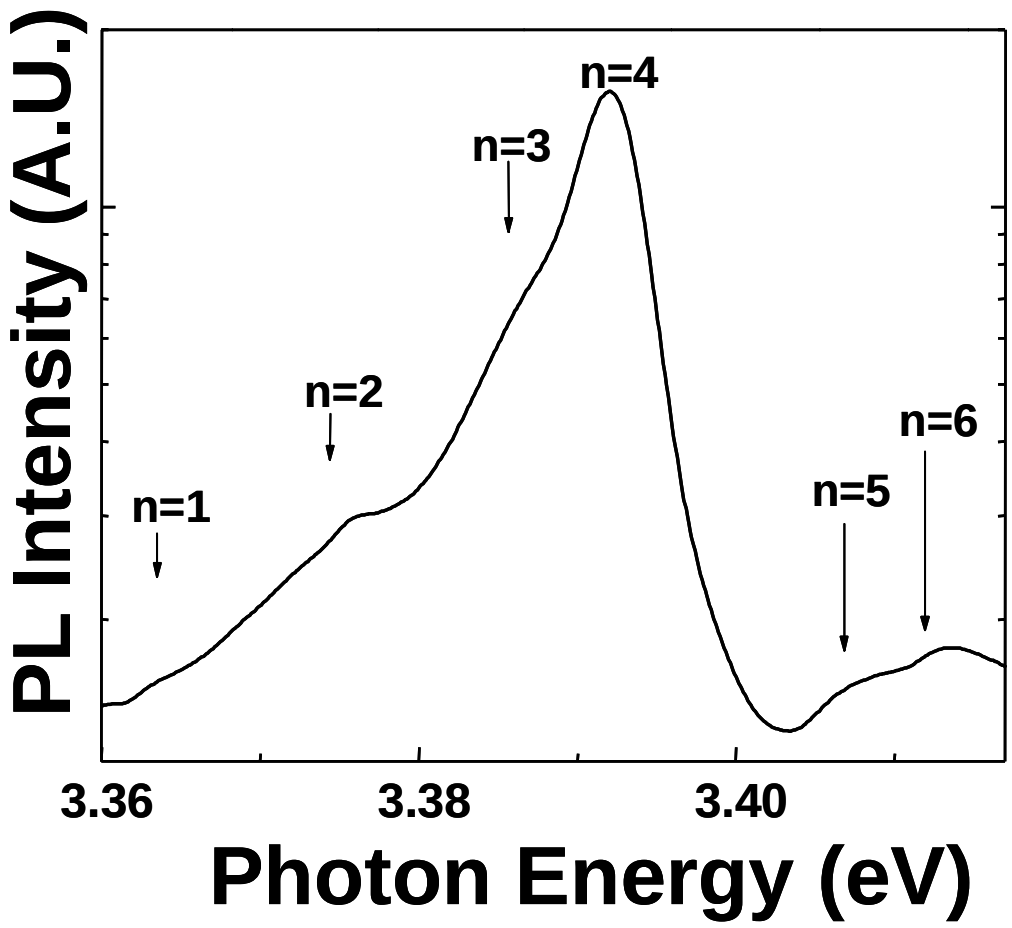

Figure 60. Transitions for 2DEG sub-bands observed in PL spectra at 10 K for a $GaN/Al_{0.2}Ga_{0.8}N$ heterostructure.

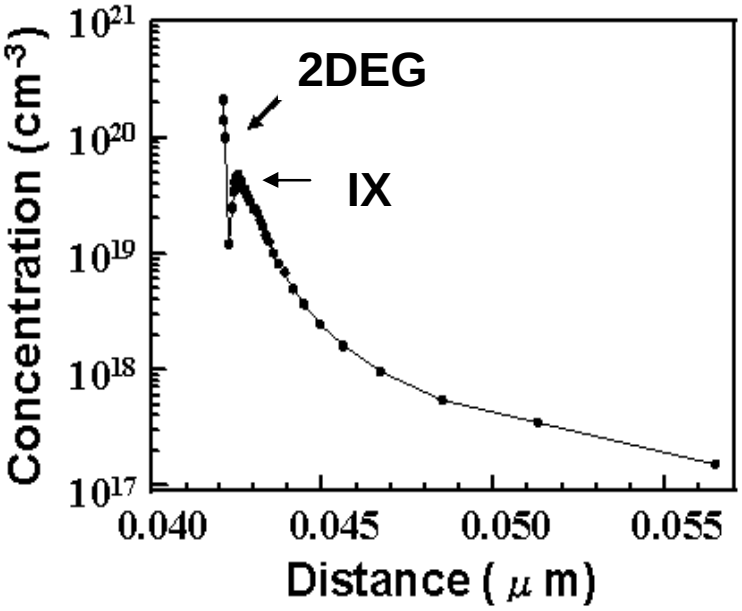

Figure 61. Electron concentration profile as a function of penetration depth of an $Al_{0.2}Ga_{0.8}N/GaN$ heterostructure measured by capacitance-voltage technique with an Hg probe at 10 kHz.

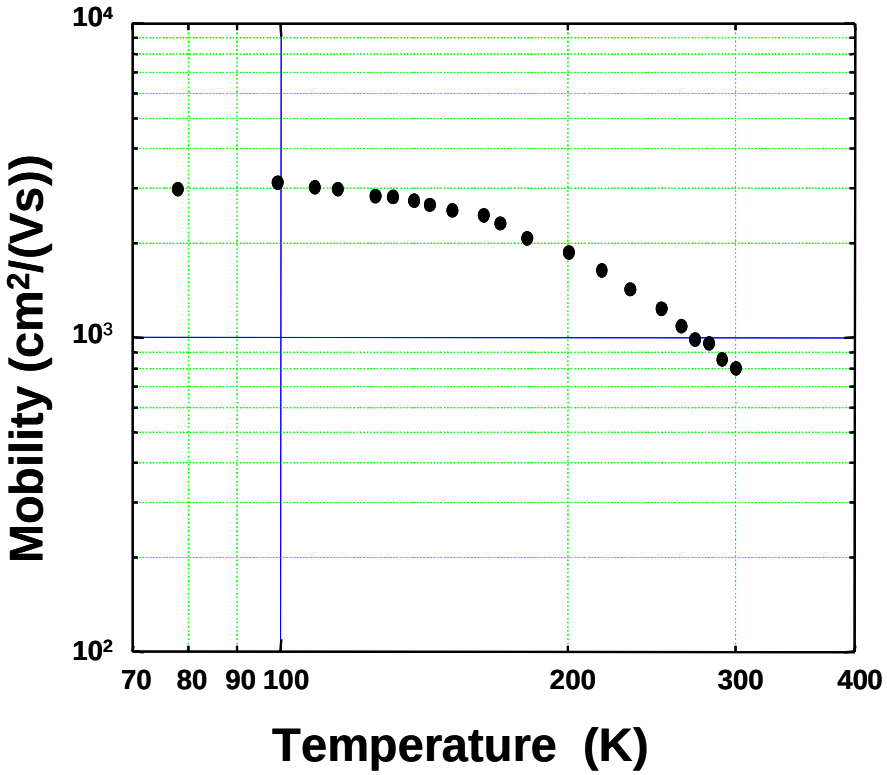

Figure 62. Temperature dependent electron mobility for the $Al_{0.2}Ga_{0.8}N/GaN$ heterostructure.

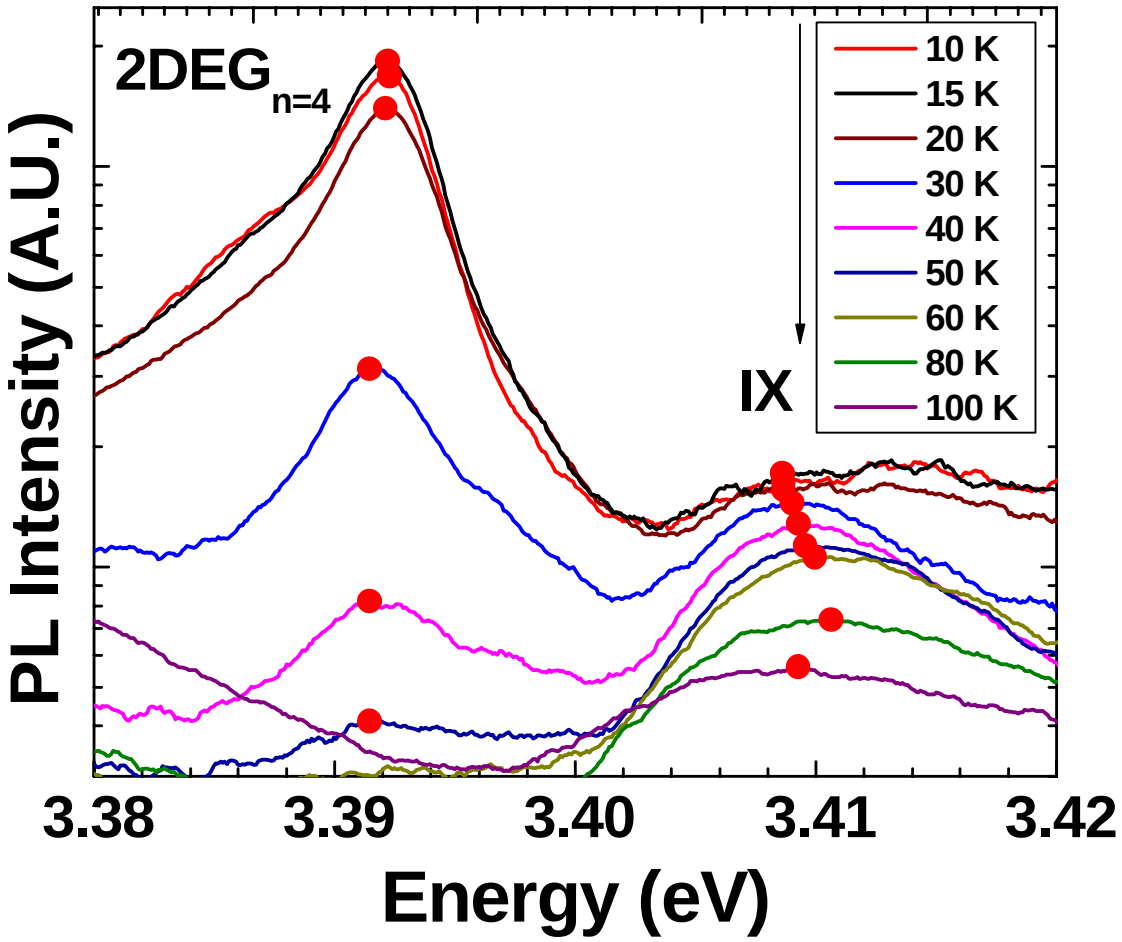

Figure 63. Variation of the $2DEG_{n=4}$ and the interface exciton IX peaks with temperature.

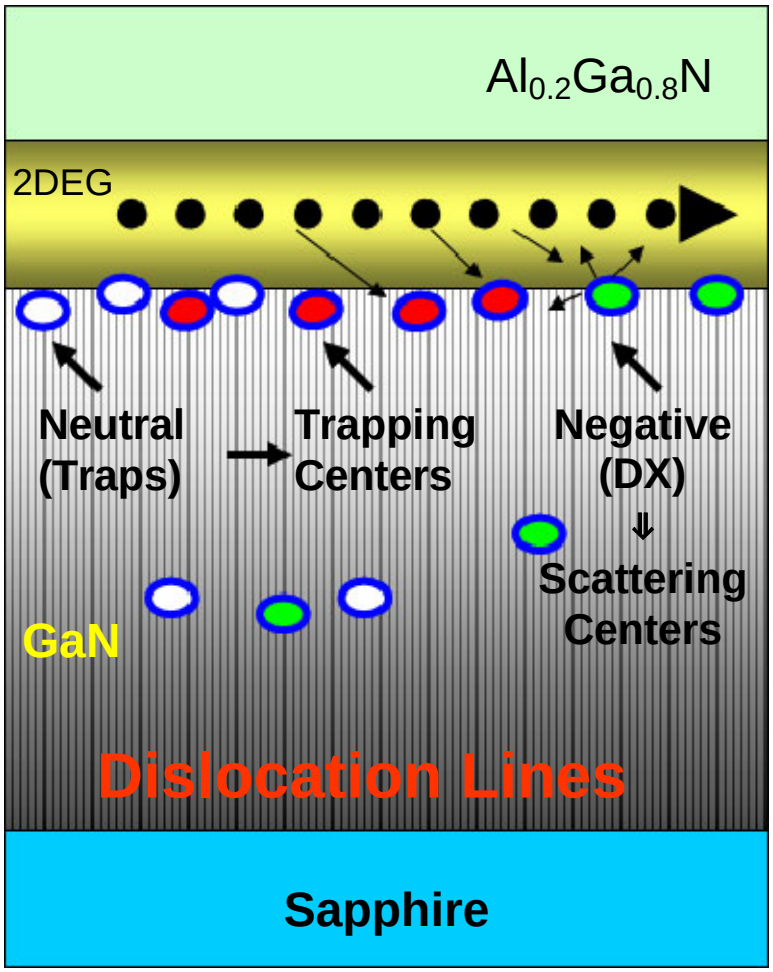

Figure 64. As illustrated in the figure the dislocation lines originate at GaN/sapphire interface and extend to $Al_{0.2}Ga_{0.8}N$/GaN interface. The space between these dislocation lines fill with traps, empty traps are neutral and filled traps are negatively charged. The negative traps form the two defect- donor-states (DX) observed in the PL spectra. The DXs act as scattering centers for the 2DEG electrons while empty neutral traps act as trapping centers for the 2DEG electrons.

CHAPTER X

Comparative Study of HVPE- and MOCVD_ Grown Nitride Structures for UV Leasing Applications[3]

INTRODUCTION

With the commercial availability of InGaN-based laser diodes (LDs) and light emitting diodes (LEDs)[136], GaN related materials have proven to be important for the development of optoelectronic devices that operate in the blue to UV spectral range. For example, optically pumped lasing at room temperature was obtained in a GaN/AlGaN structure at 362 nm, [Bidnyk et. al.[137]], which is shorter than the lowest emission wavelength of 376 nm reported for InGaN-based LDs[15]. Currently, most nitride LEDs and LDs are grown by MOCVD. However, HVPE has become an important growth technique for GaN, since it is a cost-effective way of growing thick, high quality GaN with growth rates of up to 100 μm/h [Ref. 138] and dislocation densities on the order of $10^6 cm^{-2}$ [Ref.139]. Freestanding HVPE-grown GaN films with thicknesses of up to 300 μm have been produced via laser liftoff[140]. Nichia and NEC both have fabricated InGaN-

[3] *"Comparative Study of HVPE- and MOCVD-Grown Nitride Structures for UV Lasing Applications",* J. B. Lam, G. H. Gainer, S. Bidnyk, Amal Elgawadi, G. H. Park, J. Krasinski, J. J. Song, D. V. Tsvetkov2, and V. A. Dmitriev, Mat. Res. Soc. Symp. **639**, G6.4.1, (2001).

based LDs on HVPE-grown GaN substrates[141,142]. Bulk GaN substrates grown by HVPE are available in the market. Here, we compare the optical properties of HVPE-grown samples (a GaN epilayer and a GaN/AlGaN heterostructure) with a high quality MOCVD-grown GaN epilayer.

We studied and compared the emission properties of optically excited AlGaN structures grown by two different techniques: hydride vapor phase epitaxy (HVPE) and metalorganic chemical vapor deposition (MOCVD). We successfully achieved stimulated emission (SE) in an HVPE-grown GaN epilayer and an AlGaN/GaN heterostructure at 10 K and room temperature. We found that the SE threshold and photoluminescence efficiency of the HVPE-grown samples are similar to those of high-quality MOCVD-grown structures. Photoluminescence measurements from 10 to 300 K show that the HVPE GaN has a high density of non-radiative recombination channels, especially those activated below 100 K. This study represented the first demonstration of SE in HVPE-grown AlGaN heterostructure.

EXPERIMENTAL DETAILS

The HVPE GaN epilayer and GaN/AlGaN heterostructure used in this study were grown using ammonia, GaCl, and $AlCl_3$ as the N, Ga, and Al sources, respectively. The GaN epilayer is 5 μm thick and was deposited on a 5 nm thick buffer layer on a sapphire substrate. The GaN/AlGaN heterostructure was grown on a SiC substrate and has a ~ 250 nm active GaN layer embedded between an $Al_{0.06}Ga_{0.94}N$ layer on top and an

$Al_{0.16}Ga_{0.84}N$ layer below. Both AlGaN layers are 400 nm thick. This heterostructure was designed for better optical confinement, and the top AlGaN layer has a smaller Al concentration than the lower AlGaN layer to facilitate p-doping the top layer, should we later choose to do this for making electrical contacts. The MOCVD GaN epilayer is 7.2 μm thick and was grown on a ~ 5 nm AlN buffer layer on a sapphire substrate.

Photoluminescence (PL) experiments were performed using the 244 nm line of a cw Ar+ laser. Figure 21 shows the photoluminescence measurement setup and Figure 22 shows schematic diagram of surface emission geometry.

Time-resolved PL (TRPL) measurements were made using a streak camera for detection and with sample excitation by a picosecond pulsed laser system consisting of the second harmonic of a cavity-dumped dye laser synchronously pumped by a frequency-doubled modelocked Nd:YAG laser. The overall temporal resolution of this system is better than 15 ps. Figure 24 shows the TRPL experimental setup.

The high-carrier density part (stimulated emission) of this work was performed in the traditional edge emission geometry using the second harmonic of a tunable dye laser pumped by the third harmonics of an injection-seeded Nd:YAG laser and. A closed-cycle helium cryostat was used to vary the temperature of the samples. Figure 25 shows the stimulated emission measurement setup and Figure 26 shows schematic diagram of edge emission geometry used for the stimulated emission measurements..

RESULTS AND DISCUSSION

PL spectra from the 5 μm HVPE-grown GaN at 10 K and room temperature (RT) are seen in Figure 65. At 10 K, bound exciton emission is observed at 3.474 eV (356.9 nm) with a FWHM of 4.9 meV, and the free exciton peak "A" is seen as a shoulder about 6 meV higher in energy. Room temperature (RT) PL shows free exciton position at 3.417 meV (362.8 nm) with a 32 meV FWHM. These PL peaks are red shifted by 10 meV and 14 meV from those of the MOCVD-grown GaN at 10 K and room temperature. This may be due to a decrease in the energy bandgap of the HVPE GaN epilayer caused by a reduction in the lattice mismatch induced compressive strain[143]. The reduction is likely due to a lower grown-in stress at high temperature, which may result from the growth conditions[144]. The FWHM of the free exciton peaks of both GaN epilayers are similar at RT, but the MOCVD-grown GaN has a narrower bound exciton FWHM (1.4 meV) at 10 K.

Stimulated emission (SE) was obtained for the HVPE-grown GaN at 10 K and RT using the third harmonic of an Nd:YAG laser as the excitation source. Figure 66 shows RT power dependent emission spectra of the HVPE GaN near the SE threshold. The inset shows integrated intensity as a function of excitation density. A sharp transition from spontaneous to stimulated emission occurs at the SE threshold. In addition, the SE is highly polarized, with a TE:TM ratio of 50. The RT SE threshold for this epilayer was measured to be 710 kW/cm^2, which is close to that of the MOCVD-grown GaN (600 kW/cm^2). At 10 K, the SE threshold of the HVPE GaN is 200 kW/cm^2, which is lower than the 300 kW/cm^2 of the MOCVD GaN. The RT SE peak of the HVPE GaN is at

3.310 eV, which is red shifted 107 meV from the spontaneous emission peak. This large shift is due to bandgap renormalization effects, and indicates that electron-hole plasma recombination is the dominant gain mechanism in this epilayer at room temperature, as in the case of the MOCVD GaN [Bidnyk [145]].

Figure 67 shows the HVPE-grown GaN TRPL at 10 K with a bound exciton lifetime of 67 ps, which is longer than the 35 ps lifetime of the MOCVD-grown GaN. The inset shows RT TRPL for the HVPE GaN with a decay time of 48 ps.

Figure 68 shows the PL intensity as a function of temperature from 10 to 300 K for the HVPE and MOCVD GaN epilayers. From 10 to 70 K, the PL intensity of the HVPE GaN decreases faster than that of the MOCVD GaN, as shown in in the Figure. However, above 70 K, MOCVD GaN intensity decreases more rapidly and has about the same 10 K to RT intensity ratio as the HVPE GaN. This indicates that there is still a large density of non-radiative recombination channels in the HVPE GaN, especially channels activated below 100 K. The exact mechanisms of non-radiative recombination were not studied, but in the assumption that the dislocations (and not the point defects) are the dominant non-radiative recombination centers, one would expect an improvement in the quantum efficiency by growing thicker HVPE GaN layers due to a substantial reduction in the density of dislocations farther away from the interface[146].

The HVPE-grown $Al_{0.16}Ga_{0.94}N/GaN/Al_{0.06}Ga_{0.94}N$ heterostructure PL at 10 K and RT is seen in Figure 69. The 10 K PL shows the $Al_{0.06}Ga_{0.94}N$ layer emission peak at 3.586 eV and the GaN emission peak at 3.459 eV.

We obtained 10 K and RT SE in the DH, using the second harmonic of a tunable dye laser at 350 nm (3.542 eV, which is below the band edge of the $Al_{0.06}Ga_{0.94}N$ layer) as the excitation source. This is the first demonstration of SE in a HVPE-grown nitride heterostructure. Figure 70 shows RT power dependent emission spectra of the HVPE GaN/AlGaN DH near the SE threshold. The inset shows the integrated intensity as a function of excitation density. The RT SE threshold is 1.4 MW/cm2, about twice that of the 5 μm thick HVPE GaN in Figure 66 The increased threshold is due to an increased role of non-radiative recombination due to the presence of interfaces. Slightly above the threshold, the RT SE peak is at 3.330 eV, which is red shifted about 100 meV from the PL peak. This again indicates that electron-hole recombination is responsible for the gain in the GaN active layer at room temperature. To improve the optical quality and reduce the SE threshold, a thicker layer, a separate confinement heterostructure (SCH)[137], and better interface control should be investigated.

Conclusion

We reported here a study of the optical properties of a GaN epilayer and a GaN/AlGaN double heterostructure grown by HVPE and compared these to a high quality MOCVD-

grown GaN epilayer. We obtained stimulated emission in both the HVPE-grown GaN epilayer and the GaN/AlGaN double heterostructure at 10 K and room temperature. We found that the stimulated emission threshold and photoluminescence efficiency of the HVPE-grown samples are similar to those of high-quality MOCVD-grown structures. Our results show that HVPE-grown nitrides have potential for UV – visible photonics device applications.

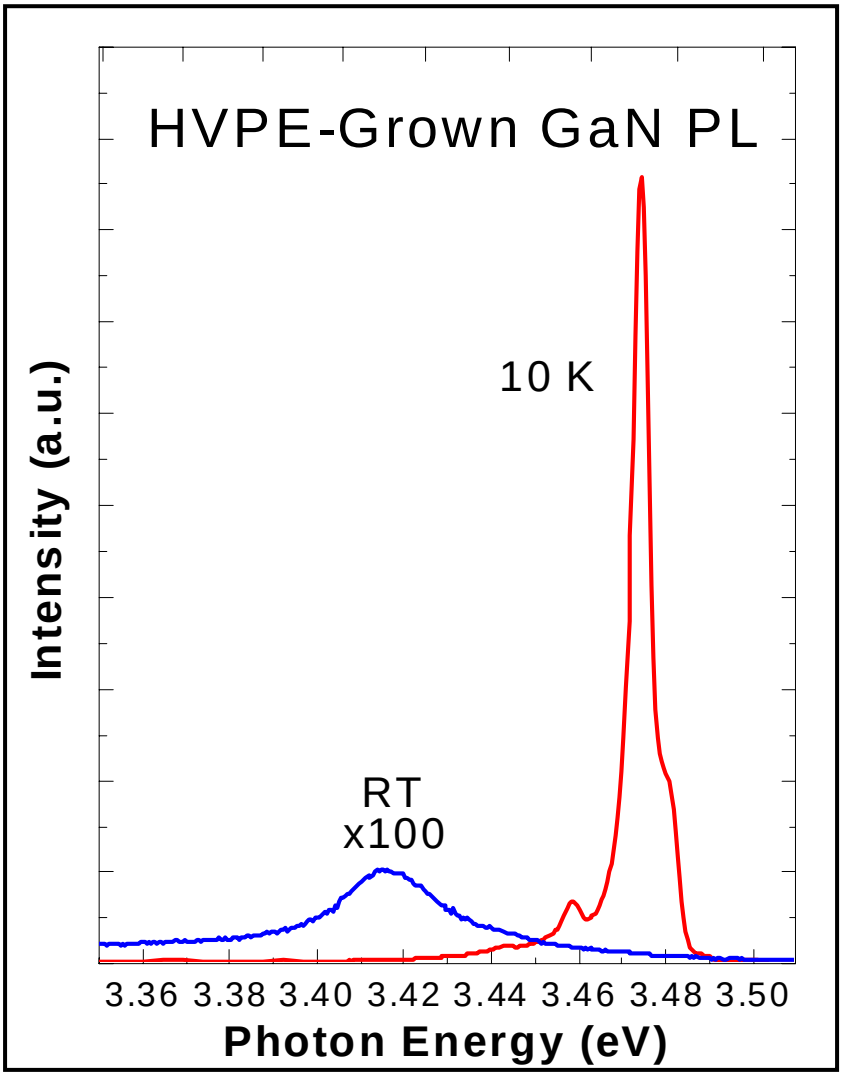

Figure 65. 10 K and room temperature photoluminescence for the 5 μm HVPE-grown GaN.

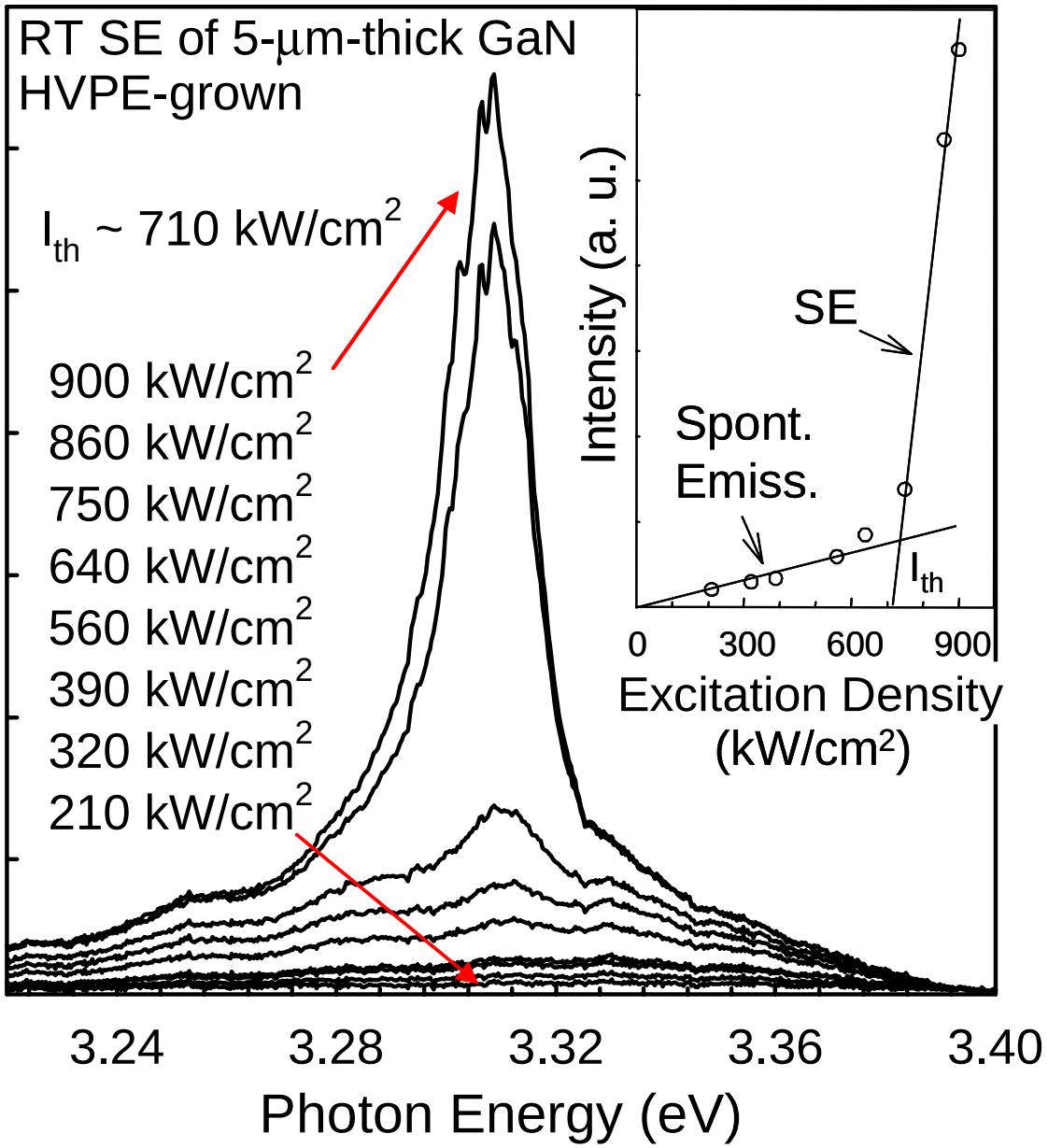

Figure 66. Room temperature emission spectra of the 5 μm thick HVPE GaN epilayer at various excitation densities near the stimulated emission (SE) threshold (I_{th}). The inset shows the integrated intensity as a function of excitation density. The lines in the inset to guide the eye only.

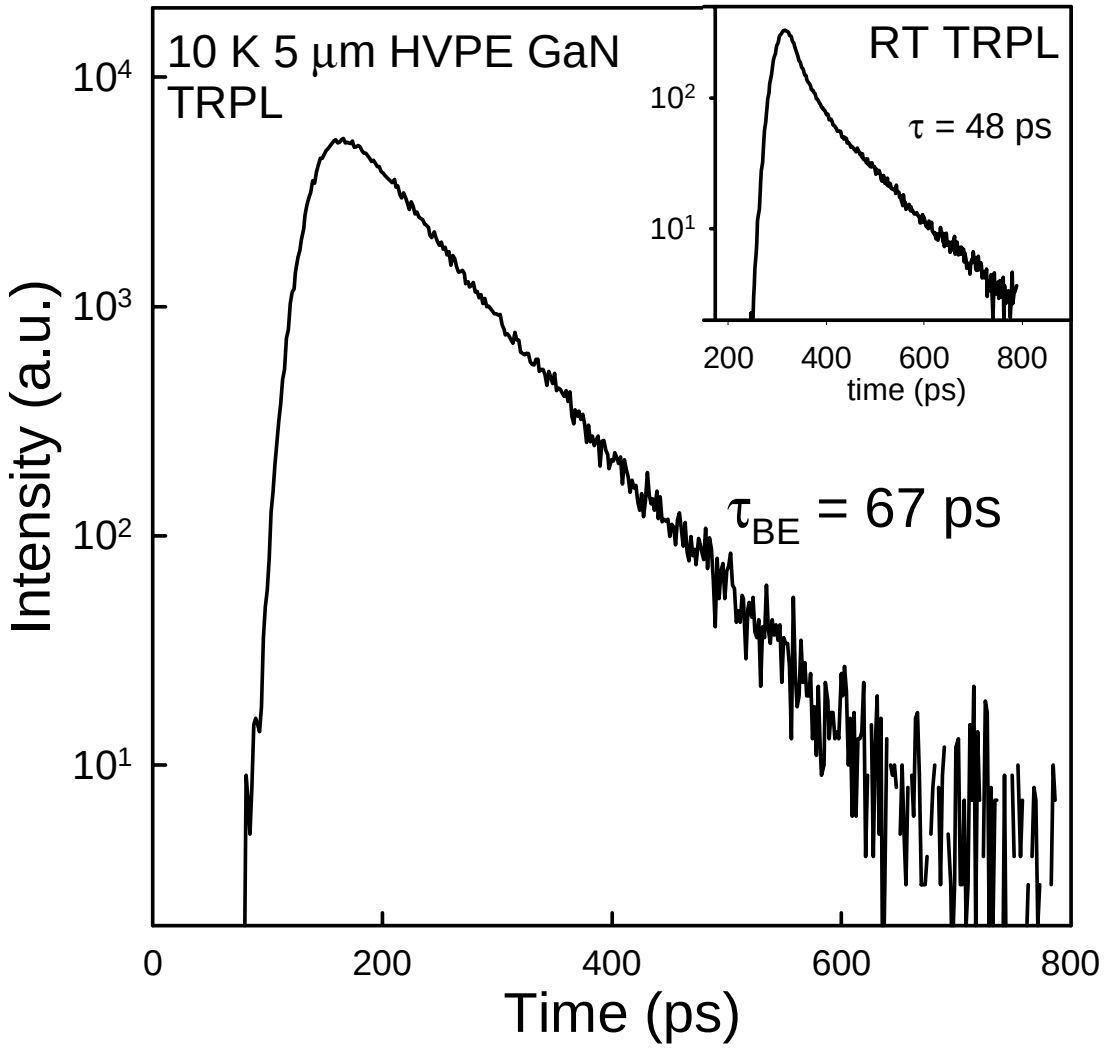

Figure 67. Time-resolved photoluminescence of the HVPE GaN epilayer at 10 K and at room temperature.

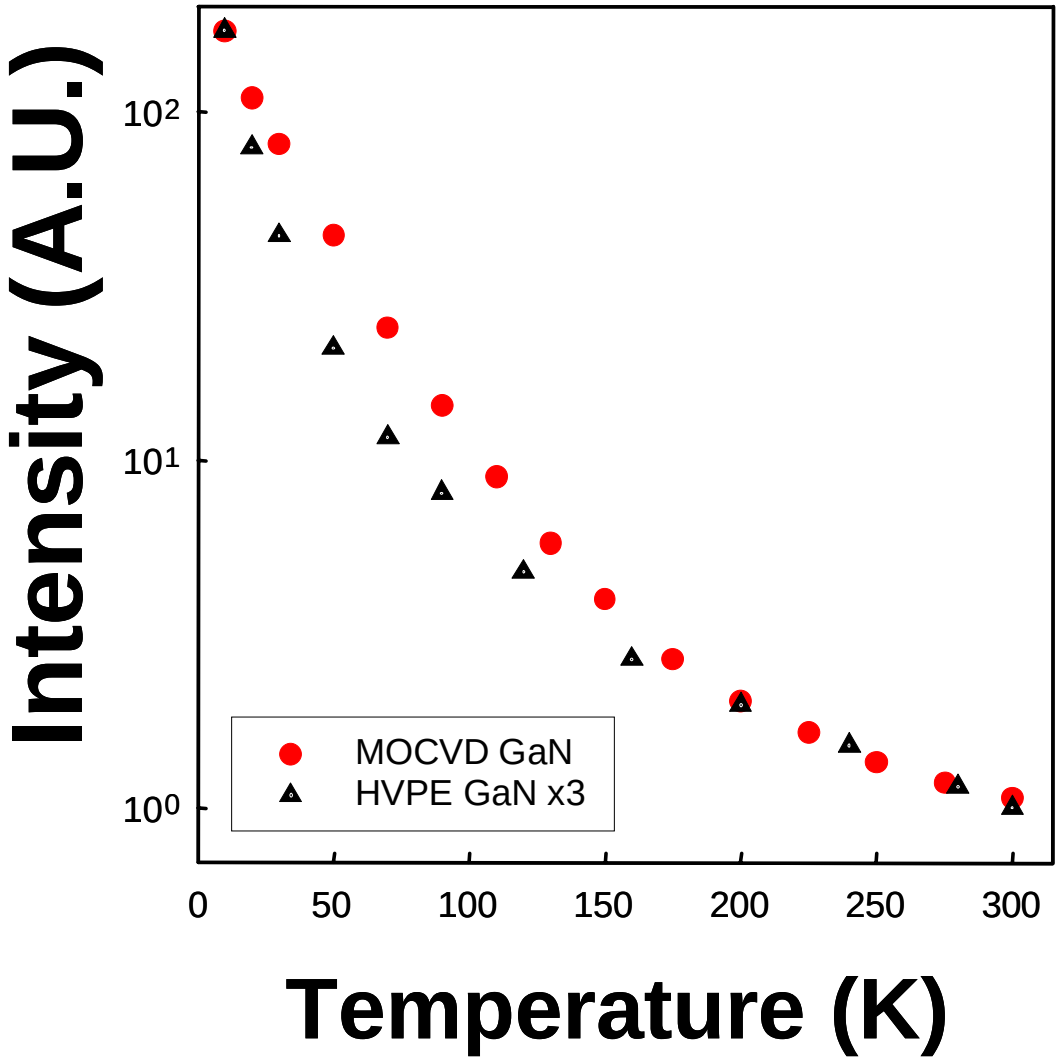

Figure 68. Temperature dependent PL intensity of the HVPE and MOCVD GaN epilayers.

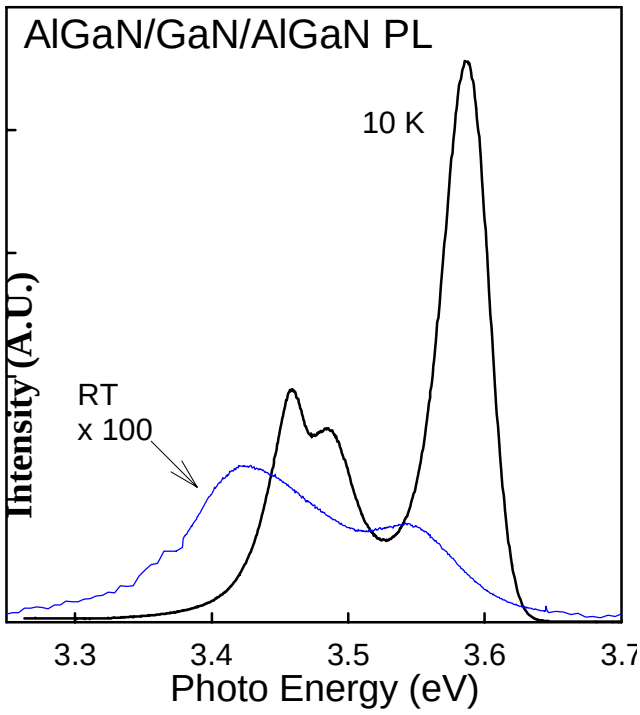

Figure 69. Photoluminescence of the HVPE $Al_{0.16}Ga_{0.94}N/GaN/Al_{0.06}Ga_{0.94}N$ heterostructure.

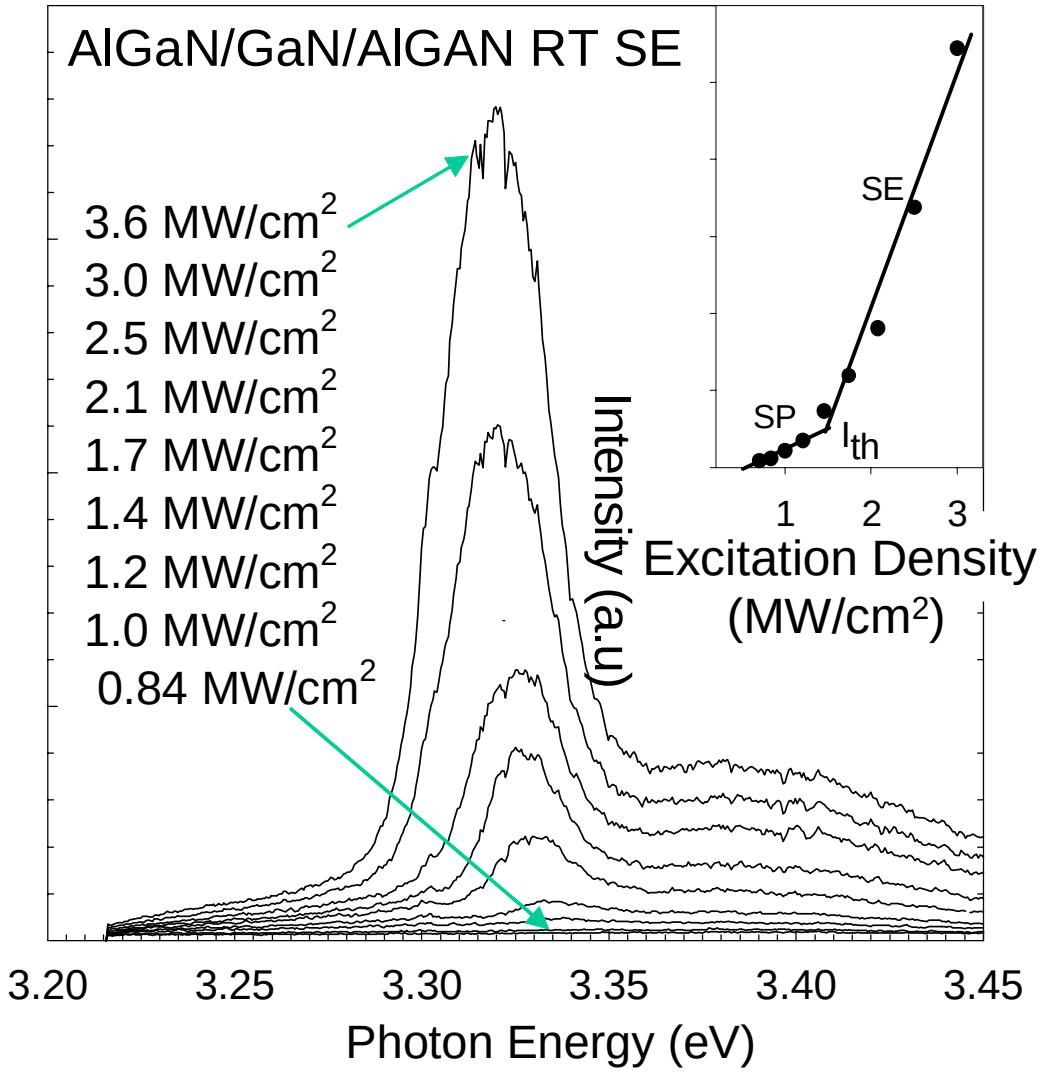

Figure 70. Emission spectra of the HVPE GaN/AlGaN double heterostructure near the stimulated emission (SE) threshold excitation density I_{th}. The inset shows the integrated intensity as a function of excitation density. The lines in the inset are to guide the eye only.

BIBLIOGRAPHY

1 . PALLAB BHATTACHARYA, “SEMICONDUCTOR OPTOELECTRONICS DEVICES”, PRENTICE HALL.

2. G. LANDWEHR, A. WAAG, F. FISCHER, H.-J. LUGAUER, AND K. SCHÜLL, PHYSICA E 3, 158 (1998).

3. H. AMANO, M. KITO, K. HIRAMATSU, I. AKASAKI. JPN. J. APPL. PHYS. PART 2-LETTERS, 28, L2112 (1989).

4. S. NAKAMURA, T. MUKAI, M. SENOH, N. IWASA, JPN. J. APPL. PHYS. PART 2-LETTERS .31, L139 (1992).

5. H. AMANO, N. SAWAKI, I. AKASAKI, AND Y. TOYODA, APPL. PHYS. LETT. 48, 353 (1986).

6. S. NAKAMURA, JPN. J. APPL. PHYS. 30, L1705 (1991).

7. A. SAKAI, H. SUNAKAWA, AND A. USUI, JPN. J. APPL. PHYS. LETT., PART 2 36, L899 (1997).

8. AKIRA SAKAI, HARUA SUNAKAWA, AND AKIRA USUI, APPL. PHYS. LETT. 71, 2259 (1997).

9. I. GRZEGORY, S. KRUKOWSKI, M. LESZCZYNSKI, P. PERLIN, T. SUSKI, S. POROWSKI, ACTA PHYS. POL. A SUPPL. 100, 57 (2001).

10. “PROPERTIES, PROCESSING AND APPLICATIONS OF GALLIUM NITRIDE AND RELATED SEMICONDUCTORS”, ED. BY J.H. EDGAR, S.T. STRITE, I. AKASAKI, H. AMANO AND C. WETZEL, INSPEC-IEE LONDON 1999.
11. S. NAKAMURA, M. SENOH, S. NAGAHAMA, N. IWASA, T. YAMADA, T. MATSUSHITA, H. KIYOKU, Y. SUGIMOTO, JPN. J. APPL. PHYS. 35, L217 (1996).
12. T. L. TANSLEY, E. M. GOLDYS, M. GOLDEWSKI, B. ZHOU, AND H. Y. ZOU, IN GAN AND RELATED MATERIALS, EDITED BY S. J. PEARTON (GORDON AND BREACH, NEW YORK, 1997), PP. 233–94.
13. B. GELMONT, K. KIM, AND M. SHUR, J. APPL. PHYS. 74, 1818 (1993).
14. M. J. MANFRA, N. G. WEIMANN, J. W. HSU, L. N. PFEIFFER, K. W. WEST, S. SYED, H. L. STORMER, W. PAN, D. V. LANG, S. N. G. CHU, G. KOWACH, A. M. SERGENT, J. CAISSIE, K. M. MOLVAR, L. J. MAHONEY, AND MOLNAR, J. APPL. PHYS., 92, 1, 338 (2002).
15. I. AKASAKI AND H. AMANO, TECH. DIG. INT. ELECTRON DEVICES MEET. 96, 231 (1996).
16. S. C. BINARI AND H. C. DIETRICH, IN GAN AND RELATED MATERIALS, EDITED BY S. J. PEARTON (GORDON AND BREACH, NEW YORK, 1997), PP. 509–534.
17. J.-Y. DUBOZ AND M. A. KHAN, IN REF. 8, PP. 343–90.
18. S. STRITE AND H. MORKOÇ, J. VAC. SCI. TECHNOL B. 10, 1237 (1992).

19. M. MIZUTA, S. FUJIEDA, Y. MATSUMOTO, AND T. KAWAMURA, JPN. J. APPL. PHYS. 25, L945 (1986).
20. S. GUHA AND N.A. BOJARZUK, APPL. PHYS. LETT. 72, 415 (1998).
21. K.S. STEVENS, M. KINNIBURGH, AND R. BERESFORD, APPL. PHYS. LETT. 66, 3518 (1995).
22. R.C. POWELL, N.-E. LEE, Y.-W. KIM, J.E. GREENE, J. APPL. PHYS. 73, 189 (1993).
23. T. SASAKI AND T. MATSUOKA, APPL. PHYS. LETT. 64, 4531 (1988).
24. T. DETCHPROHM, H. AMANO, K. HIRAMATSU, AND I. AKASAKI, J. CRYST. GROWTH 128, 384 (1993).
25. S.D. LESTER, F.A. PONCE, M.G. CRAFORD, AND D.A. STEIGERWALD, APPL. PHYS. LETT. 66, 1249 (1996).
26. I. AKASAKI, H. AMANO, Y. KOIDE, K. HIRAMATSU, AND N SAWAKI, J. CRYST. GROWTH 98, 209 (1989).
27. P. J. HANSEN,Y. E. STRAUSSER, A. N. ERICKSON, E. J. TARSA, P. KOZODOY, E. G. BRAZEL, J. P. IBBETSON, U. MISHRA,V. NARAYANAMURTI, S. P. DENBAARS, AND J. S. SPECK, APPL. PHYS. LETT., 72, 18, 2247 (1998).
28. D. CHERNS AND C. G. JIAO, PHYS. REV. LETT, 87, 20, 205504 (2001).
29. J. OILA, K. SAARINEN, A. E WICKENDEN, D. D. KOLESKE, R. L. HENRY AND M. E. TWIGG, APPL. PHYS. LETT., 82, 7, 1021 (2003).

30. NILS G. WEIMANN, LESTER F. EASTMAN, DHARANIPAL DOPPALAPUDI, HOCK M. NG, AND THEODORE D. MOUSTAKAS, J. APPL. PHYS. 83, 7, 3656, (1998).
31. S. POROWSKI, I. GRZEGORY, S. KRUKOWSKI, M. LESZCZYNSKI, P. PERLIN, AND T. SUSKI, EUROPHYSICS NEWS, 35, 3, (2004).
32. RICHARD STEVENSON, COMPOUND SEMICONDUCTOR. NET, JULY 2004.
33. J. M. BARANOWSKI, IN MRS SYMPOSIUM PROCEEDINGS VOL. 449, F. A. PONCE, T. D. MOUSTAKAS, I. AKASAKI, B. A. MONEMAR, EDITORS, MATERIALS RESEARCH SOCIETY, PITTSBURGH, P. 393 (1996).
34. S. NAKAMURA, M. SENOH, S. NAGAHAMA, N. IWASA, T. YAMADA, T. MATSUSHITA, H. KIYOKU, Y. SUGIMOTO, T. KOZAKI, H. UMEMOTO, M. SANO, K CHOCHO, APPL. PHYS. LETT. 72, 2014 (1998).
35. NILS G. WEIMANN, LESTER F. EASTMAN, DHARANIPAL DOPPALAPUDI, HOCK M. NG, AND THEODORE D. MOUSTAKAS, J. APPL. PHYS. 83, 7, 3656, (1998).
36. M. K. KELLY, O. AMBACHER, R. DIMITROV, R. HANDSCHUH, AND M. STUTZMANN, PHYS. STAT. SOL. (A) 159, R3 (1997).
37. S.T. KIM, Y.J. LEE, D.C. MOON, C.H. HONG, T.K. YOO J. CRYST. GROWTH 194 (1998) 37
38. W. S. WONG, T. SANDS, AND N.W. CHEUNG, APPL. PHYS. LETT. 72, 599 (1998).

39. M. K. KELLY, O. AMBACHER, B. DALHEIMER, G. GROOS, R. DIMITROV, H. ANGERER, AND M. STUTZMANN, APPL. PHYS. LETT. 69, 1749 (1996).
40. W. S. WONG "INTEGRATION OF GAN FILMS WITH DISSIMILAR SUBSTRATE MATERIALS BY WAFER BONDING AND LASER LIFT-OFF," PH.D THESIS, UNIVERSITY OF CALIFORNIA, BERKELEY (1999).
41. W.A. HARRISON, ELECTRONIC STRUCTURE AND PROPERTIES OF SOLIDS, FREEMAN, SAN FRANCISCO (1980).
42. R. GROH, G. GEREY, L. BARTHA, AND J.I. PANKOVE, PHYS. STAT. SOL. A 26, 353 (1974).
43. C. J. SUN, P. KUNG, A. SAXLER, H. OHSATO, E. BIGAN, AND M. RAZEGHI, J. APPL. PHYS. 76, 236 (1994).
44. M.E. LIN, B.N. SVERDLOV, AND H MORKOÇ, APPL. PHYS. LETT. 63, 3625 (1993).
45. T. J. SCHMIDT, Y. C, CHANG, AND J. J. SONG, SPIE CONF. PROCEEDING SERIES 3419, 61 (1998).
46. IRINA STATEIKINA AND KAHRIZI, DEPARTMENT OF ELECTRICAL ENGINEERING CONCORDIA UNIVERSITY, COURSE ENGR-797, OPTOELECTRONIC SEMICONDUCTOR DEVICES - PRINCIPALS AND CHARACTERISTICS. HTTP://WWW.ECE.CONCORDIA.CA/I_STATEI/VLSI-OPT/VLSI-OPT02012002.HTML.
47. L. SCHIFF, "QUANTUM MECHANICS", MCGROW HILL BOOK COMPANY, NEW YORK, 1955.

48. NASSER PEYGHAMBARIAN, STEPHAN W. KOCH AND ANDRE MYSYROWICZ , “INTRODUCTION TO SEMICONDUCTOR OPTICS”, PRENTICE HALL, PP. 137, 1993.
49. “INTRODUCTION TO SOLID STATE PHYSICS”, CHARLES KITTLE, JOHN WILEY AND SONS, INC., 7TH. EDITION
50. M. D. STRUGE, PHYS. REV. 127, 768, (1962).
51. H. IBACH AND H. LÜTH, SOLID STATE PHYSICS, SPRINGER-VERLAG.
52. T. J. SCHMIDT, THESIS, OKLAHOMA STATE UNIVERSITY, DEC. 1998.
53. D. C. REYNOLDS, D. C. LOOK , B. JOGAI, A. W. SAXLER, S. S. PARK, AND J. Y. HAHN, APPL. PHYS. LETT. 77, 18, 2879 (2000).
54. G. D. CHEN, M. SMITH, J. Y. LIN, SU-HUAI WEI, M. ASIF KHAN, C. J. SUN AND H. X. JIANG, APPL. PHYS. LETT. 68 (20), 2784 (1996).
55. YU. E. KITAEV AND P. TRONC, PHYS. REV. B, 64, 205312 (2001).
56. A. J. FISCHER, W. SHAN, J. J. SONG, Y. C. CHANG, R. HORNING AND B. GOLDENBERG, APPL. PHYS. LETT. 71, 1981, (1997).
57. J. B. LAM, S. BIDNYK, AND J. J. SONG, (UNPUBLISHED).
58. S. BIDYNK, THESIS, OKLAHOMA STATE UNIVERSITY, DEC. 1999.
59. BERNARD GIL, GROUP III NITRIDE SEMICONDUCTORS, PHYSICS AND APPLICATIONS, OXFORD SCIENCES PUBLICATIONS, 1998.
60. W. SHAN, X. C. XIE, J. J. SONG AND B. GOLDENBERG, APPL. PHYS. LETT. 67 (17) 2512, 1995.

61. R. DINGLE, D. D. SELL, S. E. STOKOWSKI, AND M. ILEGEMS, PHYS. REV. B 4,1211 (1971).
62. PIOTR PERLIN, LAILA MATTOS, NOAD A. SHAPIRO, JOACHIM KRUGER, WILLIAM S. WONG, TIM SANDS, NATHAN W. CHEUNG, AND EICKE R. WEBER., APPL. PHYS. LETT., 85, 4, 2385 (1999).
63. LANDOLT-BORSTEIN, SPRINGER, NEW YORK, VOL. 17 (1998).
64. BRIAN LITTLE, OKLAHOMA STATE UNIVERSITY, PHD THESIS, DEC. 2000.
65. A. GASSMANN, T. SUSKI, N. NEWMAN, C. KISIELOWSKI, E. JONES, E. R. WEBER, Z. LILIENTAL-WEBER, M. D. RUBIN, H. I. HELAVA, I. GRZEGORY, M. BOCKOWSKI, J. JUN, AND S. POROWSKI, J. APPL. PHYS. 80, 2195 (1996).
66. C. KIRCHNER, V. SCHWEGLER, F. EBERHARD, M. KAMP, K. J. EBELING, K. KORNITZER, T. EBNER, K. THONKE, R. SAUER, P. PRYSTAWKO, M. LESZCZYNSKI, I. GRZEGORY, AND S. POROWSKI, APPL. PHYS. LETT. 75, 1098 (1999).
67. G. B. STRINGFELLOW, "ORGANOMETALLIC VAPOR-PHASE EPITAXY: THEORY AND PRACTICE", (ACADEMIC PRESS, SAN DIEGO, 1989).
68. A. USUI, H. SUNAKAWA, A. SAKAI, AND A. A. YAMAGUCHI, JPN. J. APPL. PHYS. PART 2, 36, L899 (1997).
69. HISTORY OF HEMT TRANSISTORS, WEBSITE: HTTP://EESOF.TM.AGILENT.COM/DOCS/ICCAP2002/MDLGBOOK/7DEVICE_MODELING/3TRANSISTORS/0HISTORY/HEMTHISTORY.PDF.

70. K. V. KLITZING, G. DORDA, AND M. PEPPER, PHYSICAL REVIEW LETTERS, 45, 6, 494 (1980).

71. J.W.JOHNSON, F.REN, S.J.PEARTON, A.G.BACA, J.HAN, A.M.DABIRAN AND P.P.CHOW,WEBSITE:HTTP://MSE.UFL.EDU/~SPEAR/RECENT_PAPERS/ HIGHMOBGAN/HIGHMOBGAN.HTM

72 . HARALD IBACH AND HANS-LUTH, “SOLID STATE PHYSICS, AN INTRODUCTION TO THEORY AND EXPERIMENT”, SPRINGER-VERLAG (1993).

73. J.W.JOHNSON, F.REN, S.J.PEARTON, A.G.BACA, J.HAN, A.M.DABIRAN AND P.P.CHOW, WEBSITE: HTTP://MSE.UFL.EDU/~SPEAR/RECENT_PAPERS/HIGHMOBGAN/HIGHMOBGAN.HTM

74 . M.S. SHUR, WEBSITE: HTTP://NINA.ECSE.RPI.EDU/SHUR/NITRIDE.HTM AND B.E. FOUTZ, WEBSITE: HTTP://IIIV.TN.CORNELL.EDU/WWW/FOUTZ/ NITRIDE.HTML.

75. M.N. YODER, IEEE TRANS. ON ELECTRON DEV., 43 1633 (1996).

76. S.J. PEARTON, F. REN, A.P. ZHANG, AND K.P. LEE, MAT. SCI. AND ENG. R, 30 55 (2000).

77. M. B. PANISH, I. HAYASHI, AND S. SUMSKI, APPL. PHYS. LETT. 16, 326 (1970).

78. D. WOOD, OPTOELECTRONIC SEMICONDUCTOR DEVICES, (PRENTICE HALL, NEW YORK, 1994).

79 W. SHAN, A. J. FISCHER, S. J. HWANG, B. D. LITTLE, R. J. HAUENSTEIN, X. C. XIE, J. J. SONG, D. S. KIM, B. GOLDENBERG, R. HORNING, S. KRISHNANKUTTY, W. G. PERRY, M. D. BREMSER, AND R. F. DAVIS, J. APPL. PHYS. 83, 455 (1998).

80 Y. NARUKAWA, Y. KAWAKAMI, SZ. FUJITA, SG. FUJITA, AND S. NAKAMURA, PHYS. REV. B 55,

R1938 (1997).

81. M. I. NATHAN, A. B. FOWLER, AND G. BURNS, PHYS. REV. LETT. 11, 152 (1963).

82. R. L. M. VOOS AND J. SHAH, OPTICAL PROPERTIES OF SOLIDS, EDITED BY M. BALKANSKI, (NORTH-HOLLAND, AMSTERDAM, 1980).

83 C. KLINGSHIRN AND H. HAUG, “OPTICAL PROPERTIES OF HIGHLY EXCITED DIRECT GAP SEMICONDUCTORS,” (NORTH-HOLLAND PUBLISHING COMPANY, AMSTERDAM, 1981).

84 Y. YAMADA, Y. MASUMOTO, J. T. MULLINS, AND T. TAGUCHI, APPL. PHYS. LETT. 61, 2190 (1992).

85 K. BOHNERT, G. SCHMIEDER, AND C. KLINGSHIRN, PHYS. STAT. SOL. (B) 98, 175 (1980).

86. D. E. ASPNES, IN OPTICAL PROPERTIES OF SOLIDS, EDITED BY M. BALKANSKI, (NORTH-HOLLAND, AMSTERDAM, 1980).

87. I. AKASAKI, H. AMANO, Y. KOIDE, K. HIRAMATSU, AND N SAWAKI, J. CRYST. GROWTH 98, 209 (1989).

88. RICHARD STEVENSON, COMPOUND SEMICONDUCTOR. NET, JULY 2004.

89. T. WARREN WEEKS, JR., MICHAEL D. BREMSER, K SHAWN AILEY, ERIC CARLSON, WILLIAM G. PERRY, AND ROBERT F. DAVIS, APPL. PHYS. LETT. 67, 3, 401, (1995).

90. S.T. KIM, Y.J. LEE, D.C. MOON, C.H. HONG, T.K. YOO J. CRYST. GROWTH 194 (1998) 37

91. W. S. WONG, T. SANDS, AND N.W. CHEUNG, APPL. PHYS. LETT. 72, 599 (1998).

92. LANDOLT-BORNSTEIN, "NUMERICAL DATA AND FUNCTIONAL RELATIONSHIPS IN SCIENCE AND TECHNOLOGY", SPRINGER-VERLAG, BERLIN (1982).

93. YONG-HOON CHO, G. H. GAINER, J. B. LAM, AND J. J. SONG, PHYS. REV., 61, 11, 7203 (2000).

94. I. AKASAKI, H. AMANO, Y. KOIDE, K. HIRAMATSU, AND N SAWAKI, J. CRYST. GROWTH 98, 209 (1989).

95. Y. P. VARSHNI, PHYSICA (AMSTERDAM) 34, 149, (1967).

96. R. LAIHO, A. PAVLOV, O. HOVI AND T. TSUBI, APPL. PHYS. LETT. 63, 3, 275 (1993).

97. Z. C. HUANG, D. B. MOTT, P. K. SHU, R. ZHANG, J. C. CHEN, AND D. K. WICKENDEN, J. APPL. PHYS. 82, 5, 2707 (1997).

98. S. KUISMA, K. SAARINEN, P. HAUTOJÄRVI, AND C. CORBEL, PHYS. REV. B 55, 15, 9609 (1997).

99. K. KRAMBROCK. ANS J.-M. SPAETH, PHYS. REV. B 47, 3987 (1993).

100. W. S. WONG "INTEGRATION OF GAN FILMS WITH DISSIMILAR SUBSTRATE MATERIALS BY WAFER BONDING AND LASER LIFT-OFF," PH.D THESIS, UNIVERSITY OF CALIFORNIA, BERKELEY (1999).

101. J.A. VAN VECHTAN, PHYS. REV. B 7, 9 (1973).

102. J. KARPISNKI, J. JUN, AND S. POROWSKI, J. CRYST. GROWTH 66, 1 (1984).

103. I. GRZEGORY, S. KRUKOWSKI, J. JUN, M. BOCKOWSKI, M. WROBLEWSKI, AND S. POROWSKI, PROC. OF XX AIRAPT CONF., COLORADO SPRINGS (1993).

104. C. Y FANG, C. F. LIN, EDWARD YI CHANG AND M. S. FENG, APPL. PHYS. LETT. 80, 24, 4558 (2002).

105. D. C. REYNOLDS, B. JOGAI AND T.C. COLLINS, APPL. PHYS. LETT. 80, 21, 3928 (2002).

106. D. KOVALEV, B. AVERBOUKH, D. VOLM, H. AMANO, AND I. AKASAKI, PHYS. REV. B, 54, 4, 2518 (1996).

107. A. K. VISWANATH, J. I. LEE, S. YU, D. KIM, Y. CHOI, AND CHANG-HEE HONG, J. APPL. PHYS., 84, 7, 3848, (1998).

108. D. C. REYNOLDS, HOELSCHER, C. W. LITTON, AND T. C. COLLINS, J. APPL. PHYS., 92, 9, 5596 (2002).

109. F. A. PONCE, J. S. MAJOR, JR., W. E. PLANO, AND D. F. WELCH, APPL. PHYS. LETT. 65, 2302, (1994).

110. M. KOIKE, S. YAMASAKI, S. NAGAI, N. KOIDE, S ASAMI, H. AMANO, AND I. AKASAKI, APPL. PHYS. LETT, 68, 1403, (1996).

111. T. WARREN WEEKS, JR., MICHAEL D. BREMSER, K SHAWN AILEY, ERIC CARLSON, WILLIAM G. PERRY, AND ROBERT F. DAVIS, APPL. PHYS. LETT. 67, 3, 401, (1995).

112. D. VOLM, K. OETTINGER, T. STREIBLE, D. KOVALEV, M. BEN-CHORIN, J. DIENER, B. K. MEYER, J. MAJEWSKI, L.ECKEY, A. HOFFMANN, H. AMANO, I. AKASAKI, K. HIRAMATSU, AND T. DETCHPROHM, PHYS. REV. B, 53, 24, 16543 (1996).

113. D. C. REYNOLDS, B. JOGAI, AND T. C. COLLINS, APPL. PHYS. LETT., 80, 21, 3928 (2002).

114. MADALINA FURIS, A. N. CARTWRIGHT, HONG WU AND WILLIAM J. SCHAFF, APPL. PHYS. LETT., 83, 17, 3486 (2003).

115. D. D. SELL, S. E. STOKOWSKI, R. DINGLE, AND J. V. DILORENZO, PHYS. REV. B, 7, 10, 4568 (1973).

116. J. J. HOPFIELD AND D. G. THOMAS, J. PHYS. CHEM. SOLIDS, 12, PP. 276-248 (1960).

117. BERNARD GIL, SANDRA CLUR AND OLIVIER BRIOT, SOLID STALE COMM., 104, 5, 267 (1997).

118. R. STEPNIEWSKI, K. P. KORONA, A WYSMOLEK, J. M. BARANOWSKI, PAKULA, M. POTEMSKI, G. MARTINEZ, I. GRZEGORY AND P. POROWSKI, PHYS. REV. B, 56, 23, 15151 (1997).

119. K. B. NAM, J. LI, M. L. NAKARMI, J. Y. LIN, AND H. X. JIANG, APPL. PHYS. LETT., 81, 10, 1809 (2002).

120. B. SHEN, T. SOMEYA, O. MORIWAKI, AND Y. ARAKAWA, APPL. PHYS. LETT, 76, 6, 679 (2000).

121. O. AMBASHER, J. SMART, J. R. SHEALY, N. G. WEIMANN, K. CHU, M. MURPHY, W. J. SCHAFF, L. F. EASTMAN, R. DIMITROV, L. WITTMER, M. STUTZMANN, W. RIEGER, AND HILSENBECK, J. APPL. PHYS., 85, 6, 3222, (1999).

122. L. HSU AND W. WALUKIEWICZ, APPL. PHYS. LETT., 73, 3, 339 (1998).

123. NILS G. WEIMANN, LESTER F. EASTMAN, DHARANIPAL DOPPALAPUDI, HOCK M. NG, AND THEODORE D. MOUSTAKAS, J. APPL. PHYS. 83, 7, 3656, (1998).

124. P. J. HANSEN,Y. E. STRAUSSER, A. N. ERICKSON,E. J. TARSA,P. KOZODOY, E. G. BRAZEL, J. P. IBBETSON, U. MISHRA,V. NARAYANAMURTI, S. P. DENBAARS,AND J. S. SPECK, APPL. PHYS. LETT., 72, 18, 2247 (1998).

125. D. CHERNS AND C. G. JIAO, PHYS. REV. LETT, 87, 20, 205504 (2001).

126. J. OILA, K. SAARINEN, A. E WICKENDEN, D. D. KOLESKE, R. L. HENRY AND M. E. TWIGG, APPL. PHYS. LETT., 82, 7, 1021 (2003).

127. F. A. PONCE, J. S. MAJOR, JR., W. E. PLANO, AND D. F. WELCH, APPL. PHYS. LETT. 65, 2302, (1994).

128. M. KOIKE, S. YAMASAKI, S. NAGAI, N. KOIDE, S ASAMI, H. AMANO, AND I. AKASAKI, APPL. PHYS. LETT, 68, 1403, (1996).

129. T. WARREN WEEKS, JR., MICHAEL D. BREMSER, K SHAWN AILEY, ERIC CARLSON, WILLIAM G. PERRY, AND ROBERT F. DAVIS, APPL. PHYS. LETT. 67, 3, 401, (1995).

130. MADALINA FURIS, A. N. CARTWRIGHT, HONG WU AND WILLIAM J. SCHAFF, APPL. PHYS. LETT., 83, 17, 3486 (2003).

131. L. K. LI, B. TURK, W. I. WANG, S. SYED, D. SIMONIAN, AND H. L. STORMER, APPL. PHYS. LETT., 76, 6, 742 (2000).

132. B. M. ASHKINADZE, V. VOZNYY, E. COHEN, ARZA RON, AND V. UMANSKY, PHYS, REV. B, 65, 073311 (2002).

133. E. T. YU, G. J. SULLIVAN, P. M. ASBECK, C. D. WANG, D. QIAO, AND S. S. LAU, APPL. PHYS. LETT., 71, 19, 2794 (1997).

134. H. ANGERER, D. BRUNNER, F. FREUDENBERG, O. AMBACHER, M. STUTZMANN, R. HÖPLER, T. METZGER, E. BORN, G. DOLLINGER, A. BERGMAIER, S. KARSCH, AND H.-J. KÖRNER, APPL. PHY. LETT. 71, 11, 1504 (1997).

135. E. D. HABERER, C. H. CHEN, M. HANSEN, S. KELLER, S. P. DENBAARS, U. K. MISHRA AND E. L. HU, J. VAC. SCI. TECHNOL. B 19.3., 603 (2001).

136. NICHIA WEBSITE, “WWW.NICHIA.COM.”

137. S. BIDNYK, J. B. LAM, B. D. LITTLE, Y. H. KWON, AND J. J. SONG, APPL. PHYS. LETT. 75, 3905 (1999).

138. A. USUI, H. SUNAKAWA, A. SAKAI, AND A. A. YAMAGUCHI, JPN. J. APPL. PHYS. PART 2, 36, L899 (1997).

139. B. J. SKROMME, J. JAYAPALAN, R. P. VAUDO, AND V. M. PHANSE, APPL. PHYS. LETT. 74, 2358 (1999).

140. M. K. KELLY, R. P. VAUDO, V. M. PHANSE, L. GORGENS, O. AMBACHER AND M. STUTZMANN, JPN. J. APPL. PHYS. PART 2, 38, L217 (1999).

141. S. NAKAMURA, M. SENOH, S. I. NAGAHAMA, N. IWASA, T. YAMADA, T. MATSUSHITA, H. KIYOKU, Y. SUGIMOTO, T. KOZAKI, H. UMEMOTO, M. SANO, AND K. CHOCHO, APPL. PHYS. LETT. 73, 832 (1998).

142. M. KURAMOTO, C. SASAOKA, Y. HISANAGA, A. KIMURA, A. A. YAMAGUCHI, H. SUNAKAWA, N. KURODA, M. NIDO, A. USUI, AND M. MIZUTA, JAPN. J. APPL. PHYS. 38, L184 (1999).

143. W. SHAN, T. J. SCHMIDT, R. J. HAUENSTEIN, AND J. J. SONG, APPL. PHYS. LETT. 66, 3492 (1995).

144. S. HEARNE, E. CHASON, J. HAN, J. A. FLORO, J. FIGIEL, J. HUNTER, H. AMANO, I. S. T. TSONG, APPL. PHYS. LETT. 74, 356 (1999).

145. S. BIDNYK, T. J. SCHMIDT, B. D. LITTLE AND J. J. SONG, APPL. PHYS. LETT. 74, 1 (1999).

146. W. GOTZ, L. T. ROMANO, J. WALKER, N. M. JOHNSON, AND R. J. MOLNAR, APPL. PHYS. LETT. 72, 1214 (1998).

VITA

Amal Mostafa Elgawadi

Candidate for the Degree of

Doctor of Philosophy

Thesis: Effect of Strain on the Optical Properties of GaN Films, and GaN/AlGaN Heterostructure and Laser Lift-Off for GaN/AlGaN Multilayer

Major Field: Photonics

Education: Master of Electro-physics, Polytechnic University, Brooklyn, NY 2001.
Master of Physics, Polytechnic University, Brooklyn, NY 2001.
Master of Physics, Al-azhaer University, Cairo, Egypt 1988.
Bachelor of Science, Suez Canal University, Egypt 1984.
Completed the requirements for the Doctor of Philosophy Degree in Photonics, Oklahoma State University, Stillwater, OK July, 2005.

Professional Experience:
Research Assistant: Center for Laser and Photonics, Oklahoma State University, Stillwater, Ok, USA. 2000 and 2003.
Teaching assistant: Oklahoma State University, USA 2001.
Adjunct Professor: Polytechnic University, NY, USA. 1997-1999.
Assistant Lecturer: Suez Canal University, Egypt. 1987-1995.

Professional Memberships: American Physical Society.
Optical Society of America.